Dissertation
submitted to the
Combined Faculties for the Natural Sciences and for Mathematics
of the Ruperto-Carola University of Heidelberg, Germany
for the degree of
Doctor of Natural Sciences

presented by

Dipl.-Ing. Nicolas Altobelli
born in Nogent sur Marne, France
Oral examination: 26/05/2004

Monitoring of the Interstellar Dust Stream in the Inner Solar System Using Data of Different Spacecraft

Referees: **Prof. Dr. Eberhard Grün**

Prof. Dr. Immo Appenzeller

Zusammenfassung

Interstellarer Staub spielt eine entscheidende Rolle in vielen astronomischen Prozessen. Dennoch waren die Astronomen bis vor Kurzem auf die Beobachtung des durch interstellare Staubteilchen gestreuten Lichts angewiesen, um die Staubkomponente unserer Galaxie zu erforschen. Die in-situ Detektion von interstellarem Staub mit Detektoren auf Raumsonden ermöglichte also einen grossen Schritt für die Staubastronomie. Diese Methode bewies, dass man viel über das interstellare Medium lernen kann, indem man die in den interstellaren Staubteilchen verborgene Information entschlüsselt. Ziel der vorliegenden Arbeit ist es, Datensätze nach interstellaren Staub zu analysieren, die in den vergangenen Jahren von den interplanetaren Raumsonden *Helios*, *Galileo*, *Ulysses* und *Cassini* gewonnen wurden. Durch die Analyse dieser in-situ Daten wurden interstellare Staubteilchen zwischen 0.3 AE und 5 AE identifiziert. Zusätzlich liefern die Daten einen direkten Nachweis der Wechselwirkung des interstellaren Staubes mit der heliosphärischen Umgebung. Insbesondere konnte der Einfluss sowohl des Strahlungsdrucks als auch des Fokusierungseffekts durch Gravitation auf die Grössenverteilung der interstellaren Teilchen als Funktion der heliozentrischen Distanz gemessen werden.

Abstract

Interstellar dust plays a key role in many astrophysical processes. However, until recently, astronomers could infer some properties of interstellar dust only through observations of starlight extinction and infrared emission. Therefore, the in-situ detection of interstellar dust, based on detectors carried by spacecraft, was a major step for dust astronomy. This method showed that one can learn a lot about the interstellar medium, if one decodes the information carried by the dust grains. Goal of this work is to analyse data sets for interstellar dust, that have been collected by the interplanetary probes *Helios*, *Galileo*, *Ulysses* and *Cassini*. The analysis of the in-situ data allows us to identify interstellar dust between 0.3 AU and 5 AU. In addition, the data provide in-situ evidence for the interaction of the interstellar dust stream with the heliospheric environment. In particular, the influence of the radiation pressure and of the gravitation focusing on the interstellar dust size distribution could be measured as function of the heliocentric distance.

Contents

1 Introduction

Interstellar dust (ISD) made its entry on the modern astronomical scene as an annoyance to astronomers. As early as 1919, the astronomer Barnard published a catalogue of large field photographs of stars along the galactic circle. Starless regions clearly appeared as distinct features of the milky way and were called by Barnard 'Dark Marking'. At that time, two hypotheses were discussed: were those 'Dark Marking' due to an absence of stars or the result of some light absorbing mass? Observation data collected by famous astronomers like Wolf, Russel or Hubble led to the suggestion of absorbing matter, in a finely divided state, present in large gas clouds distributed all around the milky way disk. This new idea was supported by new theoretical works on extinction of star light by absorption and scattering along the light path. A more or less precise quantification of the star light extinction was crucial for works like those of Kapteyn, started around 1900, aiming at deriving the shape and the size of our milky way from stars distribution and brightness. An insufficient understanding of interstellar absorption biased the analysis of Kapteyn, and other methods had to be used later by Shapley to get a more precise view of our Milky Way. Despite of intensive observations, few progress had been made in the 1940s, as resumed by Sears (1940). ISD was described as 'an immense complication of every problem involving the apparent brightness of stars; and that reaches farther than one might suspect.'

From an 'immense complication', ISD became an object of astrophysics in itself in the next decades, involved in key questions of the galactic evolution. Hiltner (1949) and Hall (1949) showed that the light from space-reddened stars was partially plane-polarized because of the presence of ISD grains in the line of sight. The plane of polarization shows a preference for the plane of the Milky Way. The fundamental existence of a galactic magnetic field could be inferred from this observational fact, responsible for an anisotropy in the orientation of elongated ferromagnetic dust. More recently, ISD also arose cosmological questions. As recent measurements of high redshift quasars proved, dust was present in the early ages of the universe, implying a much higher star formation rate than suspected (Andreani et al., 1999).

More generally, ISD grains are strongly involved in the cycle of matter in the galaxy and in the interstellar chemistry, providing surfaces for complex organic molecule formation in the interstellar medium, and protecting already formed molecules from photodissociation (Greenberg et al., 2000). As about 40% of the heavy elements (heavier than helium) of the galaxy are embedded in ISD grains, they are the main conveyor of matter in the galaxy. The life cycle of ISD is closely associated with that of stars. Indeed, via their IR emission, ISD grains help removing the gravitational energy of a

collapsing cloud. Through their strong absorption in UV, they also shield the molecular regions from nearby stellar radiation and thus speed up the formation of a proto-stellar core by reducing the cloud ionization level (Ciolek, 1995). Solid grains condense in the cool upper atmospheres of stars that evolved off the main sequence, or in planetary nebulae, novae or supernova remnants. Through these processes, the dust grains are injected into the diffuse interstellar medium (ISM), where they can interact with their environment, the diffuse interstellar medium or dense molecular clouds. As the direct formation of dust by nucleation growth in those clouds is improbable (Evans, 1994), the ISD grains are more than matter conveyors: as witness of their past formation in evolved stars regions, they carry crucial information about the physical conditions that once ruled their formation.

Like photons, ISD grains should therefore be considered as information quanta. Similar to astronomical observations, the in-situ detection of ISD grains is a way to decode the information carried by those cosmic messengers. Only a decade ago, the dust experiment on board the solar probe *Ulysses* proved that a dust stream made of submicrometer size ISD grains penetrates the heliosphere and reaches regions of the solar system accessible to spacecraft (Grün et al., 1993). Besides, the *Ulysses* interstellar neutral gas experiment allowed accurate measurements of the flow of neutral interstellar helium entering the heliosphere (Witte et al., 1993). Note that although Hydrogen is the most abundant gas specie, it does not reach the inner solar system since it is depleted by photoionisation and charge exchange. Furthermore, filtration processes at the heliopause are more efficient for Hydrogen than Helium, that passes through the whole interface almost unaffected, (Bleszynski, 1987).

These results confirmed that the solar system could no be longer considered as a hermetically closed system inside the interstellar medium. Interstellar matter, both gas and dust, may have enriched the solar system since its formation. On its way around the galactic center during 4.5 billions of years, the Sun has traversed many dusty molecular clouds. The influence of each interstellar cloud crossing onto the solar system evolution depends on the density, the temperature and the dust-to-gas mass ratio of the cloud. Speculative theories still try to evaluate the impact on the terrestrial planets of the interstellar physical conditions that have surrounded the solar system in the past (Yeghikyan and Fahr, 2003). On long time scales, the accretion of cosmic dust may have changed the chemical composition of planetary surfaces or atmospheres (Fahr, 1991).

Currently, the Sun is flying through one of the warm clouds embedded in the hot medium of the local bubble (Holzer, 1989). In the following, I will refer to this substructure of the local bubble as the Local Interstellar Cloud (LIC). The LIC is a few parsecs broad dusty plasma whose electron density is about 0.1 cm^{-3} while its temperature lies around 10000 K. Recent measurements confirmed the relative velocity between the Sun and the LIC to be about 26 kms^{-1} (Witte et al., 1993). The Sun motion with respect to the LIC is illustrated in Fig. 1.1. Thus, it is an important question whether some ISD grains are able to traverse the Solar system. Although this was demonstrated theoreti-

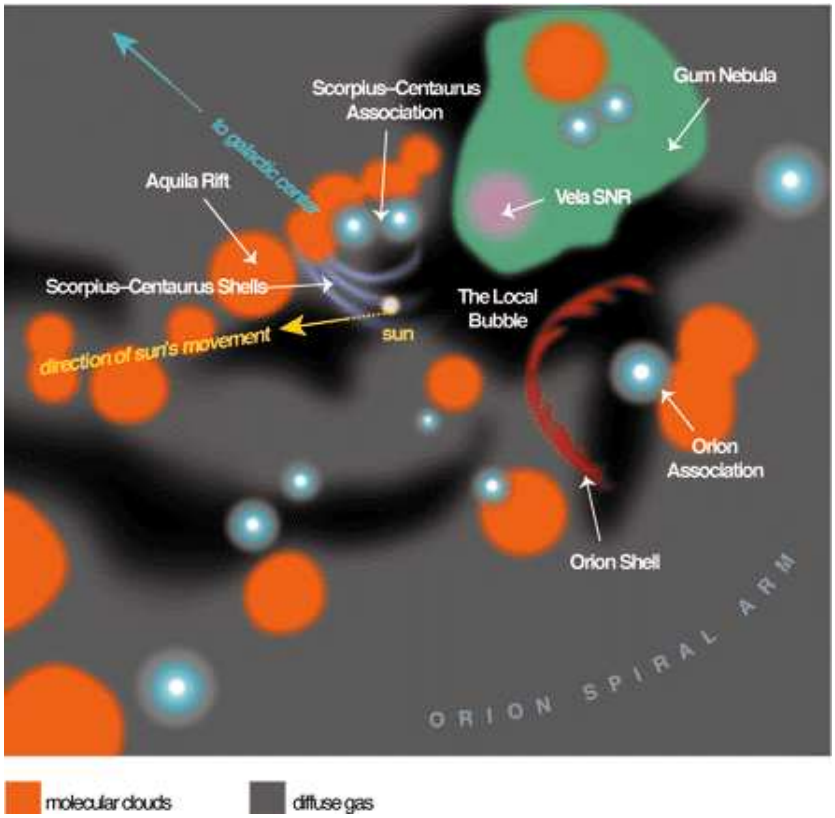

Figure 1.1: Morphology of the local galactic environment of the Sun, projected onto the galactic plane (Frisch, 1998). The radius of the figure is 500 pc. The arrows in the center show the motion of the Sun and of the local finger of warm partially ionised material of the LIC, respectively. Nearby molecular clouds are indicated by filled circles. The diffuse interstellar medium which reddens starlight is shown in light grey.

cally in the mid-70th, (Levy and Jokipii, 1976; Gustafson and Misconi, 1979; Morfill and Grün, 1979), it was not before 1993 when the first unambiguous in-situ detection of ISD grains succeeded by the *Ulysses* dust instrument (Grün et al., 1993). The age of the in-situ exploration of interstellar matter in our Solar System had begun...

Only the *Ulysses* spacecraft, orbiting the Sun on a high inclined orbit is able to continuously monitor the evolution of the ISD stream. Since 1993, *Ulysses* has accumulated about 10 years of interstellar data. From the data analysis one knows that the heliosphere filters the ISD stream, by the action of the radiation pressure and the interaction of the charged dust grains with the solar electromagnetic field (Landgraf, 1998; Landgraf et al., 1999; Landgraf et al., 2003). This analysis revealed the role played by the heliosphere as a huge mass spectrometer for ISD grains. Furthermore, the monitoring of the ISD stream gives an insight in the physics of the LIC, as summarized in the next paragraph.

The directionality of the ISD stream coincides with the downstream direction of the interstellar Helium (Baguhl et al., 1995; Witte et al., 1993; Landgraf, 1998). The heliocentric injection velocity v_∞ of ISD is about 26 kms^{-1} comparable with the Sun's speed relative to the LIC (Grün et al., 1994). Those measurements show that the ISD stream results from the relative motion of the solar system to the surrounding LIC. Furthermore, within the resolution of the *Ulysses* dust instrument, the ISD flux appears to be well collimated. This fact indicates that the ISD grains are dynamically coupled with the interstellar Helium. In addition, ISD grains detected by *Ulysses* were dominantly found to have masses of about $3{\cdot}10^{-16}$kg (Landgraf et al., 2000) corresponding to grain radii of about 0.4 μm. The size distribution of ISD grains is the result of grain formation and destruction processes (Mathis et al., 1977; Jones et al., 1996). A fit of the interstellar extinction curve leads to the so-called MRN distribution (Mathis et al., 1977). However, the *Ulysses* data show an excess of large grains with a mass value greater than the MRN cut-off mass. It was suggested by Grün (2000) that the collisional evolution of large grains provides a source for smaller grains. In contrast, the *Ulysses* data point out a lack of small grains as observed outside the heliosphere (Landgraf et al., 2000). A possible filtering of those small grains at the heliospheric interface was proposed (Linde and Gombosi, 2000). At least, it was shown in Czechowski (2003) and Landgraf (2003) that small grains are coupled with the interplanetary magnetic field (IMF) and may be prevent by Lorentz forces to reach the inner Solar System.

However, all the initial interstellar data provided by *Ulysses* were obtained between 2 AU and 5 AU (outside 3 AU near the ecliptic plane and outside $\approx$ 2 AU at high ecliptic latitudes, (Grün et al., 1997)). Therefore, what happens to the ISD grains at closer heliocentric distance than 3 AU is still unclear. In particular, are the grains detected by the *Ulysses* spacecraft still detectable at Earth orbit distance or even closer to the Sun? How does the flux density evolve under the action of the heliospheric filtering processes? Can one validate the picture of the heliosphere as a mass spectrometer? What can we learn about the past dynamics in the LIC of the ISD grains reaching close heliocentric distances? What is the quantitative contribution of the ISD to the meteoritic environment of the Earth? Is it possible to infer some material properties of the ISD grains? What can one learn about the LIC with measurements performed at Earth orbit distance?

Answers to these questions are the main goal of this work. But, since the first in-situ detection of the ISD stream by the *Ulysses* spacecraft, no mission has been devoted explicitly to the study of the ISD flux. However, on their way to their main scientific targets, space probes carrying dust instruments sometimes benefit from a genuine location and of a favorable pointing of their instruments to detect ISD grains. Things become very interesting if those measurement opportunities are provided at locations where ISD has not been detected before... Such opportunities were provided by the *Cassini*, *Galileo*, and *Helios* missions which offered two important advantages. First, each of those missions is equipped with dust detectors allowing an equivalent detection sensitivity in the sub-micrometer size range and comparable data. Second, from

the *Helios* mission to the *Cassini* mission, the data cover a time period between 1974 and 2000 and a heliocentric distance ranging from 0.3 to 2.5 AU. As a consequence, I present in this thesis the first monitoring on long time scale of the ISD stream at closer heliocentric distances than ever before.

This work is organized as follows. In the next chapter, the dust instruments carried on each spacecraft are presented together with a brief overview of the physics associated to the impact ionisation dust detection technique. In Chapter 3, a description of the interplanetary and ISD populations is given. In particular, the models for the IDPs and ISD on which I will base my analysis are discussed. In addition, the relevant dynamical aspects are identified, including a description of the forces involved in the dust grains evolution. In Chapter 4, after a general description of the method developed in this work to discriminate ISD grains from IDPs, the dust data of the *Cassini*, *Galileo*, and *Helios* mission are analysed, and the ISD contribution to each data set is estimated. To conclude this chapter, a partial reanalysis of the *Ulysses* ISD data is performed, pointing out an instrumental effect and its influence onto the data interpretation. The results of the data analysis are summarized in Chapter 5. An important part of this chapter is devoted to a discussion about the implications of the ISD detection at close heliocentric distance.

2 In-situ detection: principles and instruments

During the last three decades, several dust detectors were developed and calibrated at the Heidelberg dust accelerator facility and flown on the interplanetary probes *Helios*, *Galileo*, *Ulysses* and *Cassini*. All the in-situ data analysed in this thesis have been obtained by the impact ionisation detector sub-systems (IID) of those instruments. The present chapter aims at familiarizing the reader with the technical and physical mechanisms required for the understanding of the data analysis. I first briefly describe the physics of impact ionisation, before I present the instrumental setups. I finally conclude this chapter by discussing the measurement reliability of the IID subsystems, in case of high energetic impacts.

2.1 Impact ionisation

Impact ionisation is the fundamental physical mechanism involved in the cosmic dust detection as discussed in this work. In the early 60's, the residual ionisation of a gas cloud generated upon impact of a high-velocity projectile onto a solid target was discussed theoretically by Raizer (1960). The first experimental verification of the theory succeeded as soon as facilities were built to accelerate micrometer-size particles in vacuum to high speeds (typically, many kms^{-1}) (Friichtenicht and Slattery, 1963). Then, impact ionisation appeared to be the detection method yielding the highest sensitivity for the detection of dust particles in space (Auer, 2001).

When a dust particle impacts onto a solid target, parts of the impactor and the target are vaporized and ionised by the energy released during the impact. This leads to the formation of an impact plasma, expanding rapidly in the surrounding vacuum. The constituents of the impact plasma are electrons, positive and negative ions, neutral atoms or molecules, and residual fragments of the impactor and target. These fragments, called secondary ejecta, are likely to strike other surfaces of the instrument and produce secondary ions, electrons and debris. The cascade of processes involved in the impact ionisation theory are not well understood so far. However, the empirical knowledge about impact ionisation has been greatly improved in the last decades, through experimental works (Dietzel et al., 1973; Göller and Grün, 1989; Srama, 2000a; Stübig, 2002). A comparison with other ionisation mechanisms is discussed in Kissel (1987).

Different regimes of impact ionisation were identified, depending on the impact velocity. At small velocities (a few kms^{-1}), the dust material surface is heated by the impact energy, leading to surface thermal ionisation only. For higher impact speeds, a partial volume ionisation appears: fragments of the dust particles are totally vaporized but only partially ionized, since a fraction of the impact energy is required for the vaporization processes. With increasing impact velocities, volume ionisation is dominant and most of the initial dust material is ionized. Note, that for the same impact velocity, the total ion yield were found to be proportional to the particle's mass.

2.2 Instrumental setup

The first dust instrument based on the impact detection method was flown on the *HEOS 2* spacecraft in 1972. Two years later, in 1974, the *Helios* spacecraft was launched, also carrying a dust instrument based on impact ionisation. The descendants of the *HEOS 2* dust instrument were launched in 1989 and 1990 on board of the *Galileo* and *Ulysses* spacecraft, respectively. The last upgrade of these dust instrument is carried by the *Cassini* spacecraft, currently on its way to the Saturnian system. The results presented in this thesis are based on the data analysis of the IID subsystems of the *Helios*, *Ulysses*, *Galileo* and *Cassini* dust instruments.

The main goal of the IID setups described in the following is to measure the impact velocity and the mass of a dust grain. In addition, rough estimation on the impact velocity vector direction is given by the instrument orientation at the impact time. All the IID systems described here have a metal target plate and charge collectors (a metal grid) for electrons and ions. A material with a high electron yield is preferred for the target, in general gold. As the target and the charge collectors are set to different potentials, able to separate the positively and negatively charges of the impact plasma. The collectors are coupled with charge sensitive amplifiers. Those latter provides electrical signals monitoring the plasma generation.

2.2.1 The HELIOS dust instrument

In case of the *Helios* instrument, the target is a simple jalousie (see Fig. 2.1). A positively charged grid in front of the target collects the electrons formed upon the impact. A negatively charged grid behind the target collect the charge induced by the accelerated positive ions, flying to the multiplier subsystem. The 80 cm drift tube between the ion grid and the multiplier provides time-of-flight mass spectra with a resolution of $\frac{M}{\Delta M} \sim 5$. Two almost identical instruments were carried by a *Helios* spacecraft. Note that there were 2 *Helios* spacecrafts but only one provided useful in-situ dust data. The second *Helios* dust instrument suffered from an increased noise background. One instrument pointing is the direction of the ecliptic plane while the second one is pointed

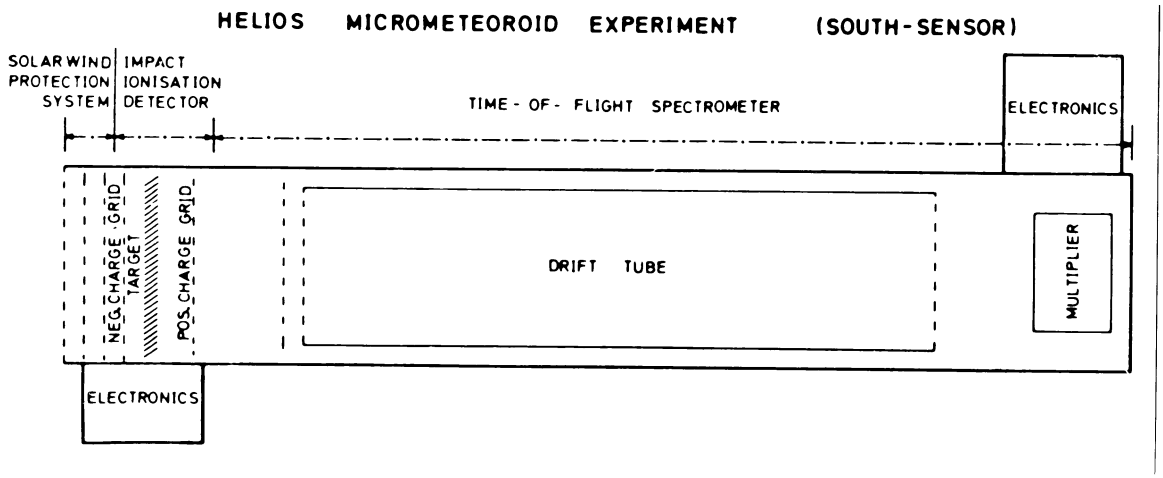

Figure 2.1: Schematic of the Helios dust instrument, including two subsystems: the impact ionisation detector and a time-of-flight mass spectrometer

toward the ecliptic south. The target area is 54.5 cm^2 for the so-called 'ecliptic sensor' and 66.5 cm^2 for the 'south sensor', see Sec. 4.4.1.

2.2.2 The ULYSSES-GALILEO dust instrument

The next instrument, carried by the *Ulysses* and *Galileo* spacecraft, is shown in Fig. 2.2. The main improvement of the detection technique resides in a semi-circular gold target. As mentioned in Sec. 2.1, only a fraction of the dust particle is vaporized and ionised upon the impact. Secondary ejecta which are also produced are lost in case of a flat plate-shaped target, resulting in a low ion yield. In contrast, a semi-circular target ensures that the ejecta impact other locations of the target and thus produce a secondary impact plasma. This allows a larger amount of the initial grain mass to be vaporized. Note that for this type of instrument, the electron collector is the target itself. The ion collector consists of a negatively charged grid, set to a potential of -350V, whilst the target is at ground. The nominal sensor field-of-view is a cone with half aperture angle of 70° with respect to the main symmetry axis of the detector. The total target area is 0.1 m^2, which is a great improvement compared to the target surface of the *Helios* twin instruments.

The quality of a dust impact is estimated by an impact classification scheme (Grün et al., 1995c). Impacts are classified into four quality classes (referred in the following as CLN 0-3), defined by various criteria on the electrical signals provided by the charge amplifiers. For a detailed review of the impact classification scheme, see (Grün et al.,

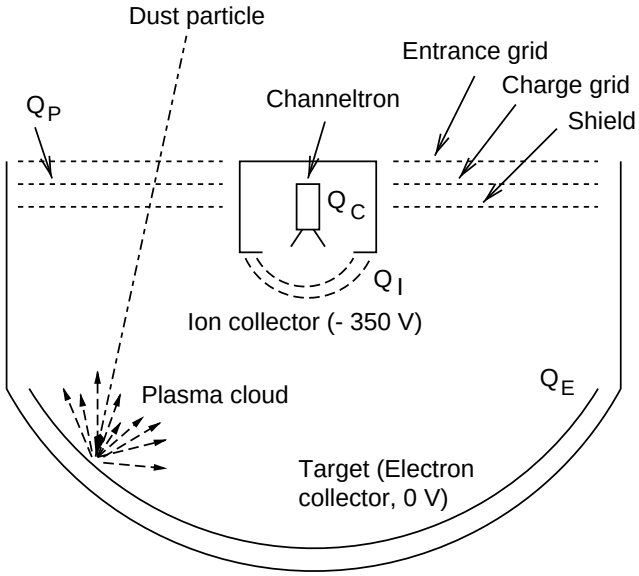

Figure 2.2: Schematic sensor configuration of the *Ulysses* and *Galileo* sensor. An impacting dust grain and the resulting plasma cloud are also represented.

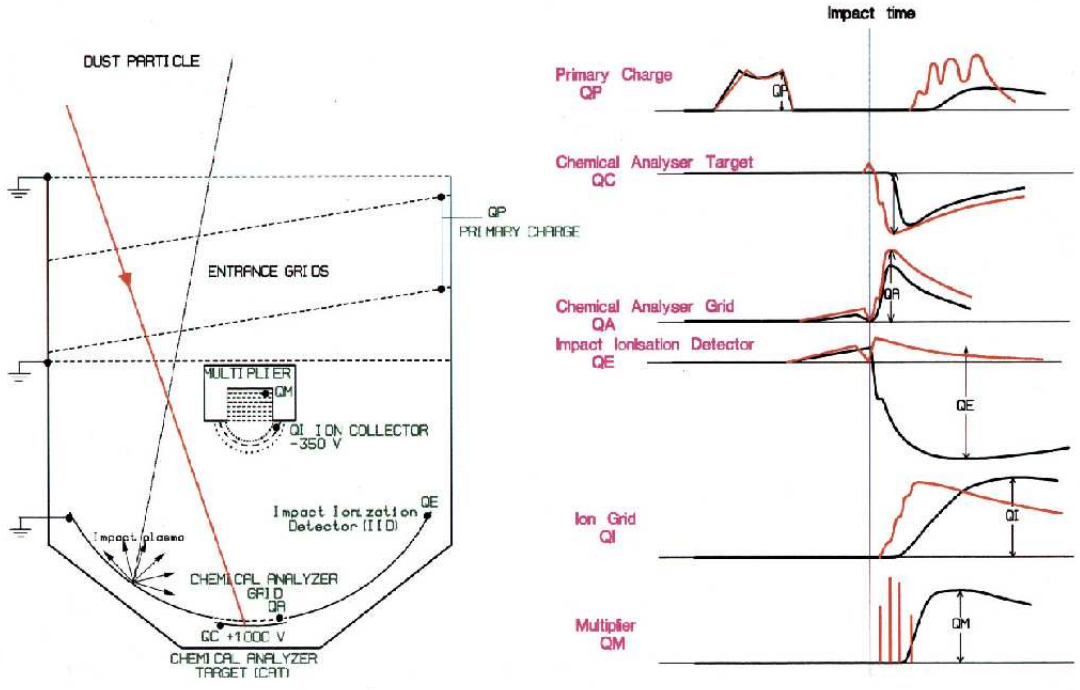

Figure 2.3: The IID subsystem of the *Cassini* dust detector. Impacts on the gold (dark line) or rhodium target (red line) are represented. On the right hand side, the resulting impact charge signals on each channel are plotted. From Srama, (2000a)

1992a). In general, Class 0 includes all signals not categorised in a higher class. This class may contain noise events or the 'exotic' impacts, like impacts onto the sensor's internal structure other than the impact target. In the higher classes CLN 1-3 the criteria that the electric signals have to fulfill become increasingly restrictive so that CLN 3 generally represents 'ideal' dust impact signals only. Criteria found by Baguhl (1993) allow to reliably distinguish between noise events and real dust impacts, even in low quality classes.

2.2.3 The CASSINI dust instrument

The Cosmic Dust Analyser (CDA), carried by the *Cassini* spacecraft is an upgrade of the *Galileo-Ulysses* instruments. For a detailed review of CDA, see (Srama, 2000b). However, the IID subsystem of CDA is not much different from the *Galileo* and *Ulysses* instruments. The major difference is that, in the CDA case, the grounded gold target is divided in two parts, see Fig. 2.3. A central rhodium target of 160 mm diameter, called the chemical analyser target, is designed to provide time-of-flight mass spectra (CA subsystem) with a resolution of about $\frac{M}{\Delta M} \sim 50$. In front of the rhodium target a positive charge grid gives an additional acceleration to the ions released upon impact on the chemical target. The total area of the impact target is 0.1 m^2, and the field-of-view 45 $^\circ$. Hence, the field-of-view of the *Cassini* instrument is somewhat lower than those of the *Ulysses-Galileo* instruments. This is caused by the side walls, extended to better protect the multiplier electronics against solar radiation and to incorporate the charge sensing grids (see the *Cassini* instrument schematic in Fig. 2.3). Note that CDA contains other subsystems: a high rate dust detector (HRD) and an instrument to measure the electric charge carried by the grains (noted QP in Fig. 2.3).

2.3 Calibration

The primary goal of an IID system is to *detect* a genuine dust particle impact. A measurement cycle is initiated when one of the electrical channels registers charges exceeding a threshold value. This is recognized by the instrument software as an *event*, and the resulting data are stored. Therefore, the instrument has to separate a *noise events* and *impact events*. For all the dust instruments used in this thesis, the impact identification relies on so-called 'multi-coincidence criteria': a genuine dust impact is identified when both the ion charge signal and the electron charge signal exceed their threshold value within a given time interval. The detailed identification scheme for the *Helios* dust experiment is given in Grün (1981), and for *Ulysses* and *Galileo* in Grün (1992a; 1992b). In the case of the *Cassini* dust instrument, one can additionally identify impact events using the transmitted charge signal curves. Therefore, a direct comparison with the impact charge signals obtained during the instrument calibration is possible.

Then, the IID systems have to provide the mass and the velocity of the impactor. It has been found empirically in dust accelerator tests that the rise time of the charge signals depends only on the impact speed of the projectile and is independent of the projectile mass (Dietzel et al., 1973). This behavior was confirmed by all the calibration experiments performed for the *Helios*, *Ulysses*, *Galileo* and *Cassini* dust instruments (Grün, 1981; Grün et al., 1992a; Grün et al., 1992b; Srama, 2000a; Stübig, 2002). According to these works, the rise time t of both the electron and the ion charge signals are functions of the impact velocity v only, and may be expressed as

$$t \sim k v^{\mu}, \tag{2.1}$$

where the parameters k and μ are characteristic for each instrument and each channel. These parameters are found through extensive calibration measurements. As I use the rise time calibration only for the *Cassini* data analysis, I provide the parameter values in the corresponding section. For the other missions, I refer the reader to the calibration papers mentioned above.

The total amount of charge Q released upon the impact depends, however, both on the particle's mass m and its impact velocity v. The elemental composition of the particle also plays a role. An empirical formula was derived, that appeared to fit well the calibration measurements:

$$Q = K \cdot m^{\alpha} v^{\beta}. \tag{2.2}$$

Experiments carried out with different projectile materials proved that $\alpha \approx 1$. This was verified by Dietzel (1973) for the *Helios* IID subsystem, by Goeller (1989) for the *Ulysses* and *Galileo* dust instrument and also by Srama (2000b) and by Stuebig (2002) for the *Cassini* instrument. The dependence of the impact charge yield upon the impact velocity is more complicated, depending on the ionisation regime mentioned in Sec. 2.1. At low speeds ($v \leq 10$ kms^{-1}), β was found to range from 2.5 to 3.5 (Dietzel et al., 1973; Göller and Grün, 1989; Stübig, 2002). For higher impact speeds, the value of β may be higher, up to 5.2. (Göller and Grün, 1989; Stübig, 2002). I give in Tab. 2.1, for each dust instrument, the coefficients α and β for Eq. 2.2 used in the data analysis to connect the mass and impact velocity value to the ion charge yield. As I had to deal mostly with high impact velocity, only values of the parameters K, α, and β for $v > 15$ kms^{-1} are given.

Once the particle's speed is known, the mass can be determined from the ion charge yields $\frac{Q_i}{m}$ and the electron charge yield $\frac{Q_e}{m}$. Thus, two independent estimates of the mass m_i and m_e can be derived. In case of the *Helios*, *Galileo*, and *Ulysses* dust detectors, the measured mass is given as the geometric mean of these two values, $m = \sqrt{m_i m_e}$ (Grün et al., 1992a; Grün et al., 1992b). From this follows that the impact speed measurement is crucial for the mass determination. In a nominal impact case, when the impact speed is derived from the rise-time, the error factor on the mass measurement is about a factor

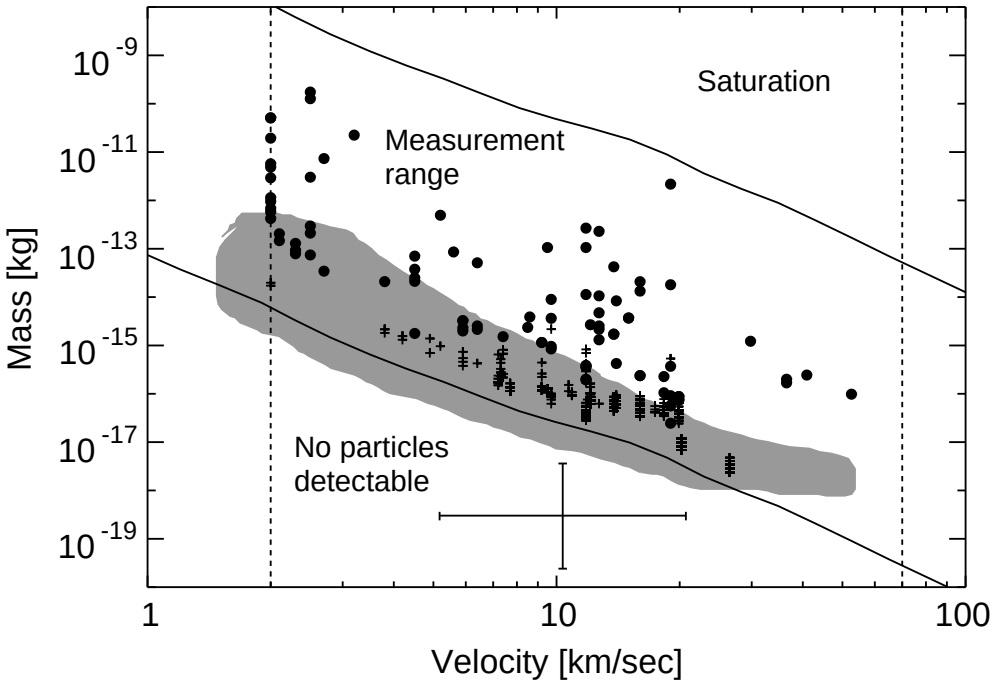

Figure 2.4: Calibrated mass and speed range of the *Galileo* dust detector. In the region marked 'Saturation' the instrument operates as a threshold detector. The shaded area shows the range where the instrument was calibrated in the laboratory. The bottom cross represents typical accuracies of speed and mass values. Plus signs and solid circles show the calibrated masses and speeds of 5353 particles measured in 1996. Plot from Gruen et al.(1992b) and Krueger's private communication.

10.

The sensitivity of an IID system is determined by its impact charge detection threshold which is about 10^{-14}C for all dust instruments used in this work. The velocity of the dust grains relative to the spacecraft plays a crucial rule in the detection sensitivity. For instance, assuming an impact velocity of 20 kms^{-1}, this allows the detection of dust grains with masses about 10^{-17}kg (see Fig. 2.4). Assuming a grain density of 2500 kgm^{-3}, this corresponds to grain radii of about 0.1 μm. In agreement with Eq. 2.2, smaller grains can be detected for higher impact velocities. The upper impact charge threshold is about 10^{-10}C for the *Helios* IID sub-system, and about 10^{-8}C for the other dust detectors. The latter value corresponds to a particle mass of 10^{-11}kg or $\approx$10 μm radius. The mass of impactors leading to impact charges higher than the upper value ('saturation range', see Fig. 2.4) will be underestimated.

The calibrations of all the IID systems used in this thesis have been performed at the Heidelberg dust accelerator facility. However, an important calibration problem should be noted. The dust acceleration technique employed uses the electrostatic charging of

	K	α	β	Reference
HELIOS	$4.07 \cdot 10^{-5}$	1	2.7	(Grün, 1981)
GALILEO	$1.5 \cdot 10^{-4}$	1	5.2	derived from (Göller and Grün, 1989)
ULYSSES	$1.5 \cdot 10^{-4}$	1	5.2	derived from (Göller and Grün, 1989)
CASSINI	$2.5 \cdot 10^{-4}$	1	5.0	(Srama, 2000a; Stübig, 2002)

Table 2.1: Values of the parameter K, α, and β for the ion charge yield calibration of each dust instrument. Only the parameter values for high impact velocity ($v > 15$ kms^{-1}) are given.

dust grains. This implies a dependence between the particle mass m_d and the particle speed v_d of the test particles of $m_d \sim 1.1 \cdot 10^{-12} v_d^{-3.4}$. This means that big impactors, with masses above 10^{-16}kg, could not be accelerated to speed higher than 30 kms^{-1}. This caveat is reflected by the calibration shown in Fig. 2.4. The higher the impact velocity, the smaller the mass range of particles that can be accelerated. However, a few calibration points for more massive particles (mass value above 10^{-11}kg), obtained from shots with the Munich plasma accelerator by Goeller et al. (1989) still confirm a linear dependence between the particle's mass and the charge yield. I call in the following high energetic impacts the impacts caused by projectiles with velocities and mass values outside the calibration range, typically, $v_d >$50 kms^{-1} and $m_d > 10^{-16}$ kg. In particular, the impact velocity and mass values given by the instruments for such impactors have to be interpreted very carefully.

2.4 High energetic impacts

The impact energy of a dust grain is equal to its kinetic energy in the spacecraft reference frame. Two kinds of problems appear for big and fast impactors. First, for the same particle mass, the higher the impact velocity v, the higher is the probability of ejecta cascades, see Sec. 2.1. In case of the *Galileo*, *Ulysses* and *Cassini* semi-spherical shaped targets, each ejecta may produce secondary impact plasma clouds. These secondary electrons and ions will be collected as well, and thus increase the rise time of the impact charge signal. This effect generally leads to an underestimation of the impact velocity, in agreement with Eq. 2.1. Consequently, this leads to an overestimation of the impactor mass, see Eq. 2.2.

A second problem may occur due to the saturation of one or both of the impact charge channels. For the same particle mass, the higher the impact velocity, the bigger is the amount of impact charge produced. It has been found experimentally that the ion collection efficiency is only 1% to 10% of the electron collection efficiency (Grün, 1981). Furthermore, the ratio of the ion charge yield *QI* to the electron charge yield *QE*

appears to be a function of v

$$\frac{QI}{QE} \sim v^{\beta}, \tag{2.3}$$

with $\beta = -1.7$ in case of the *Helios* instrument (Grün, 1981). Thus, in case of fast and big grains, the electron channel is more likely to saturate than the ion channel and may introduce an underestimation of the mass measurement (see Sec. 2.3).

The physics of impact plasma is still largely not understood. In particular, the separation mechanism of the plasma charges by an external electric field may be problematic. An external field will be able to separate the positive ions from the electrons only if the Debye length λ_D of the plasma cloud becomes greater than the typical length scale of the applied electric field (say the distance from the target to the ion collector). In the opposite case, the ions charges are shielded by the electron cloud. During the first 1 μs of the plasma existence, the plasma is in local thermodynamic equilibrium (Hornung and Drapatz, 1980). The Debye length is given by $\lambda_D = \sqrt{\frac{\varepsilon_0 kT}{ne^2}}$, where n is the electrons density, k the Boltzmann constant and e the electronic charge. If we assume the expansion of the plasma in the vacuum to be adiabatic the temperature T is a constant. If r is the plasma cloud radius, n decreases as r^{-3} and λ_D increases as $r^{\frac{3}{2}}$. As the ion grid is located far away from the impact location, the collection of the ions will start as soon as the plasma has sufficiently expanded. In contrast, the electron collectors are located directly on the target. This may bias the electron collection due to local plasma on the electron grid.

I want to stress here the fact that none of the undesirable effects discussed above can be proved experimentally, because of the difficulty to accelerate big impactors at high speeds in the laboratory. Experiments aiming at better understanding the behavior of plasma obtained by illuminating a solid target with a laser have already been performed by Mulser (1971) or are ongoing, but there is still a doubt that this can reproduce high energetic impacts of dust grains. However, it will simulate the generation of big, dense plasma clouds.

The undesirable effects described above may lead to a non-nominal response of the dust instruments in case of high energetic impacts. This should be kept in mind throughout the data analysis performed in this thesis. In particular, the ion channel will be considered as the most reliable for the impact charge measurement, since it is less affected by side effects. In contrast, the impact speed determination based on the rise time method will not be trusted in case of high energetic impactors. As a whole, the impact speeds and mass values provided by the different instruments will be interpreted with caution. However, based on the results of the data analysis, I will make effort to find out evidences for non-nominal responses of the instrument in case of high energetic impacts.

3 Dust in the inner Solar System

In this chapter I introduce dust populations that I will deal with throughout this thesis. In the first part of the chapter, I give an overview about dust dynamics, needed for the understanding of the data analysis. I first focus on the forces acting on dust grains in the Solar System, regardless of the grain size. Then, from a comparison of the relative strength of these forces for micrometer size particles, I consider only forces relevant for my analysis. In the second part of the chapter follows a brief description of the two main dust populations found in the solar system: the interplanetary dust particles (IDPs) and interstellar dust (ISD). The properties of the IDPs have been inferred from observations performed during the last decades through in-situ or remote optical sensing. In contrast, most of the knowledge about the ISD in the solar system has been obtained from only 10 years of in-situ monitoring of the ISD stream by the *Ulysses* spacecraft.

3.1 Dust Dynamics

The forces likely to influence the dust grain dynamics result from the various interactions between a dust grain and its environment. The forces are:

1. The gravitation forces
   - solar gravity
   - planetary perturbations
2. Forces due to interactions with the Sun light
   - radiation pressure
   - Pointing-Robertson drag
   - Yarkowsky effect
3. Forces due to interactions with the solar wind
   - Lorentz forces
   - solar wind corpuscular drag

The following description of the forces is made with respect to a heliocentric reference frame, for example the so-called ECLJ2000 reference frame, where the X-axis is the vernal equinox direction and the Z-axis the ecliptic north direction.

Gravitation forces The gravitation sources in the Solar System are potentially all massive bodies. As the Sun concentrates more than 99% of the Solar System mass, it is the major source of gravity. Planetary perturbations may occur if the dust grain penetrates inside the influence sphere of a planet. Let us consider a planet of mass M_p, located at the distance D from the Sun. Then, $r_i = D(\frac{M_p}{M_\odot})^{\frac{2}{5}}$ is the radius of its influence sphere. Per definition, outside of the influence sphere of the planet, the perturbating influence can be neglected. In the case of the gas giant Jupiter, located about 5 AU from the Sun and responsible for many secular perturbations of small bodies in the solar system, $r_i \approx 0.3$ AU. Therefore, the gravitative influence of Jupiter will be neglected in the following for calculations in the inner solar system. As the other planets are much less massive, their perturbation will also not be taken into account. The gravitation force acting on a dust grain of mass m_d located in the solar gravitation field is given by:

$$\mathbf{F_g} = \frac{-GM_\odot m_d}{|\mathbf{r}|^3}\mathbf{r} \tag{3.1}$$

Thus the equation of motion is

$$\ddot{\mathbf{r}} = -\frac{GM_\odot}{|\mathbf{r}|^3}\mathbf{r}, \tag{3.2}$$

where $M_\odot$ is the Sun's mass and G the gravitational constant.

Radiation pressure Radiation pressure is caused by the momentum transfer between the solar photons hitting a dust grain. This force acts in a radial direction and depends on the wavelength of the incident light, the heliocentric distance, the optical surface properties and the grain shape. The momentum p_ν of the photon for the frequency ν is $\frac{h\nu}{c}$ with h the Planck constant and c the light speed. The associated force is $F_{rad} = \dot{p}_\nu = \frac{P_\odot(\nu)}{c}$, where $P_\odot(\nu)$ is the power emitted by the Sun at the frequency ν. The decrease of this power as the square of the heliocentric distance r, the scattering of light, and the solar Planck curve are taken into account in the following expression of the radiation pressure force onto a grain of cross section S

$$\mathbf{F}_{rad}(\mathbf{r}) = \frac{P_\odot S Q_{pr}}{|\mathbf{r}|^3 c}\mathbf{r}, \tag{3.3}$$

Q_{pr} being the efficiency factor for radiation pressure weighted by the solar spectrum and $P_\odot$ the bolometric solar power.

Poynting-Robertson drag The Poynting-Robertson drag is caused by the motion of the dust particle in the inertial reference frame. In the dust grain frame, the photons responsible for the radiation pressure are seen with a (small) aberration angle with respect to the Sun direction. This results in a tangential component of the radiation pressure force, acting in the direction opposite to the particle's motion. This drag force

is responsible for continuous loss of the grain orbital energy and angular momentum leading to a reduction of its semi-major axis and eccentricity. The trajectory of the particle in the heliocentric frame becomes a spiral toward the Sun, where the grain finally evaporates. The time scale needed by a dust grain of sub-micrometer size, starting from 1 AU, to reach the Sun is about 1000 y (Gustafson, 1994). As this characteristic time scale is big compared to the short measurement time periods considered in this work, I will assume that the Pointing-Robertson drag has no influence on the dynamics of the dust grains considered.

Yarkowsky effect The Yarkowsky effect, acting on rotating bodies, is due to an asymmetry of the thermal photon emission. Indeed, the hot 'evening' hemisphere radiates more thermal energy than the cool 'morning' hemisphere. The quantitative estimation of this effect is very complex, since it involves a thermal conduction dust model and assumptions of the spin state of the particle. The influence on the dust trajectory is also difficult to foresee, because it depends on the orientation of the rotation spin axis of the dust grain relative to the momentum direction. Nonetheless, the Yarkowsky force is a tangential force that may add to the Poynting-Robertson drag or reduce it. For particles of micrometer sizes, the Yarkowsky force becomes negligible compared to the Poynting-Robertson drag and will also be neglected.

Solar wind drag The solar wind is responsible for corpuscular forces, due to collision and transfer of momentum from the solar wind protons onto a dust grain. Their interaction is therefore analogous to radiation forces, depending on the cross section of the dust grain, the surface chemical composition and the proton momentum flux density. Because of the dilution of the proton number density as r^{-2}, the solar wind proton interaction intensity decreases like the radiation pressure for increasing heliocentric distances. Therefore, the ratio between the proton pressure and the radiation pressure is independent of r and has been found from in-situ measurements at 1AU to be about 10^{-4} (Gustafson, 1994). In the following, I assume that the solar wind corpuscular pressure is negligible compared to sunlight radiation pressure.

Lorentz forces Dust grains in the heliosphere are charged. One important charging process is the photo-effect, leading to the emission of electrons from dust grains by UV photons. Furthermore, shocks of high energetic charged particles onto the dust grain may lead to secondary electron emission. Photo-effect and secondary electron emission are therefore responsible for a positive charging of the dust grain. A negative charging process consists of the interaction of the dust grain with the currents in the ambient interplanetary plasma. As electrons have the same number density as the ions (to respect the global charge balance in the plasma), but much smaller masses, the electron current is dominant and results in a negative charging of the dust grain, by electrons sticking.

As the UV-photoeffect dominates in interplanetary space, an electrostatic equilibrium potential about +5 V has been derived (Horányi, 1996), independent of the heliocentric distance. Due to their charge, dust grains in interplanetary space couple with the interplanetary magnetic field (IMF) frozen in the solar wind plasma. The Lorentz force on a charge q moving with the velocity $\mathbf{v}$ relative to the field $\mathbf{B}$ is

$$\mathbf{F_L} = q\mathbf{v} \times \mathbf{B} \tag{3.4}$$

The magnetic field $\mathbf{B}$ is convected by the solar wind at the speed $\mathbf{v_{sw}}$ in the heliocentric frame. If $\mathbf{v_g}$ is the heliocentric grain velocity, the Lorentz force becomes

$$\mathbf{F_L} = q(\mathbf{v_g} + \mathbf{v_{sw}}) \times \mathbf{B} \tag{3.5}$$

As the solar wind speed is about 300-400 kms^{-1} at low ecliptic latitude and even higher at high ecliptic latitude, $v_g \ll v_{sw}$ so that the expression of $\mathbf{F_L}$ can be approximated by

$$\mathbf{F_L} = q\mathbf{v_{sw}} \times \mathbf{B} \tag{3.6}$$

The IMF is well described by the Parker's spiral model (Parker, 1958). At r_0= 1AU, $B_{r0} \approx B_{\phi 0} \approx$3 nT, $B_{\theta 0} \approx 0$ with $B_{r0}, B_{\phi 0}, B_{\theta 0}$ being respectively, the radial, azimuthal, and the normal component averaged over one solar rotation. At the heliocentric distance r and latitude θ, the IMF components are

$$\{B_r, B_\phi, B_\theta\} = \{B_{r0} r^{-2}, B_{\phi 0} \cos(\phi) r^{-1}, 0\} \tag{3.7}$$

Thus, far away from the Sun, the IMF is azimuthal. As the solar wind expands radially, the resulting Lorentz force on a dust grain is perpendicular to the solar equator, toward the north or the south direction, depending on the IMF polarity. As the IMF polarity is time variable, depending on the solar activity, the resulting Lorentz force is equivalent to the action of a time varying electric field $\mathbf{E}$, perpendicular to the Sun equatorial plane.

Due to the instruments sensitivity, the mass of the particles studied in this work ranges from 10^{-17}kg to 10^{-11}kg (see Sec. 2.3). Assuming the mean density of dust grains to be about 2500 kgm^{-3} (Grün et al., 1985), the dust grains size ranges from 0.1 μm to 1 μm. As a whole, only the first order forces of gravity, light pressure, and electromagnetic interactions are relevant for our analysis. The relative influence of those different forces onto the grains dynamics is dependent on the location of the particle in the solar system, the particle's size, its charge, and on its material parameters (shape and chemical composition). It is common to introduce the β-ratio between the forces due to gravitation and radiation pressure, in order to evaluate their relative strength. Thus, the general equation of motion for a dust grain can be written

$$\ddot{\mathbf{r}} = -\frac{G(1-\beta)}{|\mathbf{r}|^3}\dot{\mathbf{r}} + \frac{q}{m}\mathbf{E}, \tag{3.8}$$

As the charge of the grain does not depend on the grain size, big grains have $\frac{q}{m} \ll 1$. Therefore, their trajectory is elliptical or hyperbolic and fully determined by the injection velocity vector of the particle into the force field. For smaller grains, the Lorentz

term can not be neglected any longer and may deflect the dust particle toward or outward the Sun's equatorial plane.

Because of the same dependence of the gravitation and radiation pressure forces on the heliocentric distance, the β-ratio is independent of **r** and is a function of parameters like the grain radius, the grain chemical composition, the grain shape and the grain material density. From Eq. 3.1 and Eq. 3.3 the expression of the β-ratio can be derived:

$$\beta = \frac{|\mathbf{F_{rad}}|}{|\mathbf{F_G}|} = \frac{Q_{pr} S P_\odot}{G M_\odot m_d c} \tag{3.9}$$

For the purpose of this thesis the β-values given in Gustafson (1994) were used (see Fig. 3.1). It is important to note that the choice of the $\beta(m_d)$ function constrains the material properties of the dust grains. In particular, the curve shown in Fig. 3.1 requires a compact and spherical shape for the particles, together with the optical properties of 'astronomical silicates' (see (Draine and Lee, 1984)). In addition, a typical value of 2500 kgm^{-3} is assumed for the dust grain bulk density ρ. This model of dust grain (used in the following for both the IDP and ISD populations) is a working hypothesis whose implications will be discussed in details in Sec. 5.4. However, it should be mentioned here that this model may not be too far from the reality and allows to reproduce key features of the zodiacal light scattering (Giese, 1973). Note that for this model of dust grains, the radiation pressure can balance ($\beta \approx 1$) or even exceed the effect of the gravity ($\beta > 1$).

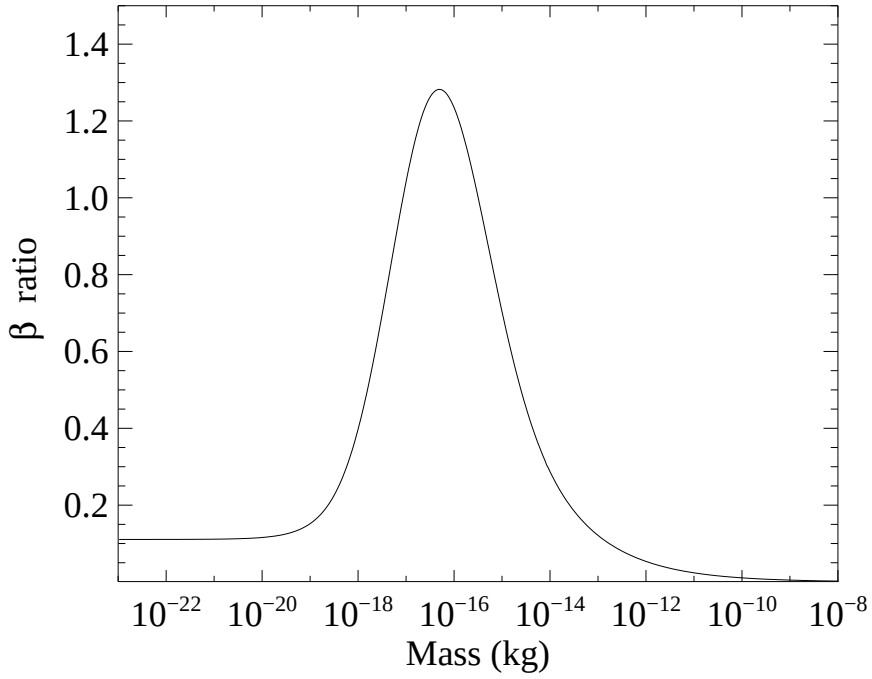

Figure 3.1: Ratio of radiation pressure to gravitational force β, calculated as function of the particle mass. The shape of the particle is assumed to be spherical and homogeneous. The optical properties are those calculated for astronomical silicates. The results presented here, calculated with the Mie theory, are taken from Gustafson (1994).

3.2 Dust in the inner solar system

Dust grains found in our solar system are either of interplanetary or of interstellar origin. The two groups of micro-meteoroids differ with respect to their origin, their dynamics, and their elemental composition.

To help understanding the in-situ detection probability of IDPs and ISD grains, I now briefly summarise the current understanding of the solar system dust environment. Please note that the following description refers to the in-situ dust detection method, based on impact dust detectors flown in the past on various spacecrafts. Therefore, the dust model description used in the following is valid inside the frame of the data obtained by the micro-meteoroids experiments during milestone missions like *Cassini*, *Galileo*, *Ulysses* or *Helios* (Grün et al., 1993; Grün et al., 1995a; Grün et al., 1995b). The data sets cover a heliocentric distance range between 0.3 and 5 AU. As an im-

mediate consequence of the dust impact detection method, only the sub-micrometer or micrometer grain size range is relevant for the instruments. However, even in this quite narrow size range, various dust populations were identified and their interactions with the solar system environment were studied.

3.2.1 Interplanetary dust particles

IDPs are mostly on gravitationally bound orbits and may originate from various interplanetary sources as comets, asteroids, or even the volcanoes of Jupiter's moon Io (Grün et al., 1993). The IDPs mass distribution as well as the distribution of their orbital elements is governed by the competition between IDP generation and destruction. A major mechanism for replenishing IDPs are successive collisions between parent bodies (e.g in the asteroid belt). On the other hand, IDPs may be removed by drag forces (Poynting–Robertson drag or radiation pressure) or even physically destroyed by sputtering through solar wind particles. Since the advent of in-situ dust detection, an impressive amount of interplanetary dust data has been collected. During the recent decade, attempts were made to develop a micro-meteoroid model capable of reproducing the observed data as well as describing the physical processes involved in the evolution of size and orbital elements of the IDPs (Divine, 1993; Grün et al., 1997; Staubach et al., 1997). The basic idea of those models is to describe the dust distribution in the interplanetary space mathematically by a superposition of a few populations, each having separable distributions in mass and orbital elements. As this model aims at providing roughly (and non time dependent) predictions on the flux observed by spacecrafts at given locations in the solar system, some simplifications were made. In this approach, non-gravitational forces, planetary perturbations, and time-dependent processes like the coupling with the IMF were omitted. Furthermore, regarding the orbital elements of the IDP populations, the following assumptions were made:

a- The IDPs are supposed to be on bound prograde heliocentric trajectories.

b- The IDPs have low-inclined orbits (up to 30°)

c- The argument of perihelion ω is assumed to be equally distributed in $[0,2\pi]$

d- The longitude of ascending node Ω is assumed to be equally distributed in $[0,2\pi]$,

The first assumption can be justified by the following fact: if one assumes the same dust number density, a spacecraft flying in the prograde direction should observe a much higher flux of particles on retrograde orbits than on prograde orbits. However, none of the previous in-situ experiments detected a significant amount of retrograde dust particles, as reported in the analysis of the *HEOS 2* or *Helios* measurements (Hoffmann et al., 1975; Grün, 1981).

In the Staubach model (Staubach et al., 2001), the biggest particles ($m > 10^{-13}$kg) are separated into the *core* population and *asteroidal* population, both characterised by small to moderate eccentricities and small inclinations. The dynamics of these grains is dominated by gravity forces. In contrast, for smaller particles with masses between 10^{-21} kg and 10^{-13} kg, the influence of the radiation pressure on their dynamics cannot be neglected, see Fig. 3.1. These particles are attributed to one of the populations *A*, *B*, or *C* and move in low inclination orbits (see Tab. 3.1). The eccentricity distributions for these populations are bimodal, characterised by a peak at low eccentricities as well as by a major component at high eccentricities.

population	mass [kg]	eccentricity	inclination [°]	β
asteroidal	10^{-6}	0.1...0.25	< 10	0
core	10^{-8}	0.1...0.25	< 10	0
A	10^{-14}	0...0.25; 0.8...0.98	< 20	0.3
B	10^{-16}	0...0.1; 0.8...0.98	< 20	0.8
C	$5 \cdot 10^{-18}$	0...0.1; 0.8...0.98	< 20	0.3

Table 3.1: Dust populations used by Staubach to fit observation data. The maximum of the mass distribution is given, together with the eccentricity and inclination ranges.

Generally, each population's mass distribution follows a power law with a negative exponent. In order to quantify the interplanetary flux at 1 AU, I will use for calculation purposes the estimation made by Grün (1985). In these calculations, the flux values are given as cumulative mean values (number of particles bigger than a given mass per time unit and surface unit). This model assumes a flat plate detector at 1 AU outside the gravitational influence of the Earth.

Interplanetary dust populations are also exposed to radiation pressure constraining the grains angular momentum. In the following, it will be crucial for our dynamical analysis to have an estimate of the most probable upper limit of the β-ratio for IDPs on bound orbits.

Only IDPs with $\beta < 1$ can maintain a bound orbit. Note, however, that even those IDPs might be unbound. We define $\mu = GM_\odot$, G being the gravitational constant, $M_\odot$ the solar mass and $\tilde{\mu} = (1-\beta)\mu$. A grain on a circular orbit of radius r_0 may be disrupted such as the new grains have $\beta < 1$. The injection velocity of the newly formed grains is assumed to be equal with the velocity V_0 of their parent body (usual case). As $V_0 = \sqrt{\frac{\mu}{r_0}}$, the new dust grains will maintain a bound orbit if $V_0 < V_e(\beta, r_0)$, where $V_e(\beta, r_0) = \sqrt{2}\sqrt{\frac{\tilde{\mu}}{r_0}}$ is the escape velocity at the grain location and for the given β ratio value. This condition may be written as

$$\sqrt{\frac{\mu}{r_0}} \leq \sqrt{(1-\beta)}\sqrt{2 \cdot \frac{\mu}{r_0}}, \tag{3.10}$$

leading to $\beta \leq 0.5$.

The assumption that the parent bodies have been moving in circular orbits turns out to be oversimplified. A parent body in a highly eccentric orbit may get disrupted at the aphelion of its trajectory, so that IDP grains with $0.5 < \beta < 1$ on bound orbit may exist. Indeed, assume a parent body on a highly eccentric bound orbit, of eccentricity e and semi-major axis a, and for which $\beta = \beta_0$. I assume that the parent body disrupts at the aphelion of its trajectory, creating two smaller new bodies. Thus, the new generation grains have a higher β value. The injection velocity V_i of the new bodies is equal to the velocity of the parent body at the aphelion, implying $V_i = \frac{\sqrt{1-\beta_0}}{\sqrt{1+e}} V_c$ where $V_c = \sqrt{\frac{\mu}{r_a}}$ is the circular velocity associated to the aphelion distance r_a, without radiation pressure. The escape velocity of the new generation grains is given therefore by $V_e(\beta, r_a) = \sqrt{2}\sqrt{1-\beta} V_c$. Thus, $V_i < V_e$ implies $\beta < 1 - \frac{\sqrt{1-\beta_0}}{2(1+e)}$. A numerical application with e =0.8 and β_0 =0.2 gives a possible upper limit value for β around 0.8. Note that in-situ evidences for such IDP populations with low angular momentum have been reported after analysis of the *Helios* spacecraft dust data (Grün and Zook, 1980). To take this into account, I will admit in my calculations β values for IDP impactors up to 0.8. Note, however, that this value is an upper limit. Indeed, collisions at perihelion are more likely since the spatial dust density and flux are there higher than at aphelion.

3.2.2 Interstellar dust particles

The first unambiguous in-situ detection of ISD grains succeeded with the *Ulysses* dust instrument (Grün et al., 1993). Since then, the *Ulysses* spacecraft has been monitoring the interstellar dust continuously, and has greatly improved our knowledge about the properties of the ISD found inside the heliosphere. It was proved that the heliosphere is continuously crossed by ISD grains, having heliocentric velocities exceeding the Solar System escape velocity (Grün et al., 1994). Within the *Ulysses* measurement accuracy, no significant deviation was found between the interstellar Helium and dust downstream direction (Baguhl et al., 1995; Witte et al., 1993; Landgraf, 1998). As a consequence, the observed grains are believed to be dynamically coupled to the interstellar gas.

In the J2000ECL reference frame, following values for the downstream direction of the ISD stream will be assumed in this thesis: 75° ecliptic longitude and -5° ecliptic latitude. The heliocentric injection velocity v_∞ of ISD is about 26 kms^{-1}, comparable with the velocity of the Sun relative to the LIC (Grün et al., 1994).

The dynamics of the grains in the LIC is crucial for the understanding of nucleation, growth and collisional destruction processes (Draine, 1990). These processes are strongly dependent on the relative velocities of the grains. Mainly, the phenomena responsible for the spread of velocities in the Local Interstellar Cloud (LIC) are the gas

drag, the interaction with the local interstellar magnetic field, the radiation pressure and the photoelectric emission (Frisch et al., 1999). The relative strengths of the different dynamic forces strongly depend on the size and the charge of the grains, together with local conditions in the LIC, like gas or magnetic field turbulences. However, within the *Ulysses* measurement accuracy, the ISD flux appeared to be well collimated, implying a weak stochastic velocity dispersion of individual ISD grains inside the stream.

ISD grains detected by *Ulysses* were dominantly found to have masses about $3{\cdot}10^{-16}$kg (Landgraf et al., 2000) corresponding to grain radii of about 0.3 μm. Optical observations of the ISM provided information on the size distribution of interstellar grains outside the heliosphere. If m is the mass of an interstellar dust grain and n the spatial distribution density associated to the m value, one gets the so-called MRN distribution (Mathis et al., 1977).

$$n(m) \propto (\frac{m}{m_0})^{-3.5}, \;\; m_0 \leq 1.6 \cdot 10^{-16} \;\; kg \tag{3.11}$$

However, most of the interstellar grains detected by *Ulysses* have masses in excess of the MRN cut-off mass m_0. To account for such particles, a modified size distribution has been proposed by Grün (1997). A possible filtration through the heliospheric interface of the small dust grains has been discussed (Linde and Gombosi, 2000). When the sun plasma carried by the solar wind encounters the interstellar plasma, a termination shock is formed. The ISD grains penetrating into the heliosphere have to cross this transition region, possibly leading to a rejection of the small ISD grains usually needed to fit the interstellar extinction curve.

The dynamics of the ISD grains inside the heliosphere is governed by Eq. 3.8. The typical q/m ratio of the interstellar grains observed by *Ulysses* has been found to be around 0.59 Ckg^{-1} (Landgraf et al., 2003). This implies a weak coupling of the major component of the ISD stream with the IMF, and the gyro-radius of those grains is about 3000 AU (Grün et al., 1994), much greater than the dimensions of the heliosphere. Thus, the influence of the IMF coupling on the trajectory is negligible. As a consequence, due to their high injection velocity, the trajectory of ISD grains inside the heliosphere is hyperbolic.

However, for smaller grains (radius smaller than 0.2 μm), the magnetic coupling results in a time variable flux due to the variable IMF, as observed by *Ulysses* (Landgraf et al., 2003). In general, the polarity of the IMF prevents the smaller grains to reach the innermost region of the solar system, explaining the lack of small interstellar grains in the in-situ data. Note that this filtering effect may be more or less strong, depending on the solar activity (Landgraf et al., 2003).

Another filtering effect of ISD grains in the heliosphere is caused by the solar radiation pressure forces. As can be seen from Eq. 3.8, radiation pressure weakens the effect of solar gravitation. The orbits of particles affected only by radiation pressure,

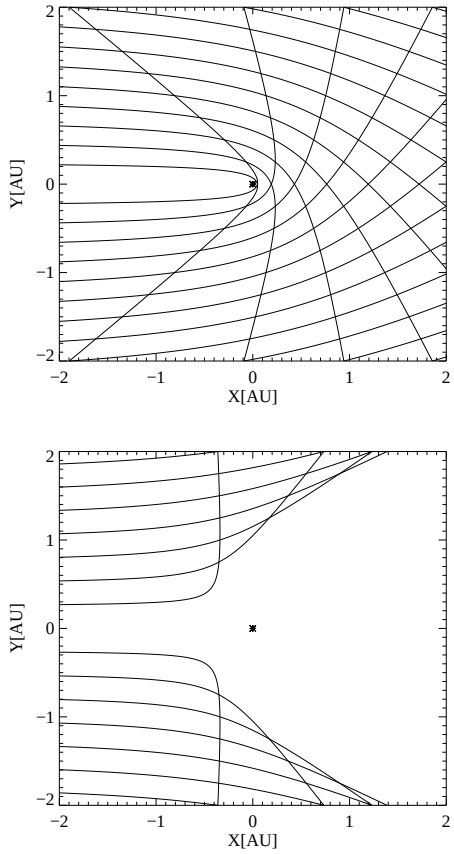

Figure 3.2: Trajectories of ISD grains in the ecliptic plane. The X-axis of the reference frame is parallel to the ISD stream injection velocity. Only the gravity and the radiation pressure have been taken into account. On the left side plot, β = 0.5, while on the right side plot, β = 1.2

however, remain hyperbolic. Three regimes of the radiation pressure strength on ISD grains can be distinguished. For $\beta < 1$, the gravity overcomes the effects of the radiation pressure. Dust grains are deflected toward the sun, the deflection angle being strongest when $\beta = 0$. For $\beta > 1$, the radiation pressure overcomes the effects of the gravitation. Dust grains are deflected away from the sun, and may be prevented from reaching small heliocentric distances, see Fig. 3.2. For $\beta \approx 1$, the radiation pressure and the gravity cancel each other. This is the case for interstellar dust grains with a grain radius about 0.3 μm, corresponding to a mass of $3 \cdot 10^{-16}$ kg see Fig. 3.1. As a consequence, such grains will pass through the solar system, without being deflected. Evidences for the radiation pressure filtering effects have been found in the *Ulysses* data (Landgraf, 1998): so called β-gap revealed a lack of grains in mass ranges corresponding to $\beta > 1$.

Fig. 3.2 suggests that the solar radiation shapes 'exclusion zones' inside which particles with $\beta > 1$ can not penetrate. The closest heliocentric distance that can be reached

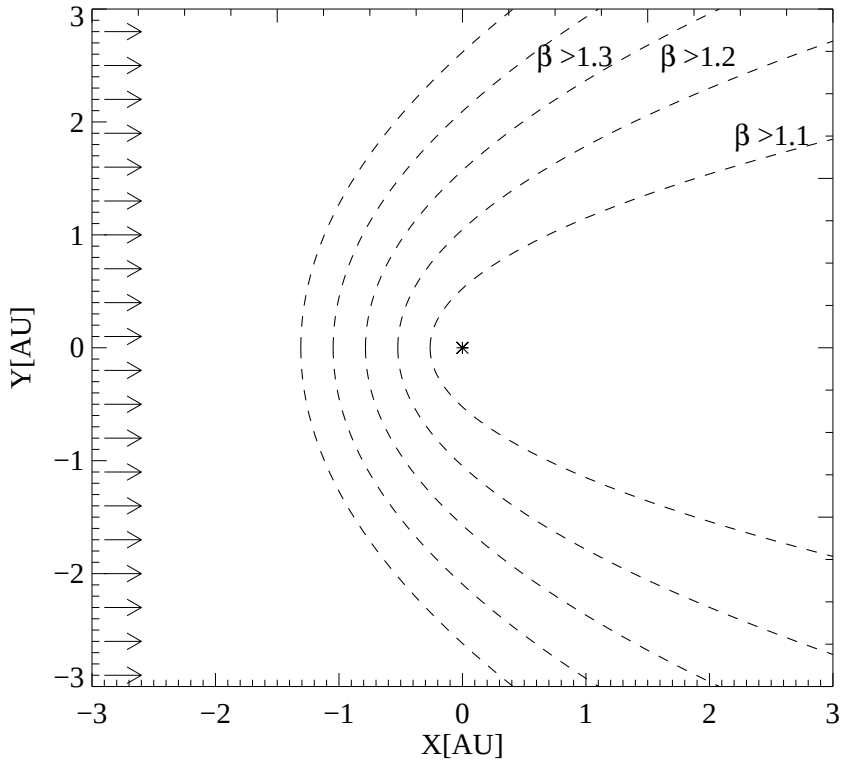

Figure 3.3: ISD exclusion zones shaped by the radiation pressure. The X-axis is parallel to the ISD stream injection direction. Each boundary line is associated to a value of the β ratio. ISD grains for which $\beta = \beta_i$ cannot penetrate inside the exclusion zone associated to β_i.

by an ISD grain is a function of its β-ratio value and the impact parameter of its hyperbolic trajectory (in Fig. 3.2, the impact parameter is simply $|Y_0|$, with $X_0 = -\infty$). A plot of the exclusion zones boundaries, for different values of the β ratio, is shown in Fig. 3.3. The theoretical calculation giving the polar equation of those exclusion zones is detailed in Appendix. A.1.

4 Data Analysis

All we currently know about the ISD stream inside the heliosphere has been inferred from in-situ measurements between 3 AU and 5 AU. I outlined in the previous chapter that, despite of heliospheric filtering effects, some components of the ISD stream should be able to reach even closer heliocentric distances. In particular, can one still find evidence at 1 AU of the ISD grains observed by *Ulysses* beyond 3 AU? Can one observe and quantify the filtering effects on the ISD stream at close heliocentric distances? These questions will be addressed in this chapter through the analysis of dust data obtained between 1974 and 2000 by the *Cassini*, *Galileo*, and *Helios* missions. I provide first a general description of the applied method to find evidences for the existence of ISD grains in the data sample obtained by these missions. Then follows a detailed analysis of each data set. In addition, the *Ulysses* ISD dust data previously analysed by Landgraf (1998) are also exploited to point out an interesting instrumental effect, that may have biased the measurement of the ISD flux and its dispersion width.

4.1 Method for ISD identification

The initial years of the *Cassini*, *Galileo* and *Ulysses* missions consisted of interplanetary cruises in the ecliptic plane, during which fly-by maneuvers were performed to increase the orbital energy of the spacecrafts. Also, *Helios* remained during all its mission duration on an elliptical orbit around the Sun within the ecliptic plane. As a consequence, all the dust impacts detected at heliocentric distances less than 2.5 AU have been detected within the ecliptic plane (see Fig. 4.1). Thus, the spacecraft's dusty environment was dominated by the IDPs described in Sec. 3.2.2. This implies an important problem I will have to face in my data analysis: how can I distinguish interplanetary impactors from potential interstellar impactors?

The dust data of the *Galileo*, *Ulysses* and *Helios* missions obtained in interplanetary space have already been extensively studied in previous works (Grün, 1981; Grün et al., 1992; Grün et al., 1995c). However, only the *Ulysses* data or the *Galileo* data obtained beyond 3 AU revealed the existence of the ISD stream as described in Sec. 3.2.2. Before the first identification of the ISD stream in 1993 by *Ulysses*, there was no reason to look for the ISD component in the dust data of *Helios* or *Galileo* in the inner solar system, since it was even not known if ISD could penetrate the heliosphere. Therefore, dust data analysis of all missions within 3 AU was focused exclusively on the description of IDP populations. Only *Ulysses* after its Jupiter fly-by had a highly inclined orbit around the Sun, that allowed to identify unambiguously the ISD component since only

little contribution was expected from the IDPs at high ecliptic latitude (see Tab. 3.1). In contrast, the *Helios*, *Galileo* and *Cassini* spacecrafts had trajectories within the ecliptic plane and never benefited from such favorable observation conditions. Therefore, for the in-situ observation of the ISD stream, efforts were concentrated on the interpretation of the *Ulysses* data only. However, I will show in this thesis that some orbit segments of the interplanetary probes mentioned above were favorable for ISD observation. Orbit segments were selected where the spacecraft had a high velocity relative to the ISD stream. As this implies the risk of a non nominal instrument response because of high energetic impacts, (see Sec. 2.4), the resulting underestimation of ISD grains impact velocity may explain why ISD has not be identified yet during the mentioned missions. The basic idea of the data analysis presented in this thesis is to discriminate ISD grains from IDPs using the ion charge yield released upon the impact.

The first step of the data analysis consists, for each mission, of identifying the orbit segments where the velocity of the spacecraft relative to the ISD stream was high. This condition was fulfilled if, for example, the spacecraft was flying toward the ISD upstream direction. Depending on the mission, this can results in impact velocities for ISD impactors up to 65 kms^{-1}. Then, knowing the sensitive area profile of the dust instrument, one can identify through geometric calculations the orbit segments and the instrument orientation for which the effective target area sensitive to the ISD stream does not vanish. Taking into account only those orbit segments and boresight directions allows to further constrain the data samples solely to impactors that *could* be ISD impactors.

An important hypothesis on the ISD grains is that they originate from a unique source, namely the ISD stream monitored by *Ulysses*. Therefore, the preliminary goal of the data analysis will be to find around 1 AU the impact charge signature of ISD grains similar to those detected by *Ulysses* beyond 3 AU. In particular, the ISD mass distribution measured by the *Ulysses* dust instrument sets constraints on the β-ratio of the grains (see Fig. 3.1). As shown in Fig. 3.1, to each β value correspond two mass values. However, I will systematically reject the smaller mass value, since the ISD grains corresponding to the left part of the curve have a higher $\frac{q}{m}$ ratio and therefore are prevented by Lorentz forces from reaching the inner solar system. The ion charge released during an impact is a function of the impact velocity and of the mass of the grains. As both, the mass and the impact velocity, are function of β, the ion charge yield for ISD can be written as a function of β only (for detailed explanations, see Appendix. A). Furthermore, the dominant contribution to the ISD stream was found to have $\beta \approx 1$ (Landgraf et al., 2000; Landgraf et al., 2003). Thus, a rough preliminary analysis consists of looking for impact charges in the data sample that *could* be indicative for ISD grains.

The second step consists of using the instrument field of view to find out the orbital element subsets of the IDPs that are the most likely to be detected. This provides a good estimation of the mean impact velocity expected for IDPs. Note that the IDP orbital dis-

tribution model used for this purpose is very simplified, as described in Sec. 3.2.1. In general, on the selected orbit segments, the expected impact velocity for ISD impactors is higher (up to a factor 3) than the mean impact velocities expected for IDPs. Indeed, all spacecrafts were on prograde orbits, like the IDPs, so that the relative velocities were rather small. Thus, for the same mass value, the impact velocity of ISD grains can lead to a higher ion charge yield than those for IDPs. The difference of the total ion charge released can be up to one order of magnitude.

Last but not least, the mass range of the IDPs likely to hit the detector has to be considered. Indeed, even if the impact velocities of IDPs are smaller than those of ISD grains, an interplanetary grain having a higher mass than an ISD grain can generate the same or even a higher ion charge. Therefore, strictly speaking, it is impossible to identify with certainty the origin of an impactor using the ion charge yield only. The identification is, however, statistically possible, using the following arguments.

First, the rough rotational symmetry of the zodiacal cloud implies a uniform distribution of the 'big' IDP impactors on a spacecraft orbiting the Sun. In contrast, the source for ISD grains is anisotropic because of the highly directional and collimated ISD stream. This results in an ISD contribution only when the detection conditions are favorable. Therefore, a non-symmetric distribution of high impact charges and an increased flux of strong impact charge yields are good indications that ISD grains contribute significantly to the data sample when the condition for the ISD detection are favorable. This argument is very powerful for the data analysis of missions like *Helios*, where the orbital elements of the spacecraft were time independent and the orbit was symmetric with respect to the ISD stream direction.

Second, the negative slope of the space density mass distribution $n(m)$ of IDPs (Sec. 3.2.1) implies a smaller impact probability of big IDP grains in a given measurement time. The number of impactors having a mass between m and $m+\delta m$ detected during the time period $t, t+\delta t$ is determined by the Poissonian statistics and is proportional to $n(m)$. Using the mass flux distribution model at 1 AU, mentioned in Sec. 3.2.1, I can calculate the mass cut-off value above which IDP impactors can not contribute significantly to the data set (less than one impact expected). This argument is particularly useful for the analysis of the *Cassini* data, where the total measurement period was relatively short.

Third, as discussed in Sec. 3.2.1, IDPs within the mass range considered in the data analysis are sensitive to the radiation pressure. The β ratio influences the orbital momentum and the orbital energy of an IDP. Thus, the impact velocity vectors of two interplanetary grains having the same orbital elements, but different β values, will be different, resulting in a different sensitivity of the instrument. As a consequence, the probability of detection of IDPs is also a function of their β ratio value. As the β ratio is a function of the particle mass only, the calculation of the sensitivity to IDP populations parameterized with the β value allows to further constrain the mass range where IDPs

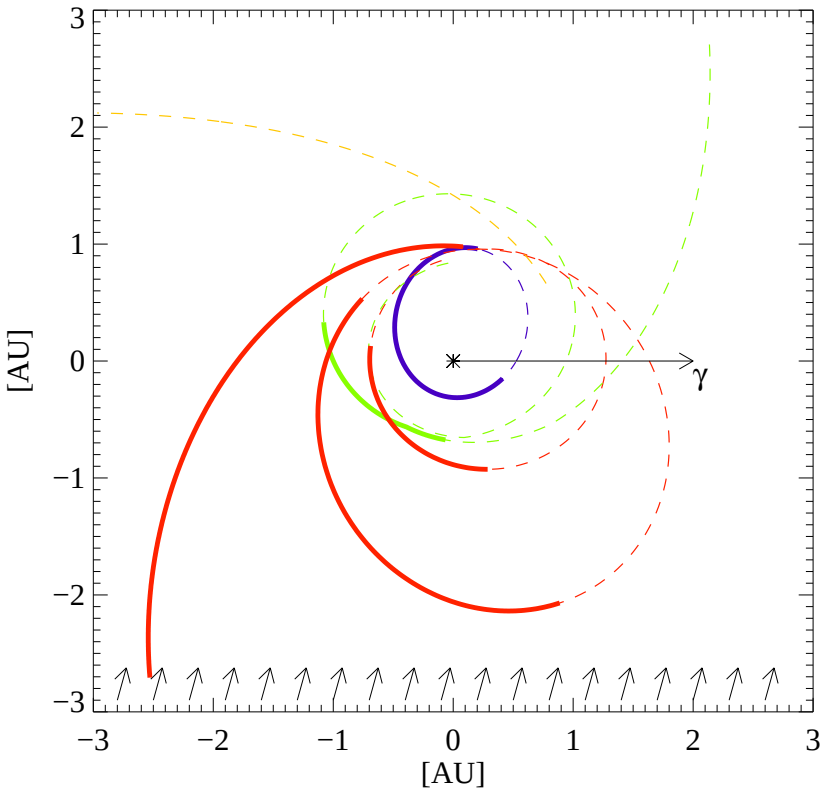

Figure 4.1: This plot shows the orbits of the different spacecrafts: the *Helios* trajectory is in blue, the *Galileo* trajectory in red, the *Cassini* trajectory in green, and the *Ulysses* trajectory in yellow. The X-axis is parallel to the vernal equinox direction. The direction of the ISD stream is given by the arrows. The thick lines give the orbit segments where ISD grains could be identified.

most likely contribute to our data set.

The trajectories within 3 AU of all the missions analysed in this work are shown in the heliocentric reference frame in Fig. 4.1. The ISD stream direction is indicated by the arrows. In the cases of the *Helios*, *Cassini*, and *Galileo* missions, the orbit configurations provided orbit segments where the velocity of the spacecraft relative to the ISD stream was high. (Note that the orbits were traversed in each case in the prograde direction.) Orbit segments plotted in thick lines, are favorable for the identification of ISD grains as discussed above. Furthermore, Fig. 4.1 shows that the *Ulysses* trajectory within 3 AU was not suitable for the identification of ISD as described above. Indeed, the trajectory of the spacecraft was almost perpendicular to the ISD stream direction, resulting in too low relative velocities. Nonetheless, the data obtained by *Ulysses* beyond 3 AU, above and below the ecliptic plane will be used in Sec. 4.5 to show an

interesting instrumental effect.

The data analysis of the *Cassini*, *Galileo*, *Helios* and *Ulysses* dust instrument follows. Note that the *Galileo*, *Helios* and *Ulysses* data have been already processed during the last decades, so that no additional work is needed before starting the data analysis. In particular, genuine dust impacts have been identified from noise events and the instrument behavior under different measurement conditions is known. In contrast, the higher complexity of the *Cassini* instrument and the more recent acquisition of the dust data required an extensive preliminary work on the data. A very brief summary of this work is provided in Appendix. B.

4.2 Analysis of the CASSINI data

In this part, I introduce shortly the *Cassini* mission, before I present the analysis of the data.

4.2.1 The CASSINI-HUYGENS mission

The Cassini-Huygens mission is an ambitious European-American exploration program of the Saturnian environment. The American spacecraft *Cassini* carries, in addition to many scientific instruments, the European lander Huygens, that will be released in the Titan atmosphere in January 2005. The Cosmic Dust Instrument (CDA), described in Sec. 2.2 is mounted on *Cassini* as shown on Fig. 4.2. The *Cassini* spacecraft was

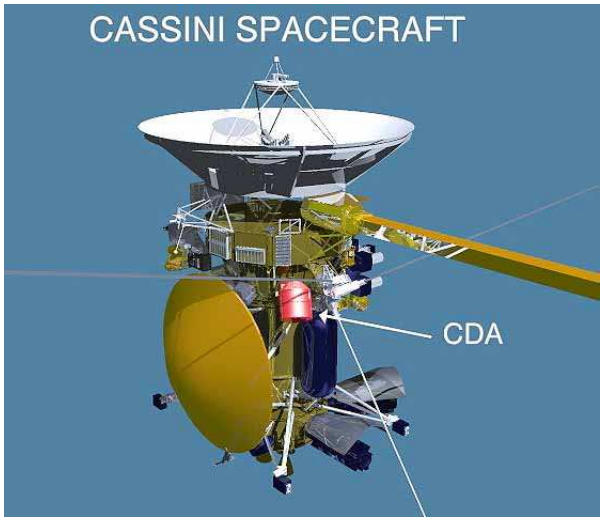

Figure 4.2: CASSINI spacecraft. To the left and on the right of the dust experiment (CDA) are mounted the Huygens probe and the plasma wave experiment. The diameter of the high gain antenna (on the top) is about 4 m.

launched in October 1997 and is now at about 1 AU from Saturn. During the first 2

years of *Cassini*'s cruise through the inner Solar System, the spacecraft performed two Venus flybys and one Earth flyby to obtain enough energy to reach Saturn's orbit, as can be seen on Fig. 4.3.

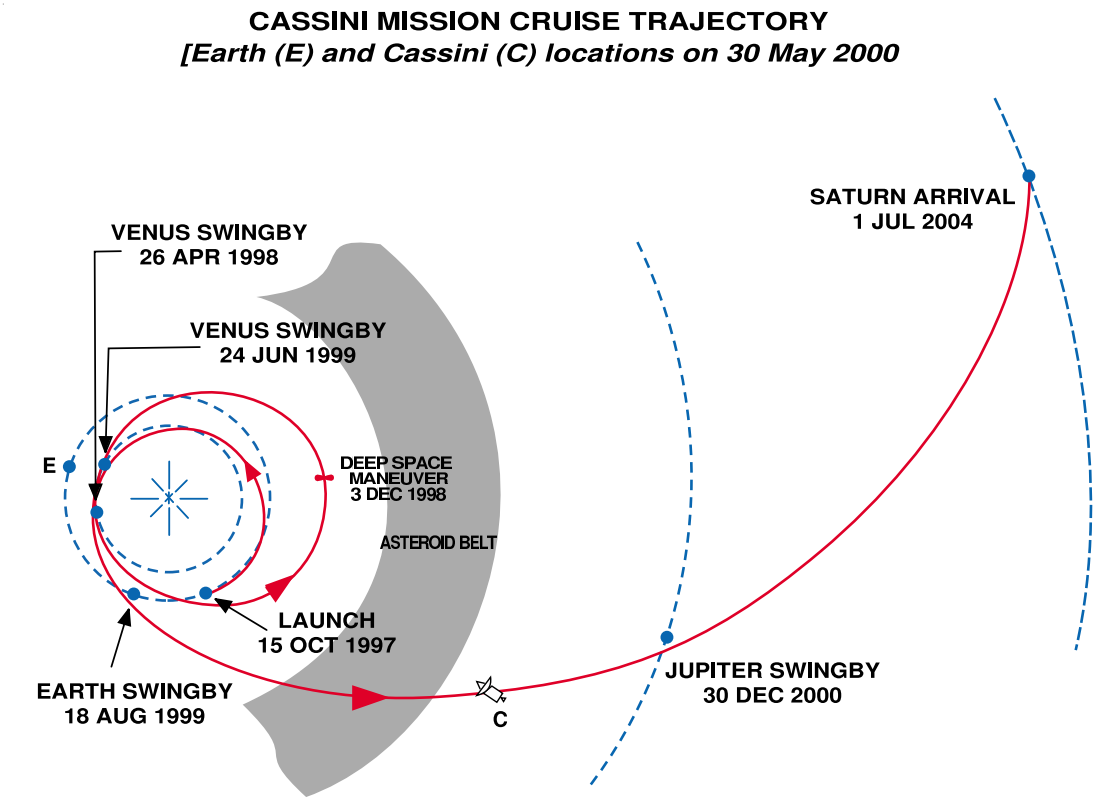

Figure 4.3: Trajectory of the *Cassini* spacecraft, from launch until its arrival at Saturn. Two fly-byes at Venus and one fly-by at Earth increase the orbital energy of the spacecraft. A last fly-by at Jupiter inserted *Cassini* on its trajectory to Saturn.

The first nominal measurements with the Cosmic Dust Analyzer (CDA) on *Cassini* were done between March and August 1999, corresponding to a heliocentric distance ranging from 1.2 to 0.7 AU. The work presented here is based on the data obtained during this period. Fig. 4.4 shows the spacecraft trajectory during this mission phase. Note that in this figure, the trajectory is plotted in the ISD dust frame. It means that the X-axis is parallel to the ISD direction.

Cassini is a three-axis stabilised spacecraft, and a desired instrument orientation has to be established by controlling the spacecraft attitude. In addition, the instrument orientation can be adjusted with a turn table the CDA is mounted upon. During the whole observation period, the dust instrument's boresight was as close as possible to the approach direction of the ISD flux (see Fig. 4.4). Moreover, the spacecraft was moving almost towards the interstellar dust direction, leading to a high velocity (about

55 kms^{-1}) relative to the interstellar stream, and consequently increasing the rate of interstellar impacts. In that sense, the spacecraft's flight configuration was optimized for the detection of ISD grains.

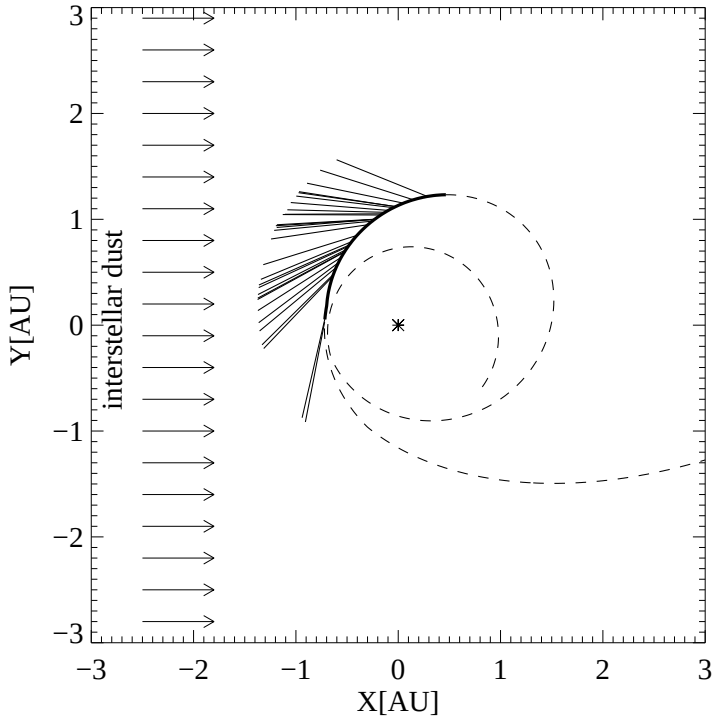

Figure 4.4: *Cassini*'s trajectory (broken curve) projected into a heliocentric ecliptical frame shown together with the orbits of Venus, Earth, and Mars (solid curves). The positive x-axis corresponds to the ISD flux downstream direction (arrows). The thickly drawn trajectory segment marks the period during which the data presented in this paper were taken. The instrument pointing (thick segments) is given for each event of the data set.

The results presented in this thesis rely on the data provided by the impact ionization detector (IID) subsystem of the *Cassini* dust instrument alone. The data provided by the other CDA subsystems (see Sec. 2.2) could not be used for this work. Indeed, the HRD detector is designed to monitor high impact rates in Saturn's rings environment. Furthermore, the data transmission rate during the presented period was low and did not allow an ideal data transmission for the CA and QP subsystems. The high density plasma wind close to the Sun would have saturated the charge grid device of the QP subsystem.

4.2.2 Dynamical Study

In this section I study the dynamical properties of the impactors likely to hit the detector during the period in question. This dynamical study is crucial to find criteria to reliably separate interstellar impactors from interplanetary ones.

As discussed in Sec. 3.2.2, the ISD grains are assumed to move on straight lines ($\beta \approx 1$), in the direction defined by the interstellar helium flow, with $v_d = 26$ kms^{-1} relative to an heliocentric inertial frame.

Since the *Cassini* spacecraft is flying in the ecliptic plane, the major difficulty is to identify the impacts as ISD or IDPs. The likelihood for an interplanetary particle to hit the detector depends strongly on its orbital elements. The orbits of interplanetary dust grains cover a wide range of orbital elements. However, the fact that Cassini is a three-axis stabilized spacecraft, the rather small field-of-view (45°) of CDA and a quasi fixed boresight pointing during the measurement period, strongly restrict the sensitivity of the dust detector to certain combinations of orbital elements. Therefore, the first step consists of calculating the CDA sensitivity to interplanetary impactors on bound orbits defined by their eccentricity, semi-major axis and inclination. In agreement with the simplified model of the IDP orbital elements described in Sec. 3.2.1, I consider the maximum value for the inclination to be 30°. As a consequence, interplanetary particles on retrograde orbits are excluded by this assumption. Another parameter, the β ratio, is added to the simulation. The β value implicitly sets restrictive conditions onto the mass of the impactors (Gustafson, 1994). Furthermore, the calculated theoretical impact velocity of interplanetary population and the impact charge threshold of CDA, also set a minimum mass cut-off. At least, the negative slope of the interplanetary dust mass density distribution allows to calculate a maximum mass cut-off, above which interplanetary impactors, statistically, may not contribute to our data sample significantly.

Interestingly, it turned out that interstellar grains and the most probable contribution of interplanetary particles are expected in comparable mass ranges. On the other hand, I show that the theoretical impact velocity difference between the interstellar and interplanetary populations is large enough to be able to distinguish between IDP and ISD impactors exclusively by their impact charge.

The CDA detector has an opening angle of about 45°. Thus, only particles entering the detector with impact angles $\mathbf{v}_{imp} \cdot \mathbf{b} \leq \cos 45^\circ$ can hit the target, where $\mathbf{b}$ is the CDA boresight vector at the spacecraft location $\mathbf{r}_{sc}$. The impact velocity vector $\mathbf{v}_{imp} = \mathbf{v}_d - \mathbf{v}_{sc}$ with $\mathbf{v}_d$ and $\mathbf{v}_{sc}$ being the heliocentric dust velocity vector and the spacecraft velocity, respectively. For particles on bound orbits around the Sun the heliocentric orbital velocity v_0 can take values between zero and the escape velocity $v_e = \sqrt{\frac{2\tilde{\mu}}{r_{sc}}}$. Since the particle's absolute angular momentum h is fixed uniquely by $\mathbf{v}_d$ and $\mathbf{r}_{sc}$, the orbit's semi-major axis a and eccentricity e are related to each other by $h = v_0 r_{sc} |\sin\alpha| = \sqrt{\tilde{\mu} a (1-e^2)}$, with α being the angle between $\mathbf{v}_d$ and $\mathbf{r}_{sc}$. From the

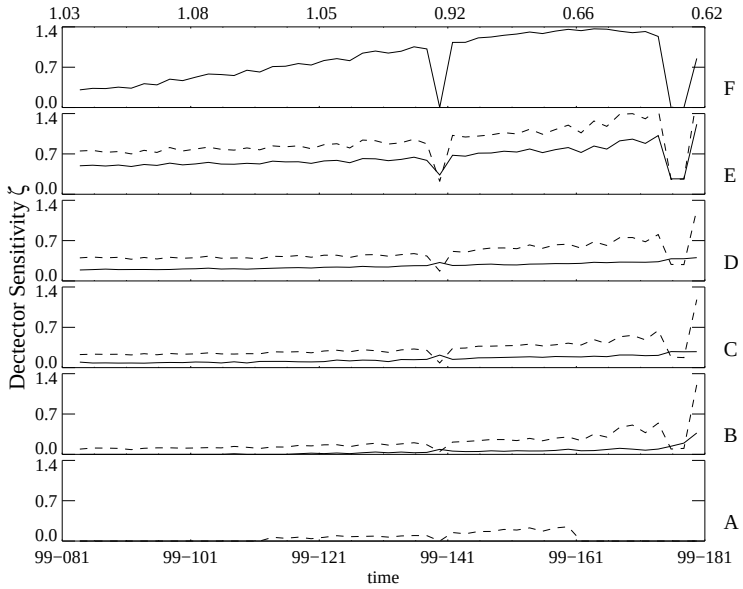

Figure 4.5: Sensitivity ζ of the CDA as a function of time between day 081 and day 181. The uppermost panel (F) gives ζ for interstellar particles with $\beta = 1$. The other panels show IDPs with: (A): $0 \leq e < 0.2$, (B): $0.2 \leq e < 0.4$, (C): $0.4 \leq e < 0.6$, (D): $0.6 \leq e < 0.8$, (E): $0.8 \leq e \leq 1$. Solid curves correspond to $\beta = 0.3$, while broken curves correspond to $\beta = 0.8$. The upper scale indicates the distance to the Sun in AU. The features on day 138 and 175 were caused by spacecraft attitude changes to perform a trajectory correction maneuver and the second Venus flyby, respectively.

conservation of the orbital energy per unit mass follows that the eccentricity depends only on the orbital velocity

$$\tilde{\mu}^2(1-e^2) = \sin^2\alpha v_0^2 r_{sc}(\tilde{\mu}^2 - v_0^2 r_{sc}). \tag{4.1}$$

From the conservation of the angular momentum further follows that the orbit inclination of the impacting particle is given by

$$\cos i = h^{-1}(\mathbf{r}_{sc} \times \mathbf{v}_d) \cdot \mathbf{z}, \tag{4.2}$$

where $\mathbf{z}$ is a unit vector pointing in the ecliptic north direction. Through this set of equations it becomes evident that each valid impact vector $\mathbf{v}_{imp}$ uniquely corresponds to a bound orbit (a,e,i). To determine the orbital parameters of the possible impactors at $\mathbf{r}_{sc}$, I calculated (a_i,e_i,i_i) for a comprehensive set of compatible impact vectors $\{\mathbf{v}_{imp}\}$. Next, I pooled impact vectors with similar eccentricities to subsets and, finally, calculated for each subset its mean impact angle θ onto the target and its mean impact velocity $\mathbf{v}_{imp}$. I define the sensitive area $A(\theta)$ of the instrument as the target area that can be hit by particles entering the detector with an impact angle θ. Furthermore, the definition of the effective sensitive area,

$$A(\mathbf{v}_{imp},\theta) = |\frac{\mathbf{v}_{imp}}{\mathbf{v}_d}|A(\theta), \tag{4.3}$$

takes into account the motion of the target relative to a subset of impactors. Let us now normalize the effective sensitive area to its value $A_0 = 0.1$ m^2 corresponding to the effective sensitive area exposed to a focused beam of particles impacting the CDA's target with $\theta = 0^\circ$, if the latter were at rest in the heliocentric frame. Hence, the factor $\zeta = \frac{A(\mathbf{v}_{imp},\theta)}{A_0}$, function of the time and the subset of impactors considered, allows one to estimate the sensitivity of the detector to different dust populations during the spacecraft's interplanetary journey.

	eccentricity	$\langle v_{imp} \rangle$ [kms^{-1}]		max(v_{imp}) [kms^{-1}]		$\langle m_{thres} \rangle$ [kg]	
	β	0.3	0.8	0.3	0.8	0.3	0.8
A	0.0...0.2	-	10	-	11	-	$4.1 \cdot 10^{-16}$
B	0.2...0.4	10	21	13	24	$4.0 \cdot 10^{-16}$	$3.7 \cdot 10^{-18}$
C	0.4...0.6	15	22	25	28	$5.2 \cdot 10^{-17}$	$7.7 \cdot 10^{-18}$
D	0.6...0.8	20	24	36	33	$1.2 \cdot 10^{-17}$	$5.1 \cdot 10^{-18}$
E	0.8...1.0	24	25	38	35	$5.1 \cdot 10^{-18}$	$4.0 \cdot 10^{-18}$

Table 4.1: Impact velocity v_{imp} and mass detection threshold m_{thres} for IDP impacts on CDA between 1999-081 and 1999-181 given for distinct eccentricity intervals and two β values. The threshold masses were calculated using Eq. 2.2 with a charge detection threshold of 10^{-14} C.

The result of the calculations is shown in Fig. 4.5. For IDP's, the sensitivity is indicated for distinct eccentricity ranges and for two β values. Obviously, the detector is geometrically much more sensitive to IDPs moving on highly eccentric orbits ($e \geq 0.8$) than to IDPs with low eccentricities. This finding affects in particular the probability to detect bigger particles since they were found to move mostly on low eccentric orbits (Staubach et al., 2001). To derive a statistical upper mass detection limit I calculated for what lower mass cut-off the accumulated number of impacts becomes less than one. I assumed that the flux between Earth and Venus can be approximated by the interplanetary flux model at 1 AU (Grün et al., 1985). The total expected number of interplanetary particles heavier than 10^{-14} kg during the observation time is less than one. Hence, I conclude that interplanetary particles with mass values above 10^{-14} kg are not likely to contribute to our data sample.

Important conclusions about the mass detection threshold can be drawn from the derived theoretical impact speeds given in Tab. 4.1. To initiate a measurement, an impacting particle has to produce sufficient charges to exceed the trigger threshold of 10^{-14} C. As can be seen from Tab. 4.1, the detector was insensitive to IDPs with $m_d < 5 \cdot 10^{-18}$ kg. We are confident that our study provides enough evidence to conclude that the recorded data set can only include IDPs with masses between $5 \cdot 10^{-18}$ and 10^{-14} kg. Moreover, due to the negative slope of the IDP mass distribution, impacts by IDPs with small masses are much more likely. Thus, the majority of interplanetary impactors

will have masses smaller than 10^{-15} kg. Taking the higher sensitivity to particles with $\beta \sim 0.8$ (Fig. 4.5) into account helps to constrain the distribution of the detectable IDPs even further. Grains between 10^{-17} kg and 10^{-15} kg are characterized by $\beta \gtrsim 0.8$ with a maximum in β around 10^{-16} kg, (Gustafson, 1994). Thus, the expected IDP flux will also show a pronounced maximum around 10^{-16} kg.

Throughout the whole observation period, the instrument was also sensitive to ISD impacts in the mass range mentioned above. Thus, the data set will be dominated by impacts of both IDPs and ISD grains of comparable masses but of different impact speeds. For ISD, impact speeds are expected to be narrowly distributed around 55 kms^{-1}, while for IDPs with high eccentric orbits our study predicts mean impact speed values around 25 kms^{-1} (see Tab. 4.1). As a consequence, the impact speed difference of 30 kms^{-1}, corresponding to an impact charge difference of 2 orders of magnitude, see Eq. 2.2, allows us to identify interplanetary candidates among the impacts that generated the smaller impact charge. Using Eq. 2.2 for the mean mass value expected for IDPs (10^{-16} kg) and their mean impact velocity value (25 kms^{-1}), an upper impact charge limit value for interplanetary grains around ($< 3 \cdot 10^{-12}$ C) is derived. As a consequence, a statistically significant number of impactors in the upper impact charge range will give strong indications for the presence of an interstellar contribution in our data sample. In addition, as the theoretical mass and impact velocity values for interplanetary impactors are within the instrument's calibration range, the comparison between the measured impact velocity values with the theoretical expectations provides a second identification scheme for interplanetary impactors.

4.2.3 Analysis of the CASSINI dust data

In this section I analyze the impact data taken between 0.7 and 1.2 AU distance from the Sun in 1999. During this period, the CDA detector recorded and transmitted 121 events to Earth. All transmitted event data sets included the charge signal curves QT, QC, and QI and the multiplier waveform MP (see Sec. 2.2). The analysis of the original charge signals on Earth enabled us to identify noise events. Due to charge balance in an impact plasma, genuine impact events have to show both an ion signal (QI) and, at least, one electron signal (QT or QC). Furthermore, the detector geometry requires that one of the target signals QT and QC started to rise earlier than the ion grid signal QI. Applying these criteria reduced the data set to 29 events, which were most likely caused by genuine dust impacts. For a detailed description of the dust impact identification scheme, please see Appendix. B.

As discussed in the previous section, the QI charge amplitude of interstellar impactors is expected to be about two orders of magnitude larger than the QI amplitude caused by interplanetary grains. The values of the QI charge signals are plotted in Fig. 4.6, together with the impact date and the corresponding distance to the Sun. To identify the interplanetary impactors I considered all impacts with charge amplitudes between 10^{-14} C and $\sim 3 \cdot 10^{-12}$ C as possible IDP candidates. To prove that the

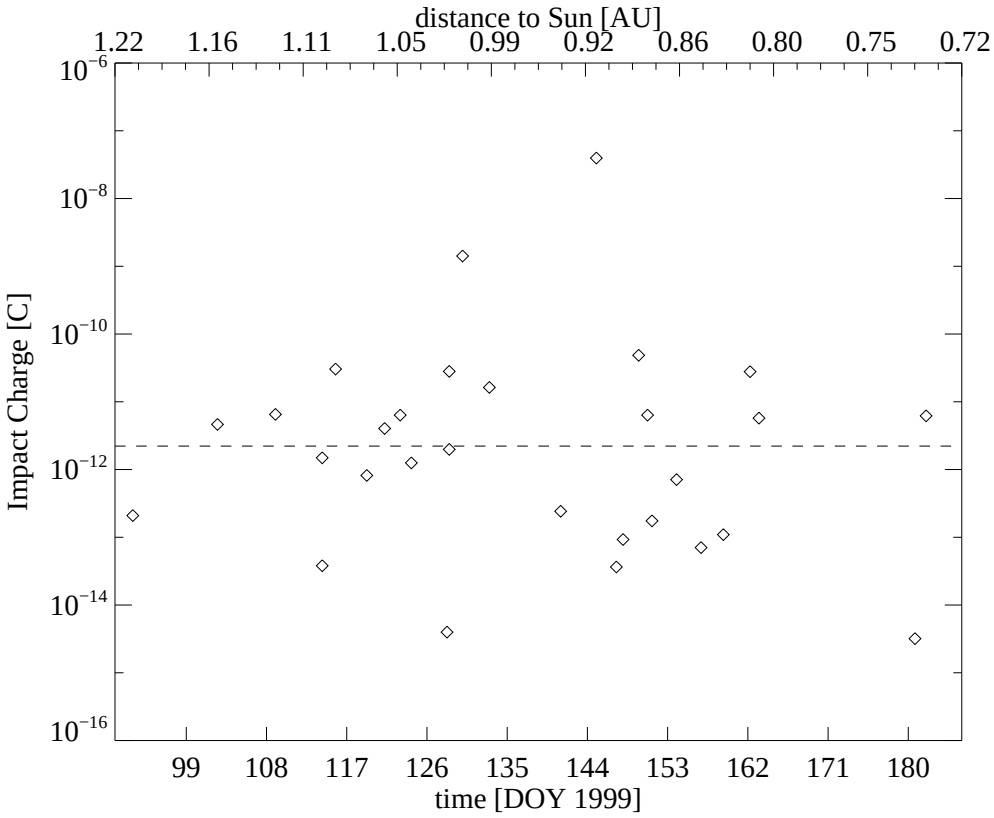

Figure 4.6: Impact charge value for each impact of our data sample, as function of the time. The broken line shows the limit value of the impact charge ($3{\cdot}10^{-12}$ C), above which the interplanetary impactors should not contribute signifi cantly to the data set. Thus, the particles in the low impact charge region should be mostly populated by dust grains of interplanetary origin, while the high impact charge region corresponds to an interstellar contribution. From this plot, I estimate the number of interstellar grain candidates to be around 14 ± 3.

resulting subset actually comprises mostly IDPs I plotted in Fig. 4.7 their impact velocity, measured with the rise time method, as function of the time, together with the theoretical predictions for interplanetary particles moving on high eccentric orbits and with $\beta = 0.8$. Due to the high sensitivity of the detector for such grains (see previous section), I expect the major interplanetary contribution to be provided by these grains. Note that the theoretically expected masses and impact speeds of those IDPs are within the calibration range. Thus, for these impacts, the rise time method should be applied to derive the impact velocity v_{imp} from the ion impact charge signal rise time t_r For impacts on the IID it was found by calibration tests with the CDA flight spare unit that

$$v_{imp} = 1.74 \cdot 10^{-3} t_r^{0.85}, \tag{4.4}$$

where the result is accurate to a factor of two, (Srama, 2000a; Stübig, 2002). Obviously,

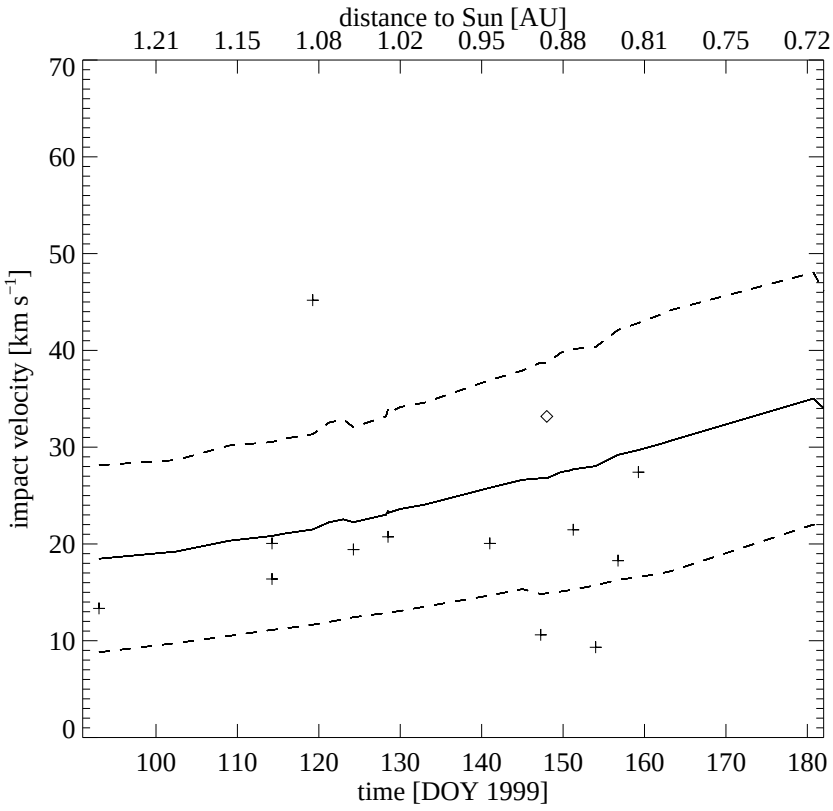

Figure 4.7: Impact speed as function of time plotted for all impacts with QI charge amplitudes between 10^{-14} C and $3 \cdot 10^{-12}$ C. Crosses denote impacts on the outer target (IID). One event marked by a diamond has been identified as an impact onto the inner target (CAT) accompanied by a time-of-flight mass spectrum. The broken curves indicate the minimum and maximum impact speeds theoretically expected for IDPs with $\beta = 0.8$ and moving on high eccentric orbits, while the solid curve signifies the mean speed of such particles. The upper scale gives the distance to the Sun in AU.

for 10 of these impacts, the derived impact speeds are consistent with the theoretical expectations. Furthermore, the measured mean mass of $1.6 \cdot 10^{-16}$ kg agrees well with the characteristic masses of grains with large β values, (Gustafson, 1994), and, thus, also with our theoretical expectations in Sec. 4.2.2. The three impactors outside the theoretical predictions may belong to other interplanetary populations less likely to be detected.

Next, let us identify the origin of the 14 ± 3 residual particles in the data set. In Sec. 4.2.2, I showed that the interplanetary contribution is essentially represented by grains on high prograde eccentric orbits and mass values concentrated around 10^{-16} kg. By their theoretical mean impact velocity of 25 kms^{-1}, those grains cannot account for a statistically significant number of impacts with charge above $3 \cdot 10^{-12}$ C. In spite of this, the impacts with big impact charge value (greater than $3 \cdot 10^{-12}$ C) comprise

more than half of our data sample.

Hence, the residual data set can only include interstellar grains or IDPs moving on hyperbolic orbits, i.e. β-meteoroids (interplanetary grains for which $\beta > 1$). The latter candidates were highly unlikely to be observable due to inappropriate instrument pointing. Thus, it is justified to consider these events to be most likely caused by ISD grains. This conclusion is supported by the impact charge of these events. Indeed, the QI amplitudes range between $3 \cdot 10^{-12}$ C and 10^{-10} C, which is in good agreement with Eq. 2.2 and the theoretical expectations on the mass value and the impact velocity given in Sec. 4.2.2. Apparently the rise time method failed to provide meaningful estimates for the ISD since the mean speed derived by this method was found to be only about 22 kms^{-1}. This contradicting result is not surprising. As explained in Appendix A, secondary ejecta created during the impact of big and fast impactors, like our interstellar dust grains, leads to an underestimation of the impact velocity by our instrument. However, using Eq. 2.2 to calculate m_d under the assumption that $v_{imp} \sim 55$ kms^{-1}, leads to reasonable ISD masses between $5 \cdot 10^{-17}$ kg and 10^{-15} kg. Furthermore, a number of 14 ± 3 ISD impacts during the observation period corresponds to a flux of $2.5 \pm 0.5 \cdot 10^{-5}$ m^{-2} s^{-1} comparable with the measurements by *Ulysses* at 3.5 AU during the same time period (Landgraf et al., 2003) .

4.2.4 Preliminary conclusions

For the first time ever, in-situ evidence of ISD at and inside the Earth orbit have been found, showing the deep penetration of the ISD stream into the inner Solar System. Furthermore, the analysis confirmed that the mass range of the detected ISD grains corresponds to bigger grain sizes in the ISM than expected from the MRN distribution (see Sec. 3.2.2). This result supports the conclusions of the *Ulysses* interstellar dust data analysis (Landgraf et al., 2000).

Furthermore, the ISD flux measured by *Cassini* around 1 AU is somewhat lower than the flux measured by *Ulysses* beyond 3 AU. This result is in qualitative agreement with the filtering process through radiation pressure mentioned in Sec. 3.2.2. Unfortunetly, the short measurement time results in a low statistics for ISD impactors and does not allow a precise quantitative estimation of this process.

However, the *Cassini* data show that the in-situ detection and the analysis of ISD within the ecliptic plane and at Earth distance is possible. Therefore, this motivates a reanalysis for ISD grains of the dust data obtained by previous spacecrafts in the inner solar system. Although opportunities to monitor the ISD stream from 0.3 AU to 2.5 AU were provided by the *Galileo* and *Helios* missions, none of the previous data analysis tried to estimate the ISD contribution to the respective data sample. Therefore, the dust data obtained by these two missions are reanalysed in Sec. 4.3 and Sec. 4.4 for ISD grains.

4.3 Analysis of the GALILEO data

Data taken with *Galileo* between 1990-001 and 1992-365 within 3 AU has not been examined yet for ISD. However, the *Cassini* findings encouraged me to analyse the *Galileo* data for such grains as well. This section is organized as follow. In the first part I briefly describe the *Galileo* mission, the spacecraft, and its trajectory during its interplanetary cruise in the inner solar system. Then, I present the data set used for the analysis. A detailed description of the method to identify ISD grains within the *Galileo* data sample will be outlined in Sec. 4.3.3. This method is then applied to the data set and followed by an attempt to perform a 'β-spectroscopy' in Sec. 4.3.4. A discussion of the results can be found in Sec. 4.3.6.

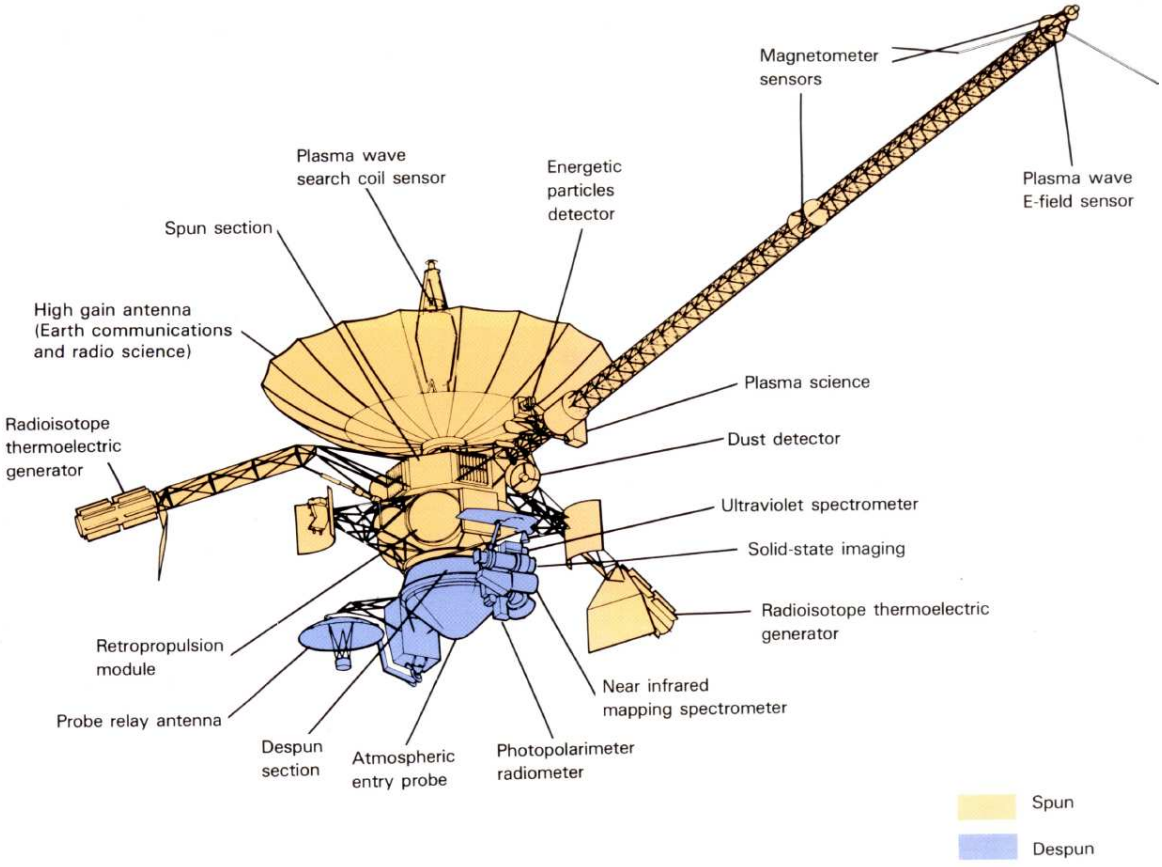

Figure 4.8: *Galileo* spacecraft. It consisted of a 3-axis stabilised de-spun section (in blue) and a spinning section (in yellow), whose spin axis is coincident with the antenna axis. The dust instrument is mounted on the spinning section, below the magnetometer boom. The atmospheric entry probe, released in the Jupiter atmosphere, was mounted on the despun section. The *Galileo* orbiter was the only dual-spin spacecraft ever flown.

4.3.1 Spacecraft's trajectory and geometry

Between January 1990 and mid 1993, the *Galileo* spacecraft traversed the interplanetary space within the Venus and the Mars orbits, performed flybys on the Earth, Venus, and the asteroid Gaspra, to gain enough energy to reach Jupiter. The dust instrument had been operated most of the time. I selected three orbit sections out of the interplanetary flight of *Galileo* between 0.7 AU and 3 AU, that provide favorable observation conditions for the interstellar dust stream. To identify ISD amongst the interplanetary dust background, the observation geometry has to fulfill two conditions. First, the ISD stream must be within the instrument field of view. Second, the impact velocity must be sufficiently high to allow to apply an identification method solely based on impact charge criteria. Fig. 4.9 shows the three orbit segments selected for the ISD detection.

For the two innermost orbit segments, the velocity of interstellar impactors relative to the spacecraft was about 50 kms^{-1}. In case of segment 3, the relative velocity ranged between 60 kms^{-1} (after the Earth flyby) and 35 kms^{-1} (at 1994-001). For heliocentric distances larger than 2.5 AU, ISD impacts can also be identified solely by directional arguments (Baguhl et al., 1995).

Galileo is a spinning spacecraft (see Fig. 4.8) with the antenna axis oriented antiparallel to the positive spin axis. From launch till January 1993 the antenna pointed to the Sun. Afterwards, the antenna was oriented to the Earth. The angle between the instrument boresight and the positive antenna axis is 60° and the instrument field of view is of 140°. Per spacecraft rotation the instrument boresight $\mathbf{p}$ cross two times the ecliptic plane. $\mathbf{p}$ can be characterised by a single parameter, the so-called rotation angle ϕ, given as the angle between two planes: the plane spanned by the rotation axis $\mathbf{s}$ and the ecliptic north direction $\mathbf{N_e}$ and the plane spanned by the boresight and the rotation axis. For $\phi = 0^\circ$, the instrument boresight $\mathbf{p}(0) = \mathbf{p}_0$ is defined by:

$$\frac{\mathbf{s} \times \mathbf{N_e}}{|\mathbf{s} \times \mathbf{N_e}|} \cdot \frac{\mathbf{s} \times \mathbf{p_0}}{|\mathbf{s} \times \mathbf{p_0}|} = 1 \tag{4.5}$$

This definition implies that for $\phi = 90^\circ$ the boresight is within the ecliptic plane, oriented toward the spacecraft apex direction (see Fig. 4.9).

4.3.2 Data sample

The discrimination between genuine dust impacts and noise events has been performed by Baguhl (1993). Between 1989-365 and 1993-365, the *Galileo* dust detector registered 517 genuine dust impacts. Fig. 4.10 shows the rate of the impacts detected by the *Galileo* dust instrument. The flybys are also indicated. Time periods without data transmission appear clearly.

The transmitted set of impact parameters depends on the telemetry capabilities. Here, I only considered periods during which all relevant parameters required for the analysis

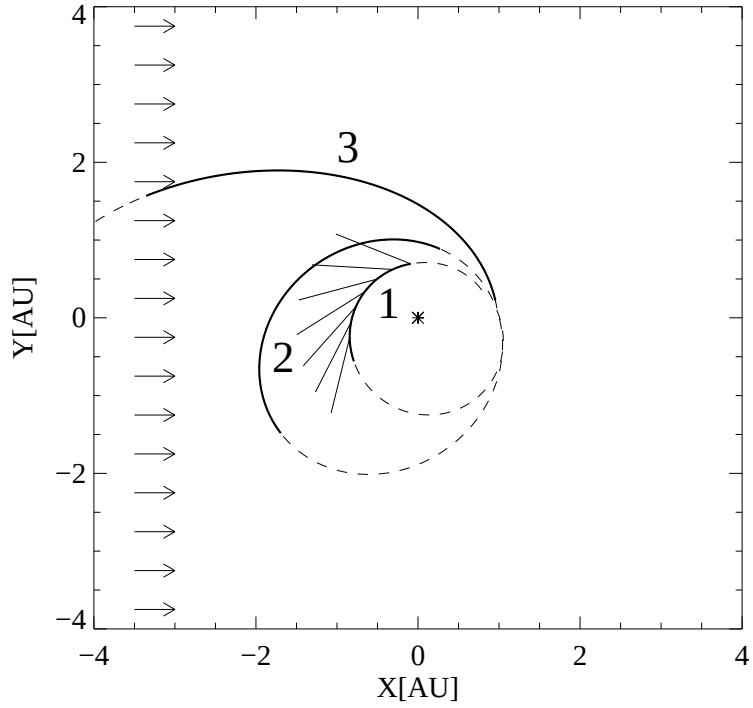

Figure 4.9: Galileo's trajectory projected in the ecliptic plane from launch in december 1989 until 1994. The X-axis has been chosen parallel to the interstellar dust stream indicated by the arrows. The full lines represent the 3 orbit segments used for the analysis. The thin lines attached to segment 1 are indicating the instrument pointing within the ecliptic plane ($\phi = 90°$).

were transmitted. These include the impact time, the ion impact charge, and the rotation angle. Fig. 4.11 depicts the resulting data sample consisting of 435 impact events. The impact time is given together with the rotation angle at the impact time. The amplitude of the impact charge signal is indicated by circles, whose surfaces are proportional to the logarithm of the signal amplitude. Furthermore, the sensitive area with respect to impacts by ISD with $\beta = 1$ is plotted as contour lines.

The sensitive area $A(\phi,t)$ of the instrument is defined as the target area exposed to particles entering the detector. The sensitive area is obviously a function of the time t and of the rotation angle ϕ. To take into account the relative motion of the spacecraft relative to the ISD stream, I define the effective sensitive area as the detector area required to register the same impact rate in the heliocentric inertial frame. Thus, v_{imp} and v_d being the impact velocity of ISD impactors and their velocity in the heliocentric frame, respectively, the effective sensitive area is

$$A_{eff}(\mathbf{v}_{imp},\phi,t) = |\frac{\mathbf{v}_{imp}}{\mathbf{v}_d}|A(\phi,t). \tag{4.6}$$

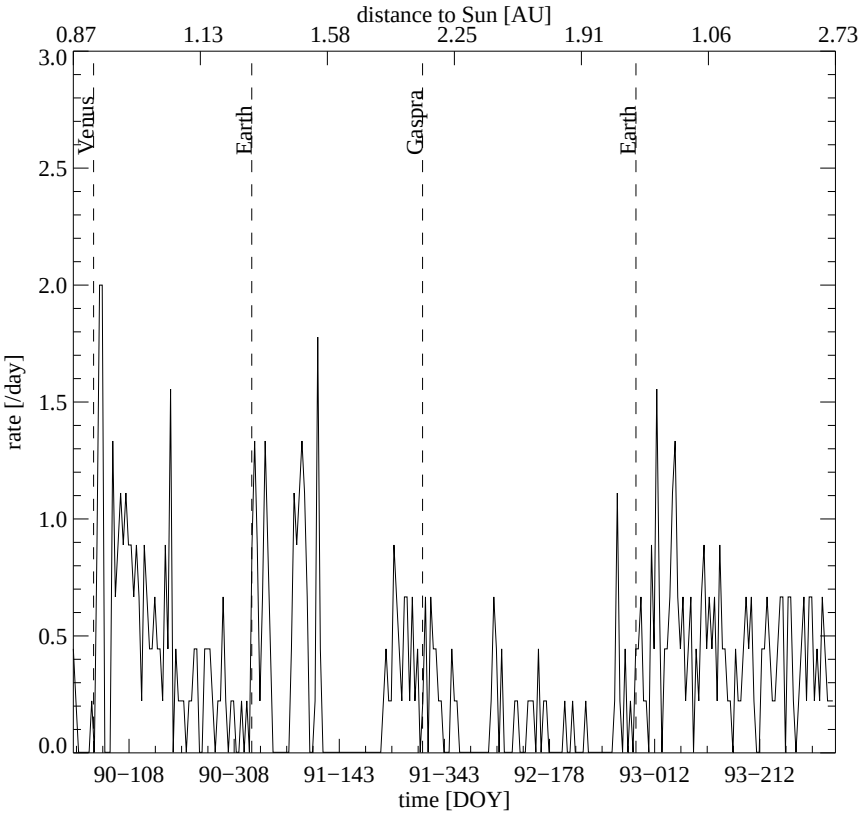

Figure 4.10: Rate of impacts detected by the *Galileo* dust instrument from 1990 to end 1993. A sliding average over 5 days has been used. The heliocentric distance is given by the upper scale. The dashed lines indicate the different flybys performed by the spacecraft.

As a consequence, the sensitivity for ISD impactors will be high for a pointing direction offering the largest target area to the impactors, combined with a high impact velocity. As can be seen from Fig.4.11, the conditions for detecting ISD grains started to be favorable after the planetary flybys. The Gaspra flyby occurred during orbit 2 and did not influence much the detection geometry for ISD grains. Unfortunately, the spacecraft went two times in safe mode between 1991-123 and the Gaspra flyby (segment 2), resulting in a data gap of about 100 days.

As can be seen in Fig.4.11, the impacts cluster within three distinct $\{\phi,t\}$ regions for which A_{eff} does not vanish. In each of those regions, A_{eff} takes a local maximum. For the analysis, I constrained our data sample to values of ϕ and t for which A_{eff} is greater than 10% of its local maximum. As can be seen from Fig. 4.11, this corresponds to impactors subsets for which $\phi \approx 90^\circ \pm 50^\circ$.

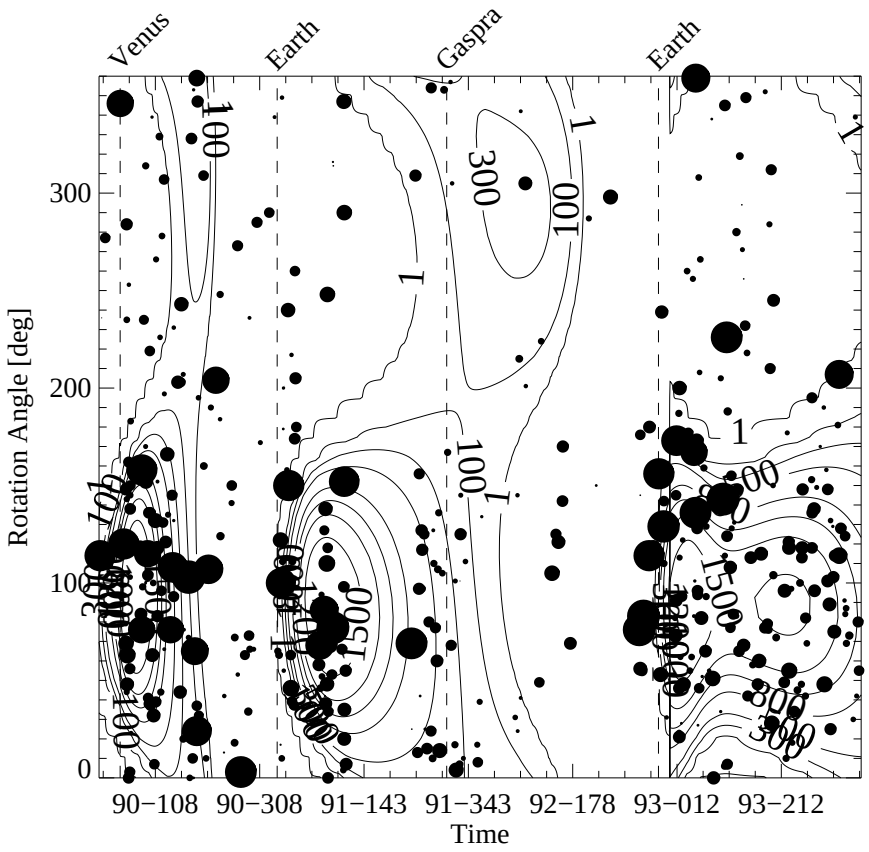

Figure 4.11: Dust impacts from 1989-001 to 1993-120, for which a full set of impact parameters including the rotation angle was transmitted to the Earth. The surfaces of the circles are proportional to the logarithm of the impact charge. The contour lines represent the effective sensitivity (in cm^2) to the ISD flux. The vertical broken lines indicate the flybys of the spacecraft at Venus, Earth and Gaspra.

4.3.3 Impactors identification

During *Galileo* interplanetary cruise, its trajectory was lying within the ecliptic plane. Besides of ISD grains, various interplanetary populations were also likely to hit the dust detector. For the data analysis, a simple model providing a coarse description of the IDP flux onto *Galileo* is sufficient. Thus, I employed the model by Staubach (2001) which is primarily based on in-situ data, and assumed the validity of the hypothesis on the population of IDPs made in Sec. 3.2.1.

The basic idea of the employed method to discriminate ISD from IDPs is to constrain for each impactor its most probable origin based upon the instrument pointing at the impact time and the ion charge yield *QI*. In particular, the likelihood of the measured *QI* value is estimated under the assumption that each impactor is of interplanetary origin.

The spacecraft location and the instrument boresight constrain the range of compatible values of semi-major axis, eccentricity, and inclination $\{a,e,i\}$ of detectable IDPs on bound orbits. Given are the position $\mathbf{r}$ and the velocity $\mathbf{v_{sp}}$ of the spacecraft at the impact time. The effective sensitive area A_{eff}, defined in Sec. 4.3.2, is a function of the subset $\{a,e,i\}$. As the calculation of A_{eff} takes into account the motion of the spacecraft relative to the impactors, A_{eff} is also a function of the β-ratio value. Indeed, the angular momentum associated to the values a and e is given by $\mathbf{h} = \mathbf{r} \times \mathbf{v_d} = \sqrt{\tilde{\mu} a(1-e^2)}\frac{\mathbf{h}}{|\mathbf{h}|}$. Thus, h is a decreasing function of β. Therefore, grains at the same heliocentric location but with different β will have different heliocentric velocity. The grain with the higher β will be the slowest.

For given values of i and β, I calculated the possible impact velocity vectors. As *Galileo*'s trajectory is lying within the ecliptic plane, a dust grain is detected at its ascending or descending node. I introduce the local coordinate frame $(\mathbf{u_r}, \mathbf{u_\theta}, \mathbf{u_z})$ attached to the spacecraft, with $\mathbf{u_r} = \frac{\mathbf{r}}{|\mathbf{r}|}$ and $\mathbf{u_z}$ is the ecliptic north. Thus, $\mathbf{u_\theta}$ points toward the spacecraft's apex direction. The dust velocity is given by its coordinates in the local frame, v_{dr},$v_{d\theta}$,v_{dz}. The angular momentum of the grain can be expressed in the local coordinate frame as: $\mathbf{h} = h(-\sin i u_\theta + \cos i u_z) = -r v_{dz}\mathbf{u_\theta} + r v_{d\theta}\mathbf{u_z}$. One finds that

$$v_{d\theta}^2 = \cos^2 i \frac{\tilde{\mu}}{ax^2}(1-e^2) \tag{4.7}$$

$$v_{dz}^2 = \sin^2 i \frac{\tilde{\mu}}{ax^2}(1-e^2), \tag{4.8}$$

with $x = r/a$. As the energy conservation imposes $v_d^2 = 2\tilde{\mu}(\frac{1}{r} - \frac{1}{2a})$, one finally yields

$$v_{dr}^2 = -\frac{\tilde{\mu}}{ax^2}(x^2 - 2x + (1-e^2)) \tag{4.9}$$

Eq. 4.9 implies the condition $1-e \leq x \leq 1+e$. Furthermore, Eq. 4.7-4.9 also prove that 8 different velocity vectors are theoretically possible. I systematically rejected the combinations for which $v_{d\theta} < 0$, corresponding to retrograde particles, in agreement with our assumptions. Thus, I considered only the 4 possible impact velocity vectors corresponding with prograde grains. The expression of the velocity vectors are parameterized by (x,e,β). For those 4 vectors, the effective sensitive area A_{eff} is calculated.

The β value which maximizes $A_{eff}(x,e,\beta)$ gives the most probable mass of an IDP within (x,e). For each impactor, the map of the effective sensitive area is calculated as function of (x,e). One example is shown in Fig. 4.13, left plot. In general, the 'prediction map' revealed that the dust instrument was sensitive to IDPs on high eccentric orbits, and close to their aphelion. Furthermore, it was found that high β values maximize the probability of detection. This qualitative result is in agreement with the expectations and can be explained as follows.

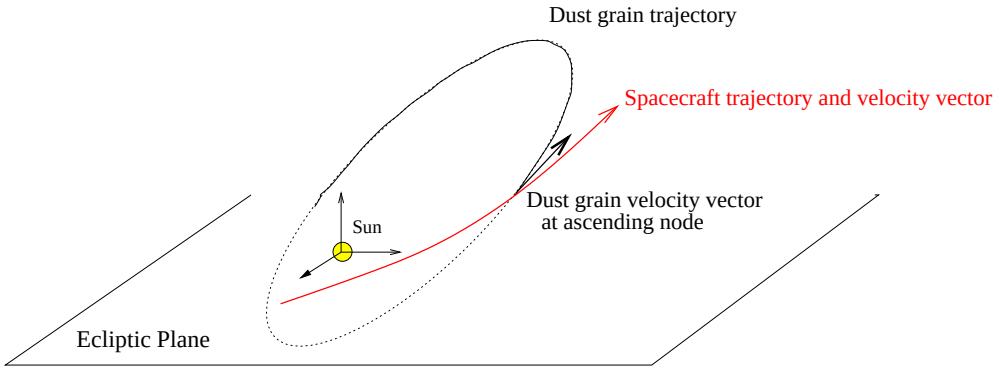

Figure 4.12: Schematic view of the IDPs detection by the *Galileo* spacecraft. IDPs are moving in the prograde direction and detected by the spacecraft at their ascending node. The velocity value of the dust grain depends both on the semi-major axis a and the β-ratio values. The heliocentric velocity of impactors coming from the spacecraft apex direction is smaller than the spacecraft velocity.

As the selected data set takes into account only particles coming from the spacecraft apex direction, the spacecraft moves faster than the particles and catches them up, see Fig. 4.12. Thus, the slower a dust grain, the higher the impact velocity. Assume now an IDP on a high eccentric orbit. Its velocity value is minimum at the aphelion. The higher the β ratio, the lower the angular momentum of the grain, and thus, the lower the velocity at the aphelion. Therefore the impact velocity is higher for such grains and the effective sensitive area as well. As a consequence, the detection probability is higher. Of course, the question arises to know if such IDPs really exist. Interestingly, a high eccentric prograde population with low inclination has already been identified from in-situ measurements and called the B population, (Staubach et al., 2001). Particles that belong to this population have a mass peak distribution about 10^{-16} kg, corresponding to high β values. Hence, I am confident that this population provides the dominant IDP contribution to our data sample.

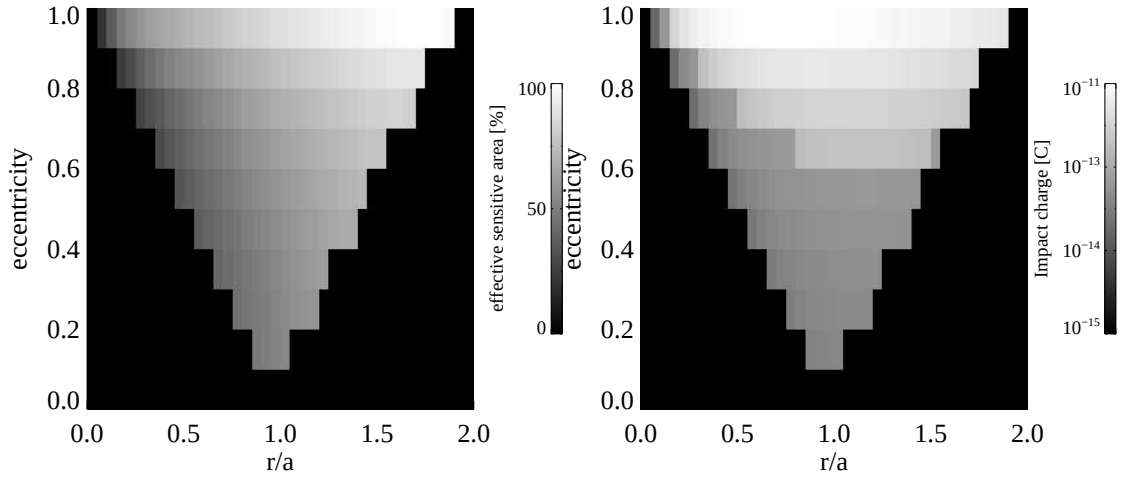

Figure 4.13: Coulor-coded plots of the effective sensitive area (left) and mean impact charge (right) calculated as function of the reduced semi-major axis x and the eccentricity for i=0°. The distance to the Sun was 0.74 AU and the rotation angle value ϕ= 84°. In this case, the expectation value of the impact charge is $1.3 \cdot 10^{-12}$C and $\sigma \approx 6.5 \cdot 10^{-13}$ C. The measured impact charge was $9.6 \cdot 10^{-12}$ C.

Note that I approximated the mass flux distribution between Venus and Mars by the interplanetary flux model at 1 AU (Grün et al., 1985). Due to the negative slope of the IDP spatial mass distribution, the data sample is statistically dominated by smaller particles. In addition, the lower mass detection threshold is constrained by the lower charge threshold of 10^{-14}C.

Using the calibration equation for the *Galileo* dust detector Eq. 2.2, $A_{eff}(x,e)$ associated to the most probable impactors mass range, the mean impact velocity and the spatial mass density distribution model at 1 AU, I finally calculate a theoretical impact charge value for each triplet (a,e,i) with a statistical weight. Calculations showed that A_{eff} is only weakly dependent upon small inclinations. An example of the impact charge as function of the (x,e) values is shown in the right plot of Fig. 4.15. Next, the expectation value for the impact charge and the corresponding 3-σ upper limit are calculated for each impact of the data sample.

As the typical mass value for ISD grains of the main ISD stream component is known, (see Sec. 4.5.1), and as the impact velocity of ISD grains can be derived from Eq. 3.8, I also calculated the theoretical impact charge range generated by ISD grains. The choice of the orbit segments for the data analysis leads ISD to have high impact velocity values and thus to generate high impact charges. As a consequence, the criterion to discriminate IDPs from ISD grains can be summarized as follows: if the measured impact charge is greater than the predicted probable upper limit value in case of an interplanetary origin, the impactor will be assumed to be from interstellar origin.

Fig. 4.14 shows the measured impact charges, the impact time, and the heliocentric distance for the three selected orbit segments. In addition, I plotted for the IDPs (left hand plots) and ISD (right hand plots) the impact charge expectation values as function of the time. The full dotted line indicates those values while the upper dashed line gives the upper impact charge limit, beyond which the probability of an interplanetary origin of the impactor is less than 5%. As discussed in Sec. 4.3.3, I am confident that the ISD grains contribute dominantly to the excess of particles above the upper line. On the right hand plots, the IDPs have been removed from the data sample. The theoretical impact charge profile for the ISDs has been calculated assuming a β-ratio value of 1. Note that beyond about 2.5 AU (orbit segment 3), the data set is dominated by ISD impactors. This fact, already shown by Baguhl (1996), is due to the detection geometry. Indeed, on the second half of segment 3, the sensitivity to IDPs on bound prograde orbits is strongly reduced because of the high eccentricity of the spacecraft trajectory. In contrast, the sensitivity to the ISD stream is high, leading to a dominant contribution of ISD impactors in the data sample.

As a whole, we identified about 115 ISD impactors between 0.7 AU and 3.5 AU. On segment 1, 21 ISD grains were obtained, making 22 % of the data sample. Despite of the data gap occurring during segment 2, the data sample could be exploited. The ISD contribution is about 23% of the corresponding data set, with 31 ISD impactors detected. At least, on segment 3, 63 interstellar impactors were identified and the relative interstellar contribution is increased to about 40% of the data sample.

As shown in Fig. 4.14, there is a good agreement on the segments 1 and 2 between the theoretical and the measured impact charges for ISD grains with $\beta = 1$. This finding supports the ISD identification scheme since it is consistent with the β ratio values expected for the 'typical' ISD in the inner solar system (Landgraf et al., 2003). However, on segment 1, higher impact charges than expected for those typical ISD grains have been measured. In contrast, on segment 3, the theoretical predictions for those ISD grains overestimate the measured impact charge. As the β-ratio value is a function of the mass (see Fig. 3.1), this leads to believe that bigger ISD impactors were detected on segment 1 and smaller ISD grains on segment 3. The next subsection deals therefore with an attempt to make a "β-ratio spectroscopy".

4.3.4 β-spectroscopy

Competition between radiation pressure and gravitation determines how deep an ISD grain can penetrate into the heliosphere. While grains whose dynamics is dominated by gravitation ($\beta < 1$) can reach the innermost region of the solar system, the penetration depth for grains with $\beta > 1$ depends on β and on the impact parameter *b*. Measurements of the ISD mass distribution performed with the *Ulysses* spacecraft revealed a lack of small ISD grains at close heliocentric distance (so-called β-gap, see (Landgraf et al., 1999)). This fact supports the idea that the ISD stream is filtered by the radiation

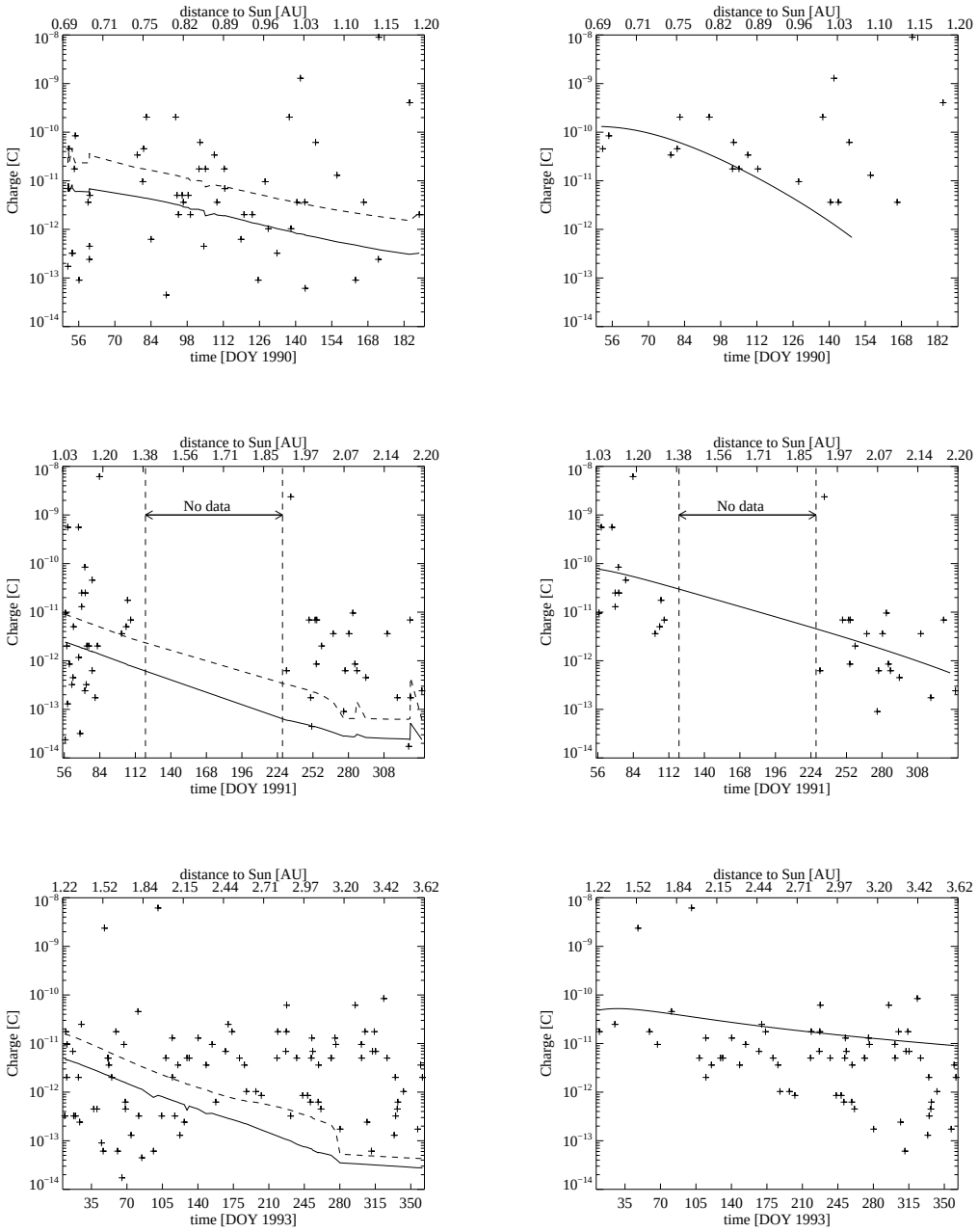

Figure 4.14: The plots on the left hand show the impactors analyzed on each orbit segment. The impact charge generated is plotted versus the impact time and the heliocentric distance. The full line gives the expected charge yield for IDPs. The dashed lines indicate the upper charge yield value. The plots on the right show the impactors identified as ISD grains The full line gives the expected charge yield for ISD grains characterized by β=1.

pressure. However, the heliocentric range covered by the *Ulysses* measurements did not allow a quantitative verification for this filtering, in contrast to the *Galileo* data. After a description of the 'β-spectroscopy' method, I will show that the *Galileo* measurements provide strong evidences for the radiation filtering effect.

ISD particles are supposed to be injected inside the heliosphere parallel to the $+X$ direction. Furthermore, the injection velocity of the ISD grains in the heliosphere is assumed to be v_∞ = 26 kms^{-1} (see Sec. 4.5.1). I consider in the following a dust grain with $\beta > 1$. In the simple case where b =0, one calculates the closest heliocentric distance r_{min} reached by an ISD grain juste writing the energy conservation, which gives

$$r_{min} = \frac{\mu(\beta-1)}{v_\infty^2}. \tag{4.10}$$

Consequently, an heliocentric distance r can be reached by an ISD grains only if $\beta < \beta_m$ with

$$\beta_m = 1 + \frac{r v_\infty^2}{\mu} \tag{4.11}$$

For $b \neq 0$, one can generalise this result, considering the hyperbolic trajectory of the dust grain. The eccentricity e and the deviation angle δ of the hyperbolic trajectory are given by $e^2 - 1 = \frac{b^2 v_\infty^4}{\tilde{\mu}^2}$ and $\sin\frac{\delta}{2} = \frac{1}{e}$, respectively. If one further assume $p = \frac{b^2 v_\infty^2}{\tilde{\mu}}$ and (r, f) to be the polar coordinates of the grain, the polar equation of the trajectory is given by:

$$r = \frac{p}{1 + e\cos(f - \frac{\delta}{2} + \frac{\pi}{2})}, \tag{4.12}$$

that can further be formed as

$$\frac{b^2 v_\infty^2}{\mu(1-\beta)} = r(1 + \sin^2 f \frac{b v_\infty}{\mu(1-\beta)} - \cos f), \tag{4.13}$$

which is a binomial equation of the variable b. Writing the condition of existence for b leads finally to $\beta < \beta_m$ with

$$\beta_m = 1 + \frac{r \sin^2 f v_\infty^2}{4\mu(1-\cos f)} \tag{4.14}$$

Lines of equal β_m are drawn in Fig. 4.16. They represent the boundary lines of exclusion zones shaped by the radiation pressure, that grains with $\beta > \beta_m$ can not penetrate, see Fig. 4.16.

The mass and the velocity within the heliosphere of an ISD grain is fully determined by its β ratio. Therefore, the impact charge q_i can be written as

$$q_i = \Xi_{P_{sp}, V_{sp}}(\beta), \tag{4.15}$$

where P_{sp} and V_{sp} are the spacecraft position and velocity, respectively. As q_i, P_{sp} and V_{sp} are known for each impact, one can finally solve Eq. 4.15 for β.

For a given spacecraft position, $P_{sp} = (r_{sp}, f_{sp})$ in polar coordinates, the set of compatible ISD interception trajectories is derived. Reforming Eq. 4.13 the problem is equivalent to find the impact parameter b of ISD with $\beta < \beta_m$ that ensures:

$$r_{sp} = \frac{b^2 v_\infty^2}{\tilde{\mu}}[1 + \sqrt{(1 + \frac{b^2 v_\infty^4}{\tilde{\mu}^2})}\cos(f_{sp} - \frac{\delta}{2} + \frac{\pi}{2})]^{-1}, \tag{4.16}$$

Note that for $\beta < 1$, this equation has two solutions, and for $1 \leq \beta \leq \beta_m$ only one.

Fig. 4.15 indicates the geometric sensitive detector surface for hyperbolic trajectories crossing the spacecraft as function of β. The assumed instrument pointing corresponds to a rotation angle of $\phi = 90^\circ$. Zero sensitivity implies either that no hyperbolic trajectory could be found or that the sensitive area to the ISD grain trajectory vanishes. Note that $\beta_m(segment1) < \beta_m(segment2) < \beta_m(segment3)$.

Provided that Eq. 4.16 has a solution, the orbital elements of the interception trajectory are calculated. In case of two solutions, I choose the shorter trajectory. This finally allows to estimate the function $\Xi_{P_{sp},V_{sp}}(\beta)$. Note that Ξ is a decreasing function of β. Indeed, if $\beta_1 < \beta_2$, $m_1 > m_2$ and $v_1 > v_2$ (see Sec. 4.5.1). Therefore, from Eq. 2.2 follows $q_1 > q_2$.

Fig. 4.17 sumarises the data set with respect to β. The left plot gives the distribution of β. As can be seen, a major contribution of grains with $\beta \sim 1.1$ is needed to explain the measured impact charges values. On the right plot, the β values for the ISD impactors are plotted as function of the time. Apparently, grains with low β value ($\beta < 1$) were detected during each orbit segment. Such grains account for the higher impact charge values detected since ξ is a decreasing function of β. In contrast, ISD with higher β-ratio values have been detected dominantly on segment 3. The concentration of impactors with $\beta = 1.2$ on segment 3 is issued by the $\beta(m)$ function used in this work, whose maximum is equal to 1.2. In fact, for those ISD grains, the β value may be higher.

The effect of the 'β-spectroscopy' can be seen more clearly if the β distribution is plotted as function of the heliocentric distance, (Fig. 4.18). The width of the bins has been chosen such to contain a least 5 impactors. ISD impactors detected beyond 2.5 AU are dominantly associated with $\beta = 1.1...1.2$. This is a reasonable result since the spacecraft was well outside the exclusion zone associated to $\beta = 1.2$, (see Fig. 4.16). Furthermore, due to the negative slope of the ISD mass distribution (see (Landgraf et al., 2000)), those grains have a higher spatial density and thus they are more likely to be detected than bigger ones.

Not only the heliocentric distance, however, should be taken into account for the β-spectroscopy. As shown in Fig. 4.16, the penetration depth of the ISD in the inner solar system also depends on the heliocentric longitude ξ. I define ξ as the angle between the line Sun-spacecraft and the downstream direction of the ISD stream. In particular, for $\xi = 0^\circ$, the Sun is between the spacecraft and the ISD stream (the spacecraft is 'behind' the Sun), while for $\xi = 180^\circ$ the spacecraft is 'in front' of the Sun. Fig. 4.19 shows the ISD impacts detected during the orbit segments (left). Three β ranges have been distinguished: $\beta > 1.1$, $0.9 < \beta < 1.1$, and $0 < \beta < 0.9$. In addition, the boundaries of the exclusion zones for different β values are shown. The right plots show the orbit segments as function of the heliocentric distance r and ξ.

Impactors with $\beta > 1.1$ have been detected dominantly on segments 2 and 3 and are in minority on segment 1. The first impactor with $\beta > 1.1$ was detected for $\xi \sim 100^\circ$ at 1 AU on segment 2 and for $\xi \approx 80^\circ$ at 1.3 AU on segment 3, in agreement with the polar equation of the exclusion zone boundary associated with $\beta = 1.1$. In contrast, few impacts with high β values have been detected on segment 1 since the spacecraft spent less time outside the 1.1-1.2 exclusion zones. Impactors with $0.9 < \beta < 1.1$ are, however, equally distributed over the three orbit segments. In particular, their distribution is independent of ξ, as expected for ISD grains with $\beta \sim 1$. Indeed, as for those grains gravity and radiation forces equilibrate, the spatial distribution of the grains is independent of the location in the solar system (Landgraf, 1998). At least, ISD grains with $0 < \beta < 0.9$ shows an interesting effect: they are dominant on segment 1 and 2. This corresponds to a spacecraft location in front of the Sun at less than 2 AU. We claim that this fact is an evidence for the gravitation focusing effect on big ISD grains, as detailed below.

The hyperbolic trajectories of ISD grains that could be detected in this region have a low impact parameter. As the velocity at the perihelion for grains on hyperbolic orbits is $v_p = v_\infty \sqrt{\frac{e+1}{e-1}}$, with $e = \sqrt{1 + \frac{b^2 v_\infty^4}{\tilde{\mu}^2}}$, the velocity at the perihelion is higher for grains with $\beta < 1$ and lower for grains with $\beta > 1$. Not only does the Sun accelerate the impactors having $\beta < 1$, it also increases their number density through gravitational focusing, according to (Fahr, 1968):

$$\frac{n}{n_\infty} = \frac{b^2}{r \sin\xi |2b - r\sin\xi|}, \tag{4.17}$$

where n_∞ is the number density of ISD grains value at infinity, and n is their number density at the spacecraft position. In addition, as the *Galileo* spacecraft is flying toward the ISD stream, the effective sensitive area to big impactors is further increased. The relative flux enhancement for a given β value is then given by:

$$\frac{F}{F_\infty} = \frac{v}{v_\infty}\frac{n}{n_\infty}, \tag{4.18}$$

v being the heliocentric velocity of a grain. For grains with $\beta = 0$, the flux can be increased up to a factor of 4. In what follows, I show that the ISD flux values derived

from our measurements support the theory.

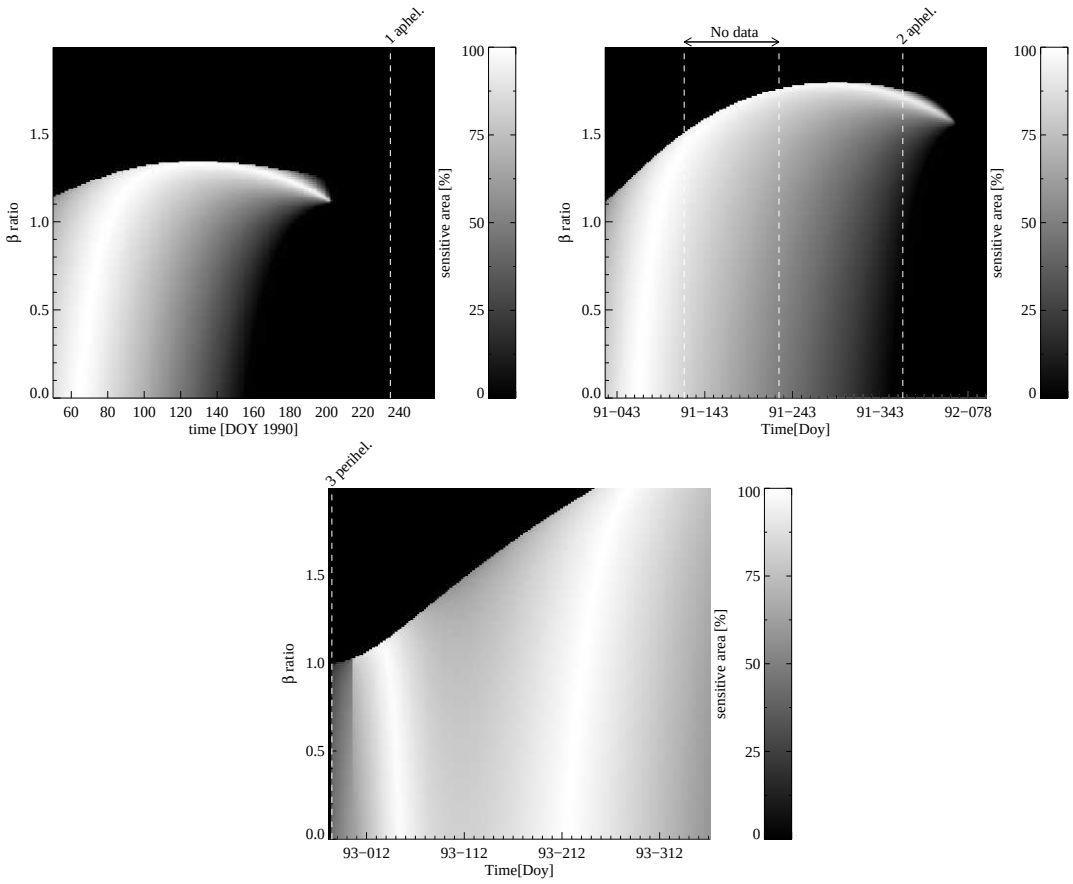

Figure 4.15: Theoretical sensitive area of the dust detector to the ISD stream as function of the β ratio and the time. Each plot covers one of the orbit segments presented in this work. The instrument pointing is defined by the rotation angle value $\phi = 90°$. The sensitive area is normed to its maximum value.

4.3.5 Flux calculations

The ISD flux has been calculated for each of the three β range values, and for each orbit segment. Note that I splitted segment 3 in two parts, called 3a and 3b. Segment 3b covers the heliocentric distance range beyond 2.5 AU. The flux values are plotted in Fig. 4.20.

In the range $\beta > 1.1$ (lower right panel), there are differences between the flux on the different orbit segments. The highest flux value (around $5{\cdot}10^{-5}\mathrm{m}^{-2}\mathrm{s}^{-1}$) is found for heliocentric distances beyond 2.5 AU and is reduced by more than one order of magni-

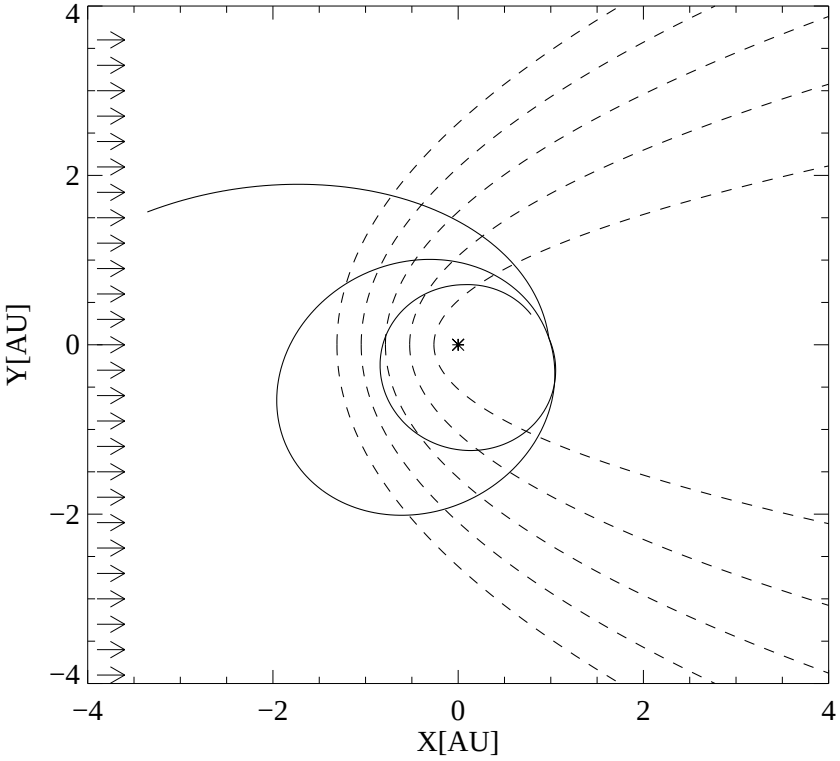

Figure 4.16: This plot shows the exclusion zones of interstellar grains, depending on the β value of the grain ($\beta > 1$). Assuming the ISD grains penetrating the Heliosphere along the +X direction (arrows), the radiation pressure may prevent them to reach the inner most region of the Solar System. The grains are deflected according to their β value and never cross the boundary line. Starting from the Sun, the dotted lines represents the frontiers of the exclusion zones for, respectively, $\beta = 1.1, 1.2, 1.3, 1.4, 1.5$. The trajectory of the spacecraft is also plotted in full line.

tude aroud 1 AU. This behavior is qualitatively in agreement with the radiation pressure filtering effect, preventing the smaller grains to reach close heliocentric distances.

The flux values calculated for ISD grains dominated by gravitation forces ($\beta \leq 0.9$) also confirm the theoretical expectations, as shown on the lower left plot. A flux of around $1.5{\cdot}10^{-5}\mathrm{m}^{-2}\mathrm{s}^{-1}$ is found for such particles on segments 1 and 2, located in front of the Sun. In contrast, a lower flux of such grains, around $3{\cdot}10^{-6}\mathrm{m}^{-2}\mathrm{s}^{-1}$ is found on segments 3a and 3b.

The flux values for $\beta \approx 1$ are also consistent with the theory, on the upper right plot. Independent on the orbit segment, the flux is approximately constant, about $1.5{\cdot}10^{-5}\mathrm{m}^{-2}\mathrm{s}^{-1}$. For those grains, radiation pressure and gravitation forces equilibrate, leading to a flux independent on the heliocentric location.

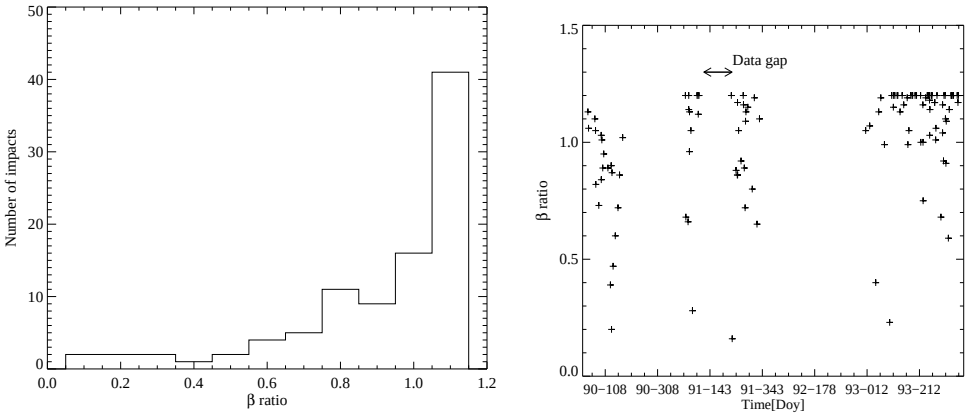

Figure 4.17: Distribution of the β value derived for the ISD impactors (left hand plot). On the plot on the right, all the β values are plotted as function of the time.

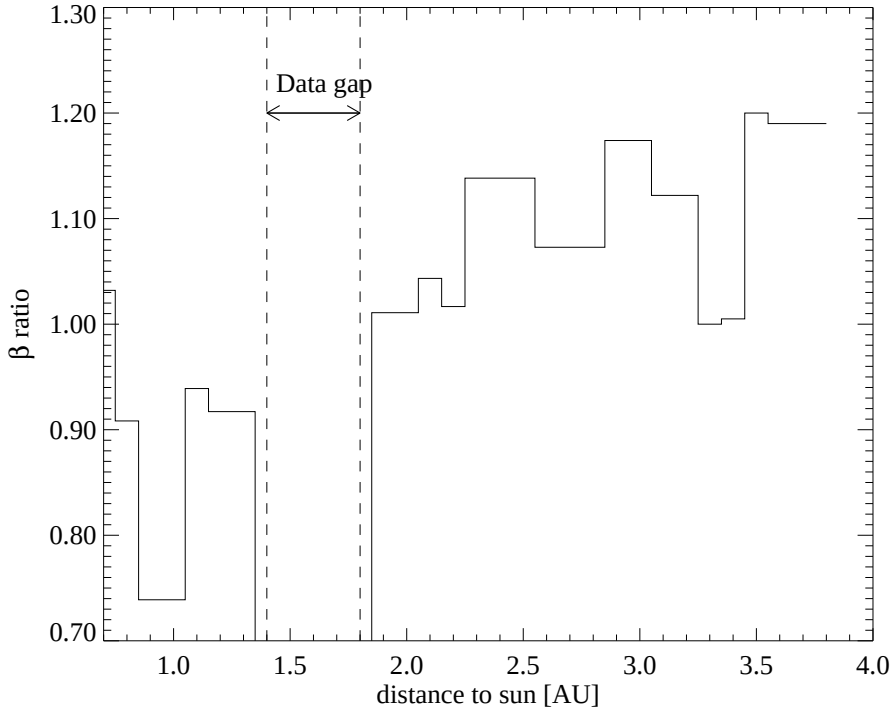

Figure 4.18: Distribution of the mean β value as function of the heliocentric distance. The width of each distance bin is chosen such that at least 5 impacts have been detected inside.

At least, in the upper left panel, all β value ranges have been taken into account.

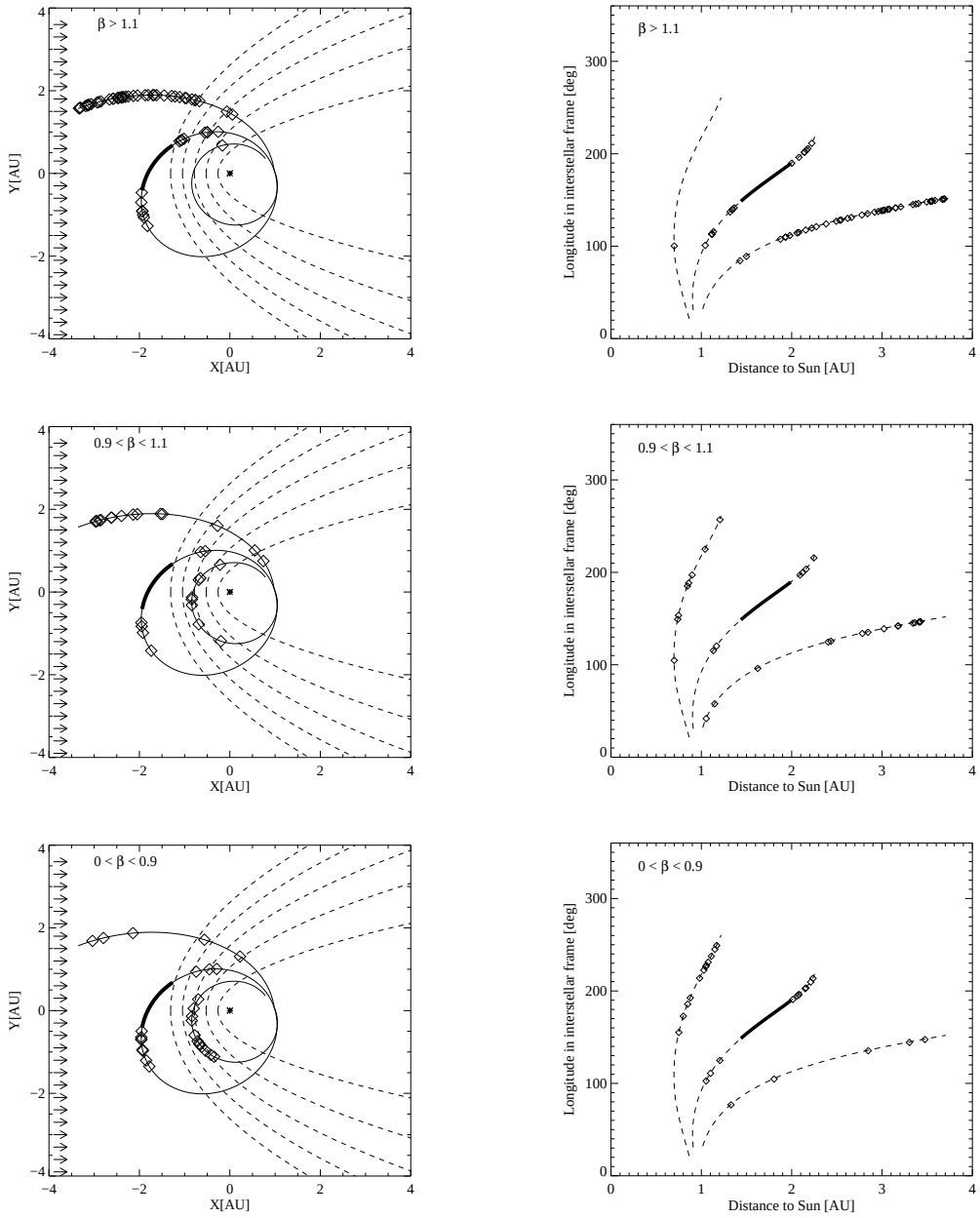

Figure 4.19: The detection location of each ISD impactors is plotted (symbols) on the trajectory of the spacecraft (full line). The +X direction is parallel to the injection direction of the ISD grains. The thicker line indicates the data gap. The dotted line gives the boundary of each exclusion zone, from $\beta = 1.1$ to $\beta = 1.5$. Three range values of β have been distinguished to plot the data: from the top to the bottom, $\beta > 1.1$, $0.9 < \beta < 1.1$, $\beta < 0.9$. For each β value range, on the right hand plots, the polar curve of segments 1,2,3 are plotted. The symbols represent the ISD impactors.

Orbit segments 3b and 3a show a decrease of the total flux with decreasing heliocentric distance. The flux for segments 1 and 2, however, is higher than expected from a linear extrapolation of the flux values on segments 3a and 3b. This may be explained by the enhancement of the flux of bigger grains through gravitation focusing on segments 1 and 2, as discussed in Sec. 4.3.4.

4.3.6 Discussion

In this section, I discuss several implications of the ISD stream monitoring with the *Galileo* spacecraft. The response of the instrument to the high energetic impacts generated by ISD grains will first be described. The non-nominal velocity determination by the rise-time method for high energetic impactors has been suspected for a long time but could never be verified experimentally on Earth. This is the reason why I only trusted the ion channel measurement throughout the data analysis for ISD as discussed in Sec. 2.4. The identification of ISD impactors provides an opportunity to verify this instrumental effect. In a second step, I discuss the agreement of the ISD flux measurements with the results obtained by the *Ulysses* and *Cassini* dust experiments. I finally stress the fact that the *Galileo* monitoring of the ISD stream at various locations in the inner solar system provides in-situ evidence for the gravitational focusing effect on the ISD stream, together with a quantification of the radiation pressure filtering.

Instrumental response In this subsection I confirm the non-nominal response of the *Galileo* instrument in case of high energetic impacts, like those caused by ISD grains. An overview of the impact data derived by the instrument for the impactors identified as ISD grains is given in Fig. 4.21. On the upper left plot, the rotation angle distribution is given. An interesting feature appears 90°. Instead of reaching its maximum, as expected theoretically, the distribution shows a lack of impacts. This is no longer surprising if one considers the mounting of the dust detector on the *Galileo* spacecraft (see (Grün et al., 1992b)). Indeed, for rotation angle values around 90°, the magnetometer boom lies in the ecliptic plane, between the downstream direction of the ISD stream and the dust instrument, and issues a shielding of the dust instrument's target (Krüger et al., 1999). As a consequence, some impactors hit the magnetometer boom structure and can not be detected by the dust detector, resulting in a lack of data.

Let us now prove the non-nominal impactor's velocity and mass determination by the instrument, for high energetic impacts. The plots in Fig. 4.21 clearly show those biased results for our ISD impactors. The velocity distribution derived from the instrument's response has a maximum lying around 10 kms^{-1}, whereas the impact velocity of the interstellar impactors are theoretically expected between 40-60 kms^{-1}. Also, the maximum of the mass distribution is lying around 10^{-14} kg, that is two orders of magnitude higher than expected for the ISD grains detected in-situ by the *Ulysses* dust instru-

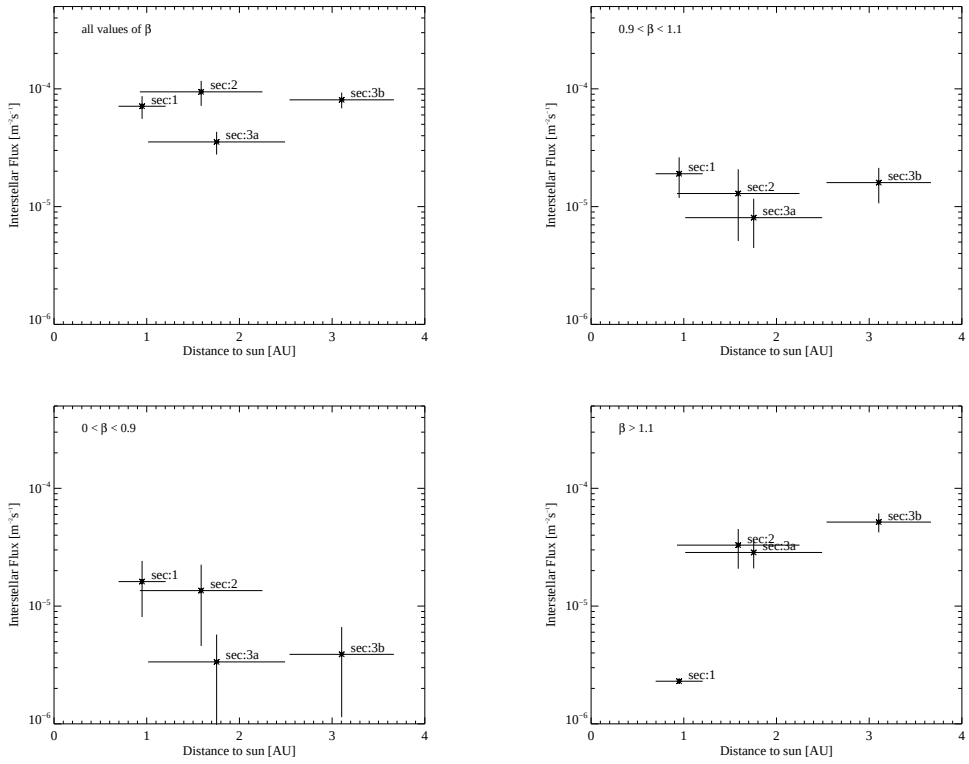

Figure 4.20: ISD flux values calculated on the different orbit segments. On the top left plot, the total flux values are plotted. On the top right plot, only the range $0.9 < \beta < 1.1$ is plotted. On the bottom left plot, only the range $\beta < 0.9$ is plotted, while only the ISD for which $\beta > 1.1$ are taken into account.

ment, see Sec.4.5.1. The reasons for the non nominal measurements can be resumed as follow. In case of high velocity impacts, sub-micrometer size particles generate more secondary ejecta. As those secondary ejecta also produce charges by impacting onto an other location of the spherical target, the multipliers keep on collecting charges from the secondary ejecta. This increases the impact rise time monitored by the instrument's software. Since the impact velocity has been found experimentally to be a decreasing function of the rise time, the impact velocity is therefore systematically underestimated by the instrument's software. Furthermore, as the ratio Qi/m is an increasing function of the impact velocity (see (Grün et al., 1992b)), the mass of the impactors will be systematically overestimated.

However, I claim that those biased results are only due to a non-optimum rise-time measurement of the impact charge signal, whereas the ion impact charge is measured properly.

In order to prove this affirmation, I use an indirect method. The dust instrument

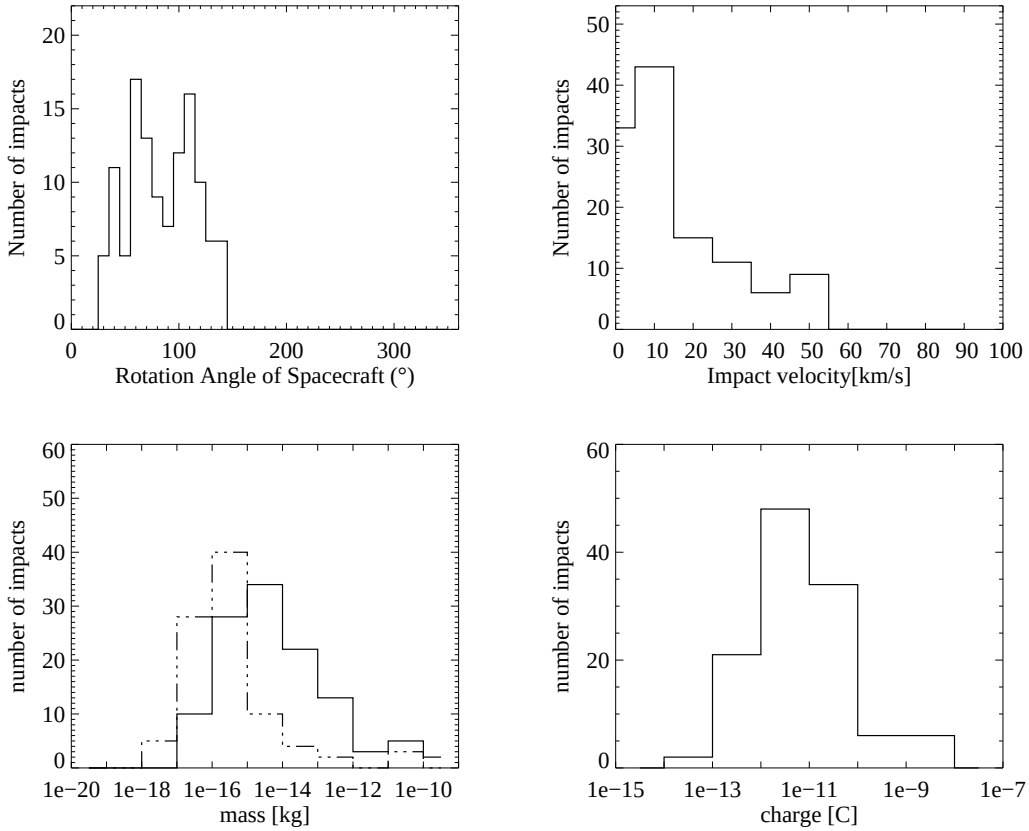

Figure 4.21: Some impact parameters directly provided by the instrument as response to the interstellar data sample. The plot on the left in the upper panel gives the rotation angle distribution, the plot on the top right gives the velocity distribution, as determined from rise-time measurements. In the bottom, two further plots gives respectively, on the left hand side the mass distribution and on the right hand side the ion impact charge distribution. The dashed dotted line on the mass distribution plot indicates the corrected mass distribution (see text).

on-board *Ulysses* is identical to the one flown on *Galileo*. As the *Ulysses* instrument monitored the ISD flux under nominal conditions (refering to the impactors energy), I rely on the mass distribution derived by Landgraf (2000) for the ISD grains. From this mass distribution was concluded that a major component of the ISD grains detected by *Ulysses* have $\beta \approx 1$. I replaced the biased values of the impact velocity found by the *Galileo* instrument by the theoretical impact velocity expected for ISD impactors with $\beta = 1$. Then, feeding Eq. 2.2 for the *Galileo* instrument with the measured *QI* value and the theoretical velocity values, I find the corrected mass distribution shown on the bottom left plot in dotted line. The peak of this new distribution around 10^{-16} kg is now consistent with the *Ulysses* measurements. From this I conclude the validity of the ion impact charge measurements, even in case of high energetic impacts.

As stressed in Sec. 2.4, this instrumental effect can not be verified experimentally, since no dust accelerator in the world is able to accelerate dust grains to the high kinetic energy reached by the ISD impactors in the spacecraft frame. As a whole, an indirect consequence of this study was to make use of the interstellar impactors as an 'astrophysics laboratory', leading to a better understanding of our instrument.

Implications and conclusions In this paragraph, I discuss the limitation of the ISD identification scheme. The method to discriminate ISD grains from the interplanetary background does not tell us with certainty the origin of an individual impactor. In particular, due to their high velocity relative to the spacecraft, retrograde IDPs are, like ISD grains, likely to generate high impact charges. However, such particles were not taken into account since they may not contribute significantly to the data sample, as supposed in Sec. 3.2.2. The *Galileo* data supports this hypothesis: if retrograde particles would contribute significantly to the data sample, the high impact charges should be equally distributed over the *Galileo* trajectory. This is not the case if one looks at the Fig. 4.11: high impact charges cluster where the sensitive area to ISD does not vanish. Therefore, I am confident that retrograde particles do not invalidate the identification of ISD. At least, applying the ISD identification scheme for data obtained beyond 2.5 AU, I found the same ISD flux of $0.9{\cdot}10^{-5}\mathrm{m}^{-2}\mathrm{s}^{-1}$ as in a previous analysis (see (Landgraf, 1998)), in which directional criteria only were used to identify the ISD grains. This supports the efficiency of the ISD identification scheme even where no directional criterion can be applied.

The analysis of the *Galileo* data for ISD show the penetration of ISD grains down to 0.7 AU. This conclusion is in agreement with the analysis of the *Cassini* data performed in Sec. 4.2, where a mean value for the ISD flux of about $3{\cdot}10^{-5}\mathrm{m}^{-2}\mathrm{s}^{-1}$ between 0.7 and 1 AU for $\beta \approx 1$ was derived. For the same β range values, I derive from the *Galileo* data a flux around $2{\cdot}10^{-5}\mathrm{m}^{2}\mathrm{s}^{-1}$. Furthermore, the *Cassini* measurements were performed in 1999, whilst the *Galileo* data were obtained between 1990 to 1993. Interestingly, although those measurements cover an interval of time of about a half solar cycle, I find no significant difference between the ISD flux values found around the Earth orbit distance for $\beta \approx 1$. This shows indirectly that the dust component of the ISD stream detected deep in the solar system do not interact significantly with the IMF. This fact will be discussed in more details in Sec. 5.3.

The *Galileo* spacecraft could monitor the ISD stream at various location in the inner solar system, covering a wider range of heliocentric distances and of heliocentric longitudes than the *Cassini* spacecraft. For the first time, a 'β-spectroscopy' could be performed, that allows the detailed analysis of the radiation pressure filtering on a large heliocentric distance range. Furthermore, the *Galileo* ISD data suggest locally spatial density enhancement for big ISD grains, that may explained by the gravitation focusing

effect. The implications of the *Galileo* finding will be discussed in Sec. 5.3.

4.4 Analysis of the HELIOS data

The *Helios* mission offers the opportunity to monitor the ISD stream closer to the Sun than the *Cassini* and *Galileo* missions. The *Helios* spacecraft, shown in Fig. 4.22, was the result of a US-German cooperation. Launched in 1974, the primary goal of this mission was to reach the perihelion of its elliptic trajectory around the Sun (see Fig. 4.23), performing measurements of the IMF, the solar wind, cosmic radiation, zodiacal light and the IDP distribution. Three months after the launch, the primary mission was a success, and the extended mission begun, consisting of 5 years measurements on the same orbit. As I will show in the following, this long measurement time together with a favorable orbit provided good conditions to detect ISD grains in the inner solar system.

Figure 4.22: Picture of the *Helios* spacecraft. Note the cylindrical shape. Helios was stabilized in rotation around its antenna axis, directed along the main axis of the cylinder and pointing to the ecliptic north direction. The solar arrays are distributed all around the spacecraft body. The magnetometer boom in the bottom performed measurements of the IMF.

4.4.1 Mission description

The *Helios* trajectory was within the ecliptic plane. The eccentricity of the elliptical orbit was about e = 0.56, the perihelion was located at 0.31 AU from the Sun and the aphelion at 0.98. The argument of the perihelion was 258.4°. The orbital period is about 190 days. The spacecraft was spinning around its antenna axis, the rotation being parameterised by the azimuth angle θ. Note that the origin of the θ angle is choose such as for both dust instruments, θ=90° indicates the Sun direction, and θ=0° gives the perpendicular direction toward the spacecraft apex motion.

Two twin instruments as described in 2.2.1 are mounted on the spacecraft body as shown in Fig. 4.24. I will refer in the following to the sensor A and to the sensor B (see Fig. 4.24) as the 'south sensor' and the 'ecliptic sensor', respectively. Indeed, the sensor A is sensitive to dust particles on high inclined prograde orbits. Observed from the spacecraft point of view, those particles come from the ecliptic south direction. For similar raisons, the sensor B is called the ecliptic sensor since its field of view fully scanned the ecliptic during one spacecraft rotation. Note that the field of view of each instrument is further constrained by the spacecraft structure. As the ecliptic sensor looks toward the Sun one time per rotation, an additional metal foil covers the instrument aperture. This foil prevents solar radiations to trigger noise events, but can be traversed by dust impactors (Grün, 1981). In contrast, the south sensor is protected against the solar plasma only.

4.4.2 Data description

From 1974-353 to 1980-002, the *Helios* dust experiment transmitted the data of 235 dust impacts to the Earth. The impact identification and noise discrimination scheme is described in details by Grün (1981). For the analysis of the *Helios* data for an ISD contribution, I used solely the following impact parameters: the date of the impact t, the distance to the Sun r, the true anomaly η , the azimuth angle θ and the ion impact charge digitalized in 4 amplitude classes QI_c.

In addition, the time-of-flight (TOF) mass spectra analysed by Grün (1981) were also taken into account. Although those TOF mass spectra gives only a rough elemental composition of the detected dust particle, their resolution was high enough to show evidences of two different types of spectra. The so-called '*Ch*' (for chondritic type) shows features that are typical for silicates rich particles, while the type '*Fe*' (for iron type) account for iron rich particles (Grün, 1981). The *Fe* spectra could be calibrated during laboratory experiments. In contrast, the *Ch* spectra features are expected from the theory only. However, both spectra types have been observed during the *Helios* mission, see Fig. 4.25. TOF spectra that did not match any of the identified spectrum type are said to be from '*Un*' type (for unidentified).

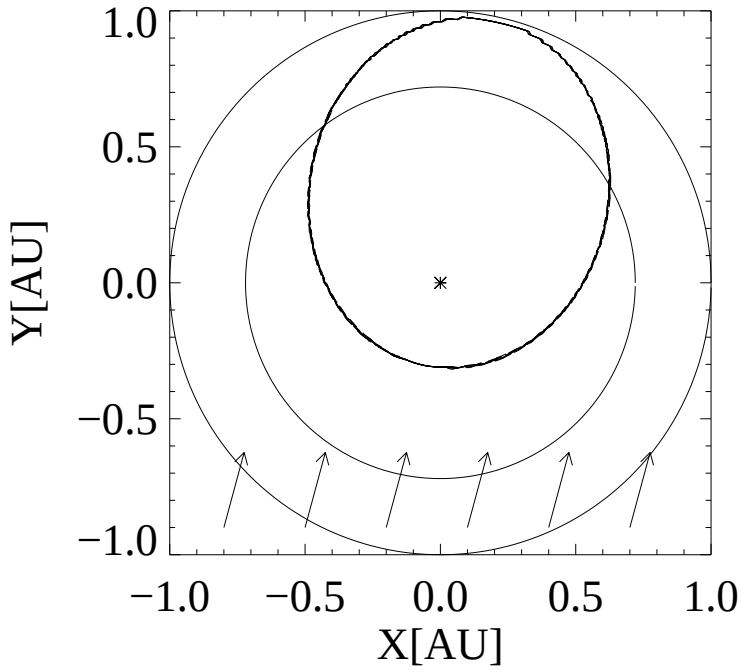

Figure 4.23: Trajectory of the *Helios* spacecraft in the ecliptic reference frame. The perihelion of the elliptic orbit is located about 0.3 AU from the Sun, and the aphelion at Earth orbit distance from the Sun. Orbits of the Earth and Venus are also plotted. The arrows represent the injection direction of the ISD stream in the heliosphere. Note that the ISD stream direction is almost parallel to the apsides line of the *Helios* trajectory.

As shown throughout the analysis of the *Cassini* and *Galileo* data, the ion impact charge is a crucial parameter in the data analysis for ISD. However, there was an important caveat in the case of the *Helios* data: the original values of the ion charge yield have been lost and only the amplitude classes QI_c are still accessible. Although the total amplitude of charge Q_{sp} providing the time-of-flight mass spectra represents well the initial ion impact charge, I decided to reconstruct the original impact charge yield values *QI* through a 'reversed proceeding' of the data. This was achieved using the calibration equations of the instrument together with the mass and impact velocity values found by Grün (1980). An important difficulty appeared because both mass and velocity value have been inferred in this work using both the ion and electron channels. Since the electron channel leads to an underestimation of the grain mass in case of high energetic impacts (see Sec. 2.4) the reversed proceeding of the data taking only the ion channel into account, leads to an underestimation of *QI*. This effect has been verified, as shown in Fig. 4.26: many of the reconstructed *QI* values for high impact charges do not correspond to their amplitude class value QI_c and are found in lower classes. Therefore, an empiric correction had to be applied. To find a correction scheme, I could

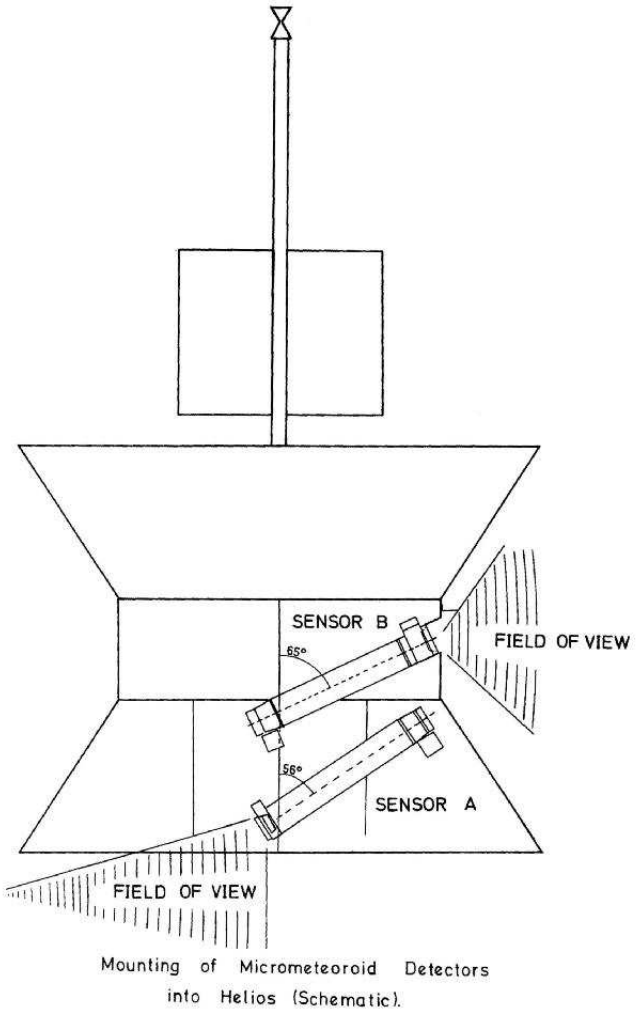

Figure 4.24: Schematic of the *Helios* spacecraft, carrying the twin dust sensors. Sensor B is also called the ecliptic sensor, since it is sensitive to dust particles on low inclined orbits, while Sensor A is called the south sensor, since it is sensitive to particles coming from the ecliptic south direction.

fortunately use the original plot of the ion charge yield distribution (still conserved!), as published in Grün (1981). The right hand plot in Fig. 4.26 shows finally the reconstructed *QI* values with correction, now corresponding well to their amplitude class. Furthermore, this plot is similar to the original from Grün (1981), made with the 'real' impact charge values. Note, however, that the reconstructed impact charges of high energetic impactors (about 40 particles in the upper amplitude class), are still underestimated: while in Fig. 4.26 the dominant contribution shows impact charge yields around 10^{-11} C, the dominant contribution for the amplitude class 4 in the original dis-

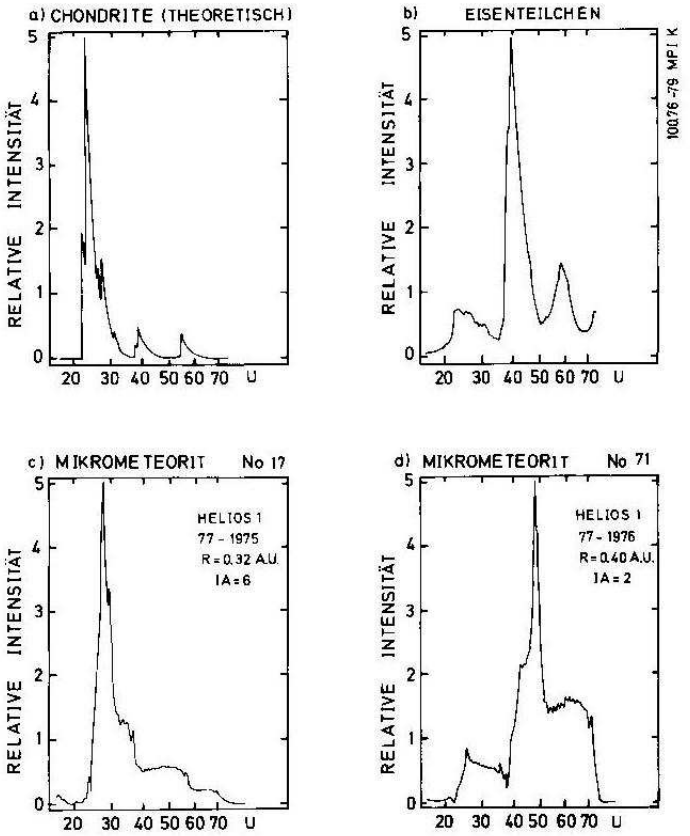

Figure 4.25: TOF mass spectra as measured by the *Helios* dust instrument. The two upper plots show, on the top left, a theoretical TOF spectrum for chondritic material, and on the top right, a TOF spectrum measured in the laboratory with iron particles. On the bottom are shown two TOF mass spectra obtained during *Helios* flight. The left one matches very well the theoretical chondritic spectrum, while the right one account for an iron rich dust grain.

tribution was rather around 10^{-10} C (see (Grün, 1981)).

The impactors detected with the south sensor and those obtained with the ecliptic sensor are shown in a (η,θ)-diagram in Fig. 4.27. The contour-lines represent the sensitive area of the instrument to populations on circular orbits. Note that all possible values of the β ratio ($0< \beta <1$) for IDP on prograde circular orbits have been taken into account for this calculation. This plot reveals between the two sensors a different distribution of the impactors in the (η,θ)-space. While the impactor distribution of the ecliptic sensor can be almost completely explained by impactors on circular or low eccentric orbits, high eccentric orbits are needed to account for the impactors distribution of the south

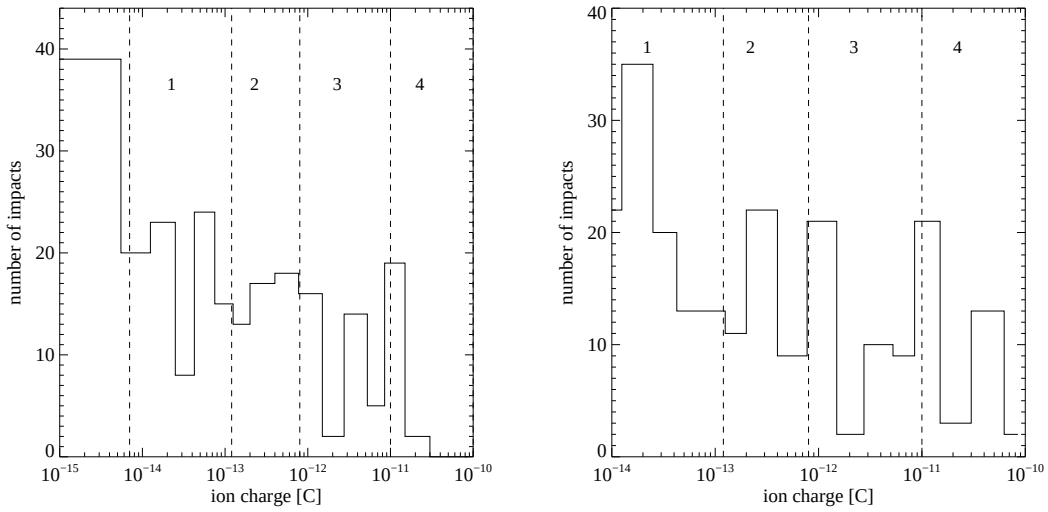

Figure 4.26: Distribution of the ion impact charge amplitude *QI*. The plot on the right shows the distribution after 'reversed proceeding' of the QI_c data (see text). On the left hand, the corrected distribution is plotted. The vertical dotted lines represent the amplitude class boundaries.

sensor. This fact was already discussed by Grün (1980). According to the analysis of this author, the ecliptic sensor was not sensitive to particles on high eccentric orbits because of the foil protecting the instrument against UV radiation, see Sec. 4.4.1.

4.4.3 Identification of ISD impactors

In this section, I aim at finding criteria that allow to discriminate ISD grains from the population of IDPs. Similar to the analysis of the *Cassini* and *Galileo* data, the values of the ion charge yield QI will play a key role, together with a geometrical analysis of the problem.

The main goal of the geometrical analysis consists in removing from the data set presented in Fig. 4.27 the impactors that *cannot* be ISD grains. In particular, an impactor detected with an azimuth angle θ is discarded as 'ISD candidate' if the sensitive area of the instrument vanishes for all possible values of the β-ratio. Details about the calculation of the sensitive area for an ISD grain characterized by a given β-ratio are given in Sec. 4.3.4 and Appendix. A.2.

Finally, in Fig. 4.28, only the impactors that could not be discarded by geometrical considerations are plotted. Each of those impactors *may* be an ISD grain, if one considers only the detection geometry. However, those two plots show that the remaining data set can also account for particles on circular or low eccentric orbits.

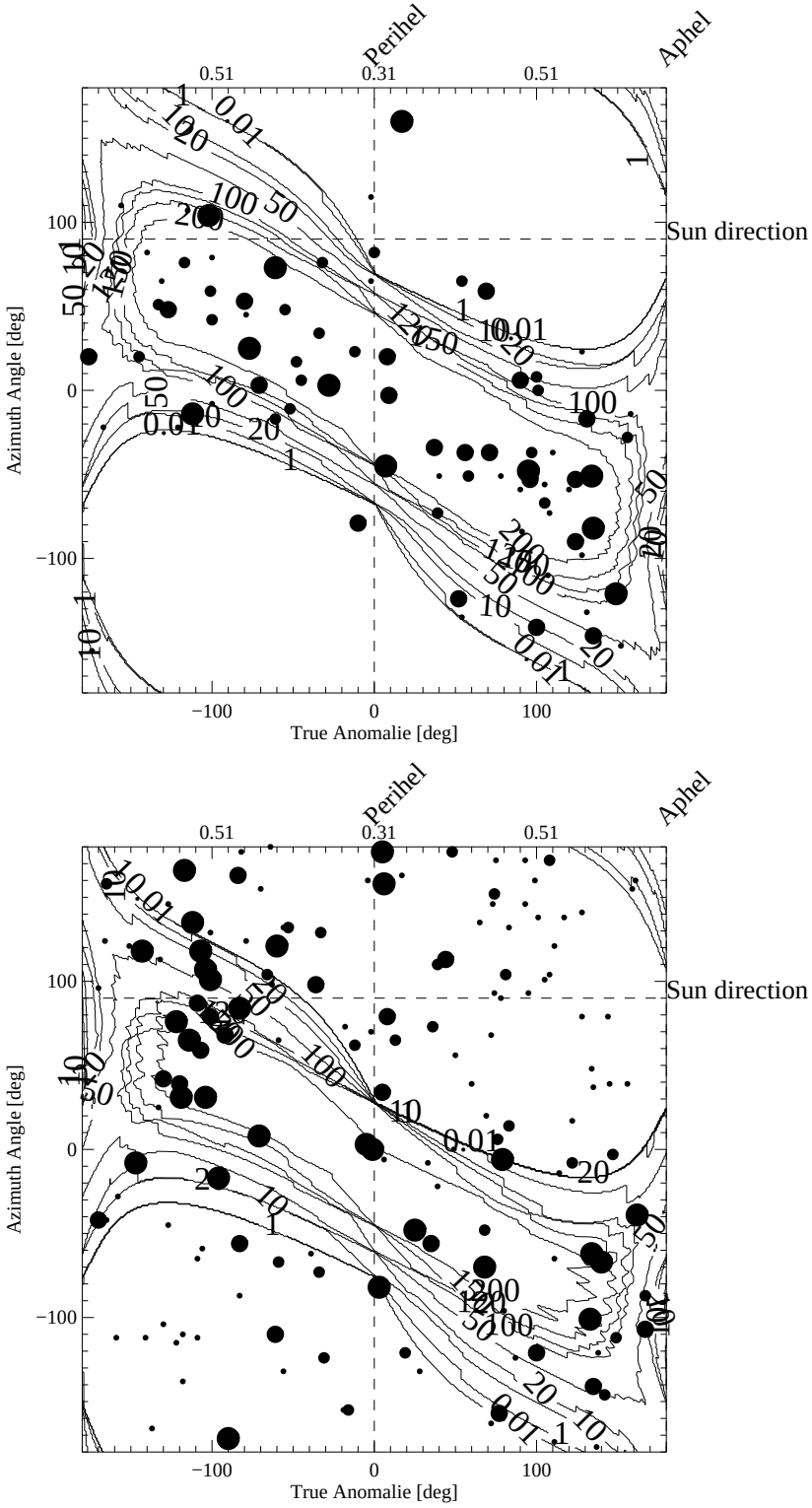

Figure 4.27: Impactors detected by, respectively, the ecliptic sensor (on the top), and the south sensor (on the bottom) in a (η,θ)-diagram. The impactors are represented by circles whose surface is proportional to QI_c. The contour-lines give the sensitivity to interplanetary populations on circular orbits. The dotted vertical line and the horizontal lines give, respectively, the perihelion and the Sun direction. The upper range indicates the heliocentric distance.

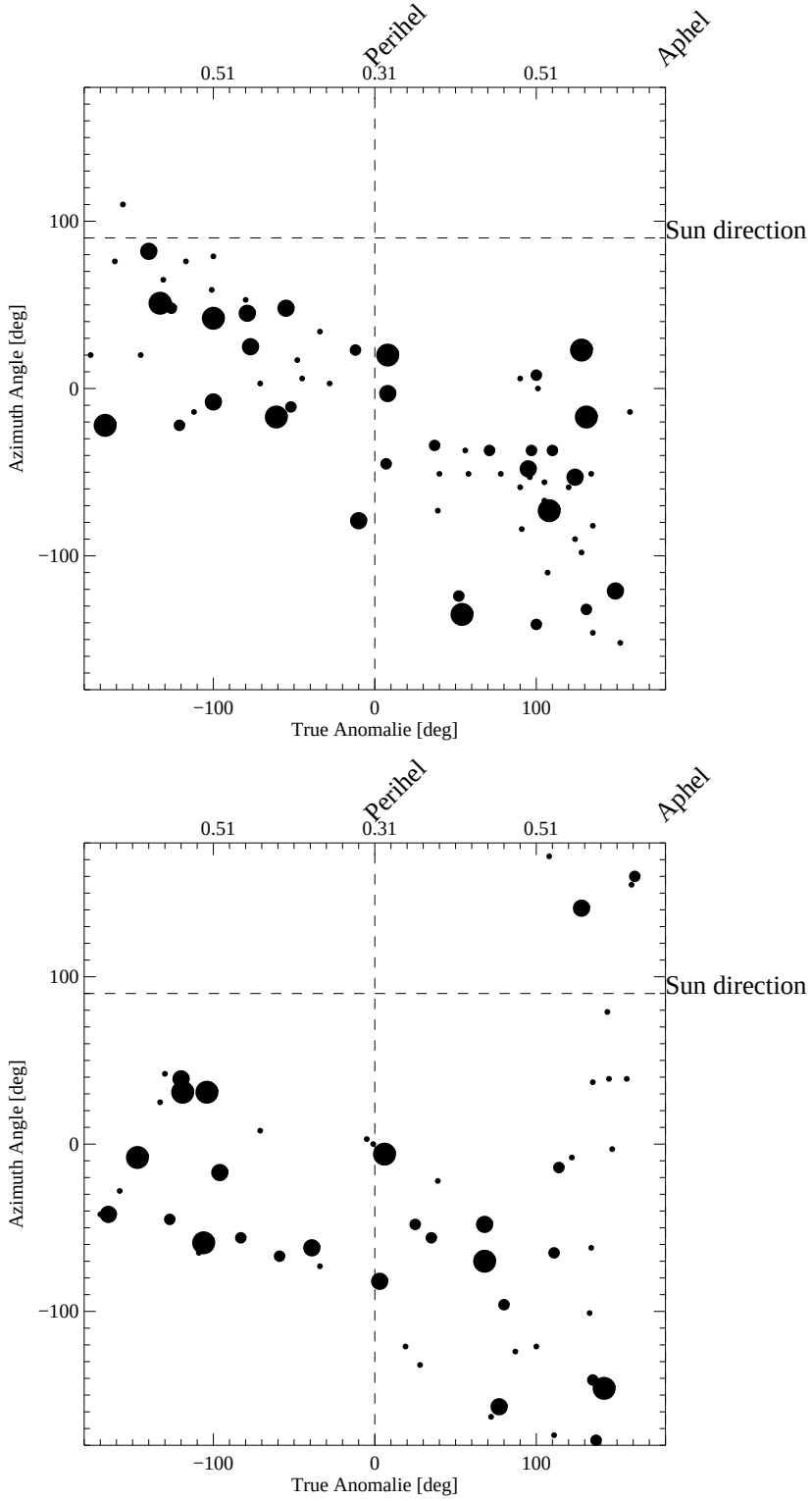

Figure 4.28: Impactors detected by, respectively, the ecliptic sensor (on the top), and the south sensor (on the bottom) in a (η,θ)-diagram. All impactors that are not compatible with an interstellar origin have been discarded, based on geometrical calculations. The dotted vertical line and the horizontal line gives, respectively, the perihelion and the Sun direction. The upper range indicates the heliocentric distance.

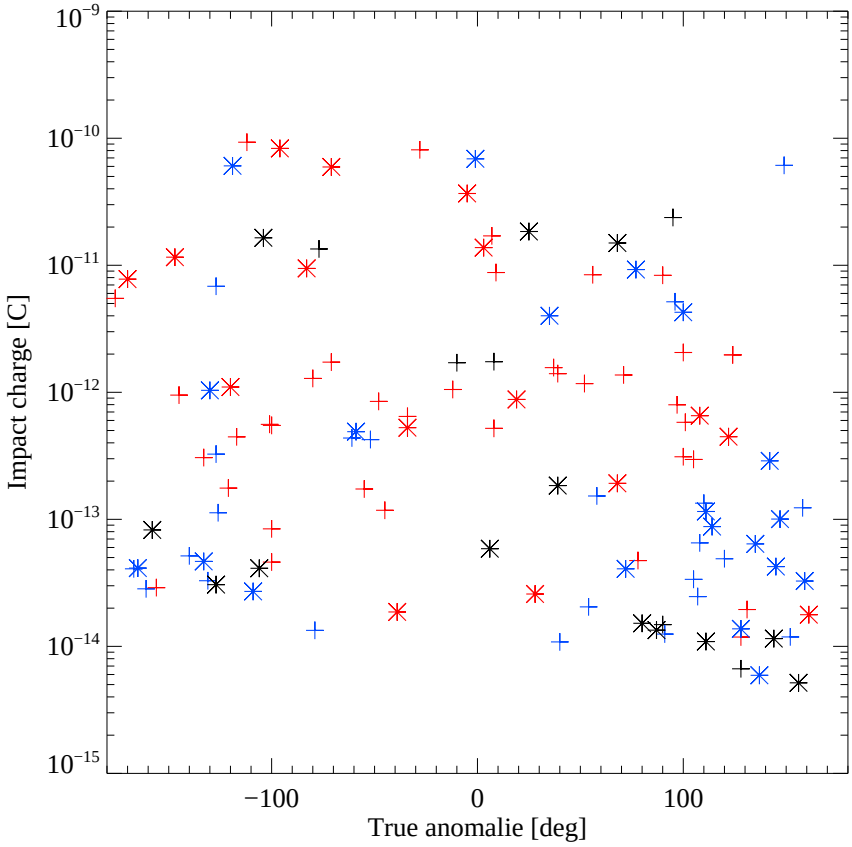

Figure 4.29: Impact charges detected by the ecliptic (crosses) and the south sensor (asterisks). The colors account for the TOF mass spectrum type. Fe-type spectra are in blue, Ch-type spectra in red and Un-type spectra in black. Note that 8 impactors, suspected to be issued by a cometary trail, have been removed from the data set (see text).

The *QI* values of the ion charge yield for both sensors are plotted as function of the true anomaly η on Fig. 4.29. The spectrum type is also given for each impact. It should be noted at that point that 8 further impactors, with high impact charges and clustering around η= 140°, have been removed from the data set and have not been plotted in Fig. 4.29. Indeed, those impacts showed a suspect clustering and revealed a probable origin from a cometary trail, crossed once per orbit by the spacecraft. This will be closer investigated in a further work.

Fig. 4.29 shows an asymmetric distribution of the ion charge as function of η. In particular, 12 particles with impact charges higher than 10^{-11} C has been detected with

$\eta < 0$ and only 4 with $\eta > 0$. As $\eta = 0$ is the perihelion position, this means that an excess of high impact charges have been detected on the left part of the orbit with respect to the line of apsides (see Fig. 4.23). I claim that this excess is not consistent with an interplanetary origin. Indeed, if v is the spacecraft velocity, it is obvious that $v(\eta) = v(-\eta)$. Assuming the rotational symmetry of the orbits and of the spatial density of the IDP populations, (see Sec. 3.2.1), this should lead to $n_{imp}(\eta) \approx n_{imp}(-\eta)$ in each impact charge range, n_{imp} being the number of impactors detected.

I will now show that the impact charge distribution in Fig. 4.29 can be fitted with the contribution of an ISD population together with a population of IDPs on circular orbits. Assuming the ISD stream model presented in Sec. 3.2.2, I performed calculations to find the theoretical impact velocity function $v_{imp}(\beta, \eta)$ of ISD grains on the instrument target. Using the calibration curve of the instrument (see Sec. 2.3) and the $\beta(m)$ ratio (see Fig. 3.1), I derived the theoretical impact charge yield function $QI_{theo}(\beta, \eta)$. In addition, I calculated the effective sensitive area function $A_{eff}(\beta, \eta, \theta)$ that takes the motion of the spacecraft relative to the ISD stream into account (see Sec. 4.2.2 and Sec. 4.3.2). I performed the same calculations for IDPs on circular orbits. The results are plotted in, respectively, Fig. 4.30, Fig. 4.31, and Fig. 4.32. Note that in Fig. 4.32, the averaged value of $A_{eff}(\beta, \eta, \theta)$ over one spacecraft rotation is plotted.

The qualitative interpretation of the theoretical calculations leads to the following conclusions. As shown in Fig. 4.32 the sensitivity for ISD grains increases from the aphelion to the perihelion, and reaches a maximum for $\eta \approx -30^\circ$. Furthermore, the position of the maximum does not depend on the value of β. However, the smaller the value of the β ratio, the higher the maximum of the sensitive area, resulting in a higher sensitivity for big ISD grains. In contrast, on the right part of the orbit, from the perihelion to the aphelion, the sensitivity for ISDs decreases, reaching a minimum for $\eta \approx 140^\circ$. As a whole, the probability function for ISDs detection is not symmetric with respect to the line of apsides and the best geometrical conditions are met for $-180^\circ < \eta < 90^\circ$.

Expected impact velocities for ISD particles are given in the right hand plots in Fig. 4.30 for two β-ratio values. Impact velocities up to 100 kms^{-1} are expected at $\eta \approx -40^\circ$ for ISD grains for which β=0. The maximum impact velocity is decreasing with increasing β-ratios as shown on the upper right hand plot. However, even for ISD with β=1, the impact velocity goes up to 60 kms^{-1}. In contrast, the impact velocities expected for IDPs on circular orbits are much lower, as shown on the left hand plots. The maximal impact velocities are reached for $\eta \approx 30^\circ$. For big IDP grains (β=0), the maximum impact velocity is about 30 kms^{-1} while for grains for which β=0.5 the maximum is less than 40 kms^{-1}.

From the comparison of the expected ion charge for IDPs and ISD in Fig. 4.31, one can see significant differences in the shape of the $QI_{theo}(\beta, \eta)$. For the ISD grains, the maximum of $Q_{imp}(\eta)$ is reached for $\eta \approx -40^\circ$ while for IDPs, the maximum of $Q_{imp}(\eta)$

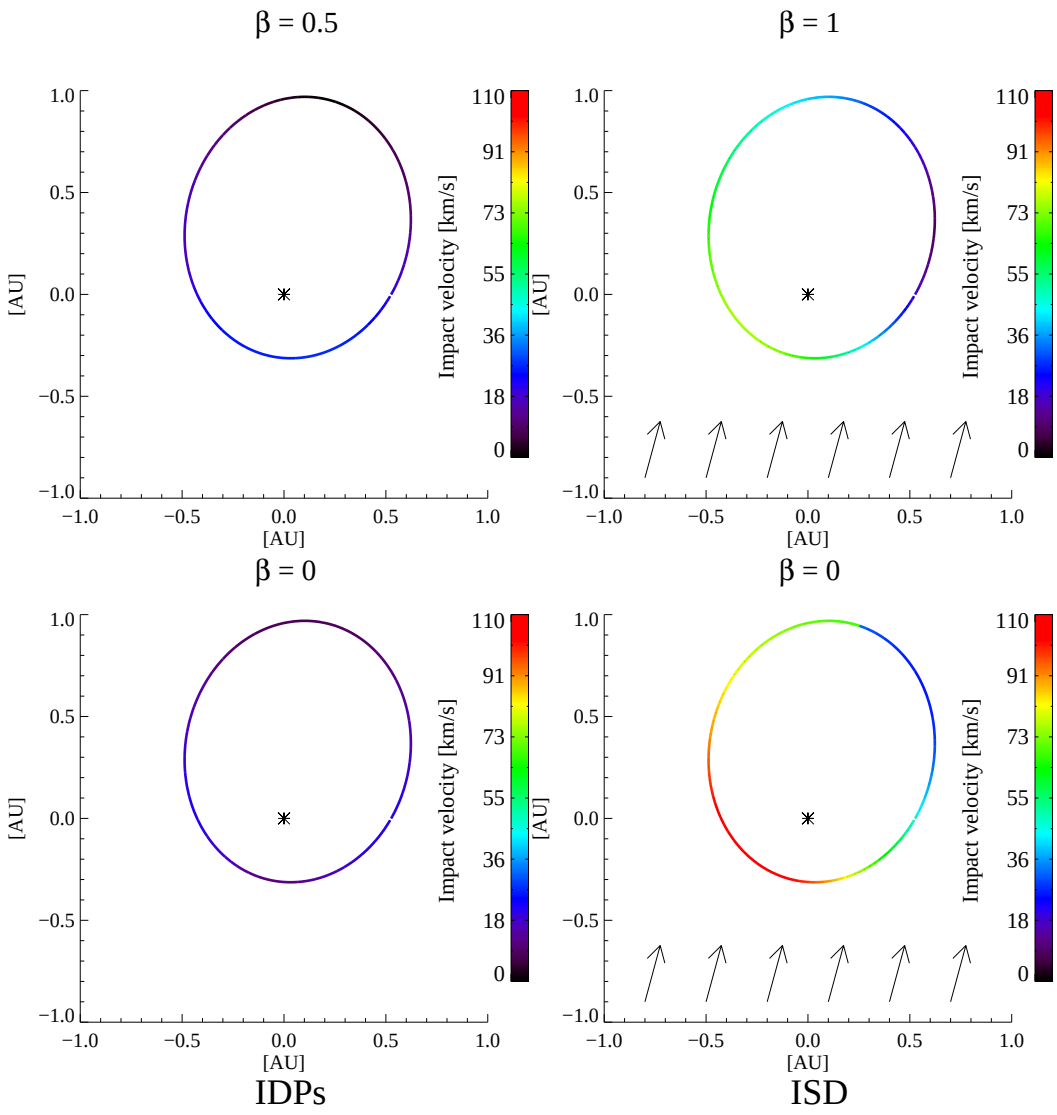

Figure 4.30: Theoretical impact velocity values calculated for IDPs on circular orbits (on the left) and for ISD grains (on the right). For each population, two different β-ratios have been assumed for the calculations. The ISD stream direction for $\beta = 1$ is symbolized by the arrows. Note the high impact speeds of ISD grains on the left part of the orbit, close to the perihelion.

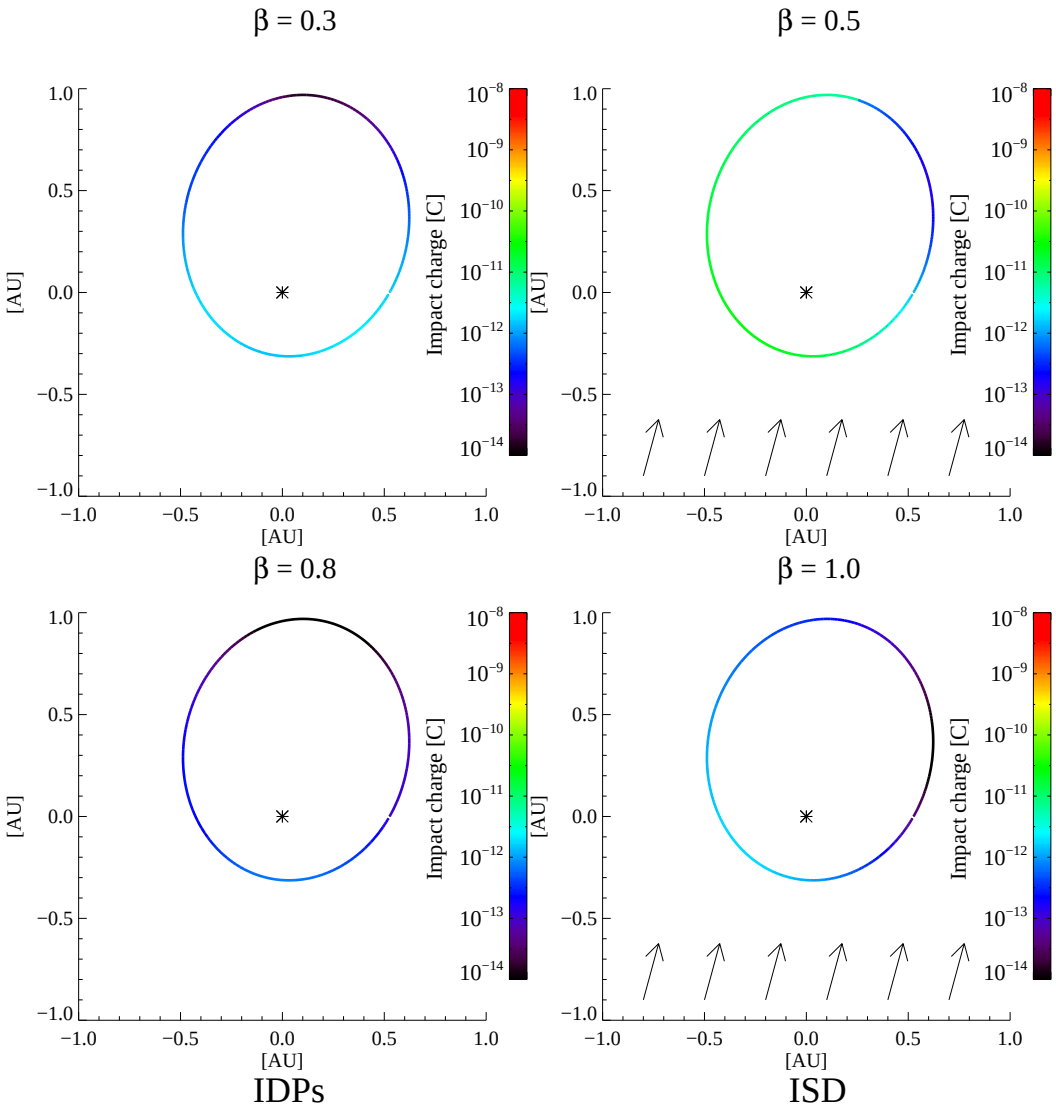

Figure 4.31: Theoretical impact charge calculated for IDPs on circular orbits (on the left) and for ISD grains (on the right).For each population, two different β-ratio values have been assumed for the calculations. The ISD stream direction for $\beta = 1$ is symbolized by the arrows. Note that big IDPs ($\beta \approx 0.3$) can generate as much charges as small ISD grains ($\beta \approx 1$). The highest impact charges, however, are generated by big ISDs, for spacecraft locations close to the aphelion.

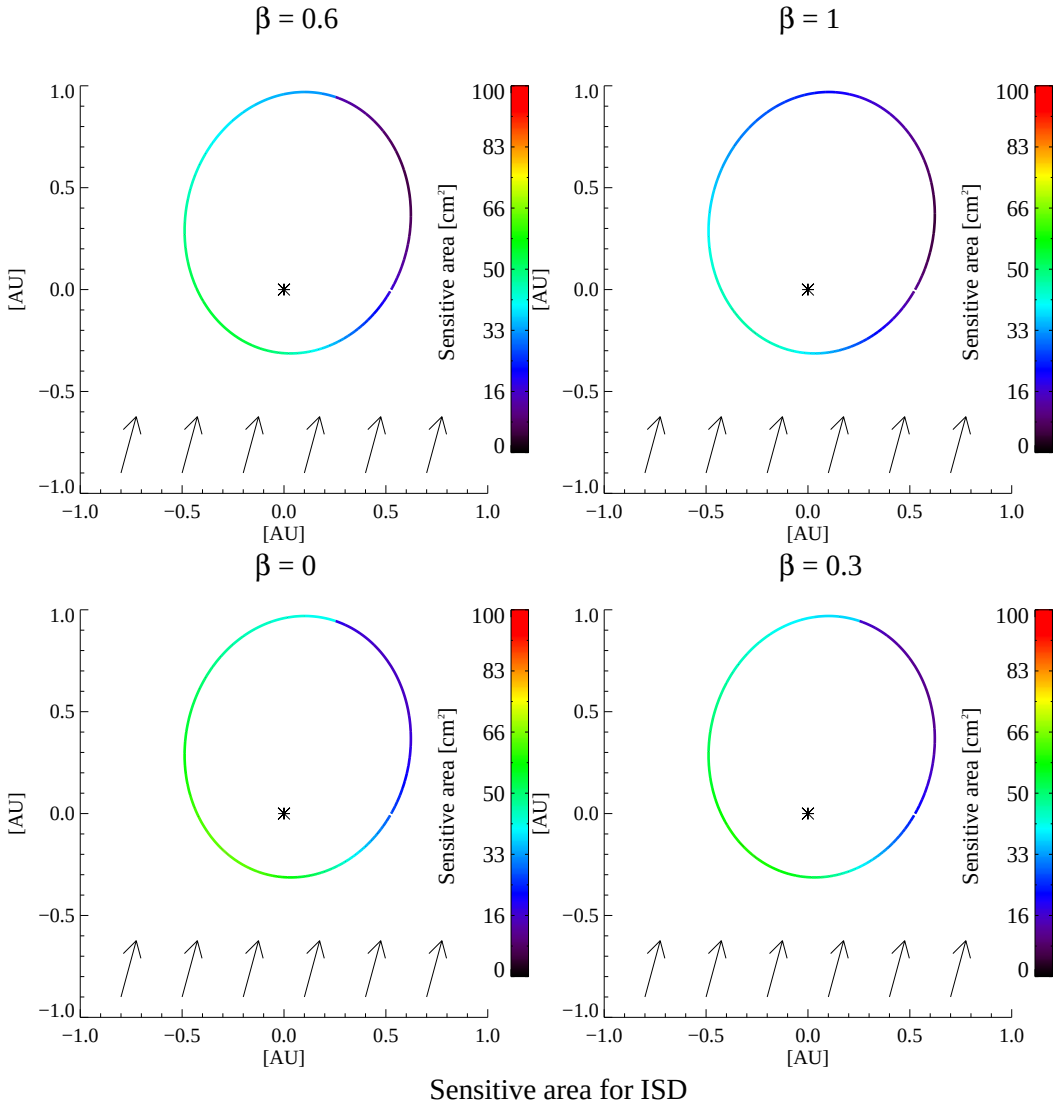

Figure 4.32: Effective sensitive area for different populations of ISD grains, characterized by their β-ratio values. The sensitive area of both detectors have been taken into account and averaged over one spacecraft rotation.

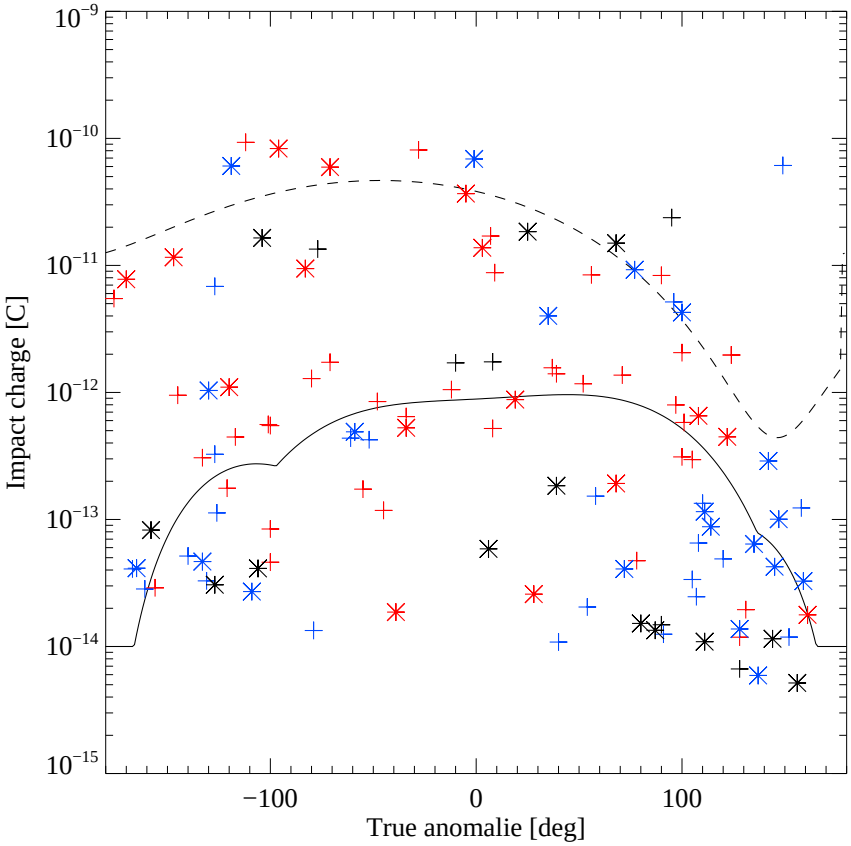

Figure 4.33: Impact charges detected by the ecliptic (crosses) and the south sensor (asterisks). The colors account for the TOF mass spectrum type. Fe-type spectra are in blue, Ch-type spectra in red and Un-type spectra in black. The full line shows the mean impact charge expected for IDPs on circular orbits as function of η. The dashed line shows the theoretical impact charge generated by ISD grains for which β =0.4.Note that 8 impactors, suspected to be issued by a cometary trail, have been removed from the data set (see text).

is reached shortly after the perihelion. The difference between the impact charge generated by IDPs and those generated by ISD impactors still depends on the β ratio assumed for each population. However, on the orbit part defined by $-180^\circ < \eta < 90^\circ$, big ISD grains may generate much higher impact charges than IDPs, (see Fig. 4.31).

I used the theoretical results described above to interpret the impact charges plotted in Fig. 4.29. It turned out that the data can be well fitted using two populations: ISD grains and IDPs on circular orbits, both characterized by their β-ratio. Then, I optimized the β-ratio for each population, in order to find the $Q_{imp}(\beta, \eta)$ functions that

fit the data best. The result is plotted in Fig. 4.33. As shown on this plot, impactors that generated high impact charges ($QI > 2 \cdot 10^{-12}$ C) are well fitted by ISD grains for which $\beta \approx 0.4$, while the lower impact charge range is well fitted by IDPs on circular orbit with $\beta \approx 0.5$. The β-values for the ISD impactors range from 0.3 to 0.7. This corresponds to a mass range [10^{-15} kg,10^{-14} kg], equivalent to particle radii between 1 and 2 μm.

4.4.4 Discussion and preliminary conclusions

Based on the argumentation developed in Sec. 4.4.3, I finally conclude that impactors such as $-180^\circ < \eta < 90^\circ$ and $QI > 2 \cdot 10^{-12}$ C are mainly from interstellar origin. About 25 impactors fulfill this criterion. The uncertainty in the number of detected ISDs can be estimated statistically, leading to 5 impactors. As the orbital period of the *Helios* spacecraft was about 6 months the orbit segment defined by -180° < η <90° was flown 10 times between 1975 and 1980. If t_0 is the time where the spacecraft passed its aphelion and t the time where the spacecraft reached the position η =90°, $\Delta t = t - t_0$ can be calculated using the Kepler equation

$$M = E - e \sin E, \tag{4.19}$$

where M is the mean anomaly, e the eccentricity and E the eccentric anomaly. Furthermore, M is a function of time as

$$M = \sqrt{\frac{\mu}{a^3}}(t - t_0), \tag{4.20}$$

where a is the semi-major axis of the trajectory.

At least, knowing that

$$\tan\frac{\eta}{2} = \sqrt{\frac{1+e}{1-e}} \tan\frac{E}{2}, \tag{4.21}$$

I can find Δt and write the function $A_e ff(\eta, \beta)$ as $A_e ff(t(\eta), \beta)$. Through time integration of $A_e ff(t(\eta), \beta)$ for $\beta = 0.4$ follows the ISD flux value measured. Note that measurements were performed in average only 61.5 % of the total time (Grün, 1981). This factor has to be taken into account for the flux calculation. The resulting mean flux for $\beta = 0.4$ is of $2.6 \pm 0.3 \cdot 10^{-6}$ m^{-2}s^{-1}, taking into account the uncertainty in the number of ISD impactors.

Interestingly, the β-ratio found for those ISD grains implies bigger sizes (about 1 μm) than the typical grains observed by *Ulysses* (radii about 0.3 μm, $\beta \approx 1.1$ (Landgraf et al., 2003)). In addition, the flux for those bigger grains is about 100 times smaller than the mean ISD flux measured between 3 AU and 5 AU. One reason may reside in the fact that the ISD stream component characterized by $\beta = 1$ could not be discriminated from the IDP background with the *Helios* sensors. Indeed, Fig. 4.33 shows that those ISDs generate at maximum around 10^{-12} C, that is in the same range as IDPs.

The ISD identification scheme is therefore more sensitive to big ISDs, that may lead to an underestimation of the total ISD flux. However, the flux value found for the big ISD grains is consistent with the general understanding of the ISD stream alteration in the heliosphere, as shown in the following.

The contribution of micron-size ISD grains or bigger ones in the *Ulysses* data set was smaller than those of the 'typical' grains with size of 0.3 μm (Landgraf et al., 2000). This is due to the natural negative slope of the dust number density with increasing grain size. Therefore, a question arises from the precedent results: why is the contribution of big ISD grains more important in the *Helios* data sample? To my opinion, this fact is evidence for the gravitation focusing effect on particles characterized by small β ratios and whose dynamics is consequently ruled mainly by the gravitation forces. As described in Sec. 4.3.5, this effect induces an enhancement of the heliocentric flux of ISD grains closer to the Sun, and in particular behind the Sun. I recall the reader that two competing effects are responsible for this flux enhancement. First, the heliocentric velocity of particles approaching their perihelion on a hyperbolic orbit is higher than their injection velocity. Second, the gravitation focusing is responsible for an enhancement of the dust number spatial density. The resulting flux enhancement factor is given by Eq. 4.17. This factor has been calculated and plotted in Fig. 4.34. Note that the curve shape is not symmetric with respect to the perihelion ($\eta = 0^\circ$) since the enhancement factor value have been calculated in the spacecraft reference frame. It takes therefore into account the motion of the spacecraft relative to the ISD stream. As shown on this plot, an enhancement factor up to 4 can be expected for particles with small β values.

Taking into account the flux enhancement factor one can infer the flux for micron-size grains at infinity, say at the heliopause, immediately after the injection of the ISD grains into the heliosphere. This leads to a flux value for micron-size grains of around $0.65 \cdot 10^{-6}$ m^{2}s^{-1}. This value can be directly compared to the flux value at infinity for 0.3 μm size grains, derived from the *Ulysses* measurements, of about $1 \cdot 10^{-4}$ m^{2}s^{-1}. The implications of this flux value will be further discussed in Sec. 4.3.6.

Another physical mechanism explains the important contribution of big ISD impactors in the *Helios* data set. As seen on Fig. 4.35, the *Helios* orbit lies inside the exclusion zones shaped by the solar radiation pressure. In particular, typical grains with $\beta = 1.1$ as seen by *Ulysses*, are prevented by the radiation pressure to reach the *Helios* spacecraft. As a consequence, only grains with $\beta < 1$ can be detected. Note, however, that the detection of smaller grains ($\beta = 1.1$) was theoretically possible on a very small orbit segment around the perihelion, when the spacecraft crossed the boundary for $\beta = 1.1$. (see Fig. 4.35). Unfortunetly, the ISD identification scheme is insensitive to such grain sizes, as mentioned above, so that this contribution may not have been identified. Furthermore, the 5 years integration time and the natural flux enhancement mechanism compensate for the small spatial density of big ISD grains. Note in addition that the south sensor is mostly sensitive to big ISD grains. Indeed, the trajectories of those grains form a revolution hyperboloid with the Sun as focal point. Thus, particles

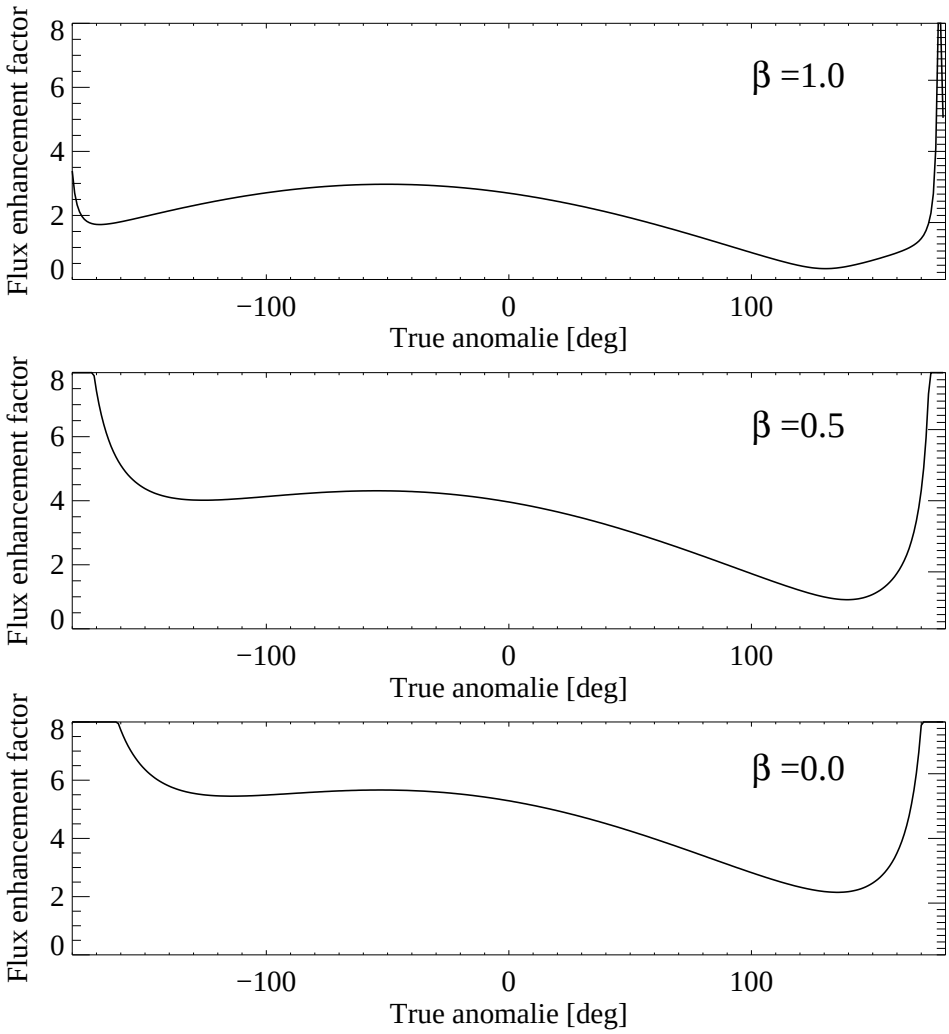

Figure 4.34: Flux enhancement factor due to gravitational focusing as function of the true anomaly, calculated in the spacecraft reference frame. Three β-ratios have been considered. The gravitational focusing effect is stronger for big particles.

injected below the ecliptic plane will be deviated toward the north, and the smaller the β-ratio, the stronger the deviation. Big grains are therefore better detected by the south sensor than ISD grains of smaller masses, for which the field-of-view vanishes.

At least, the analysis of the *Helios* data gives some insights in the rough elemental composition of micrometer-size ISD grains. I provide in Tab. 4.2 some statistics about the TOF mass spectra of the impactors. The analysis and identification of the mass

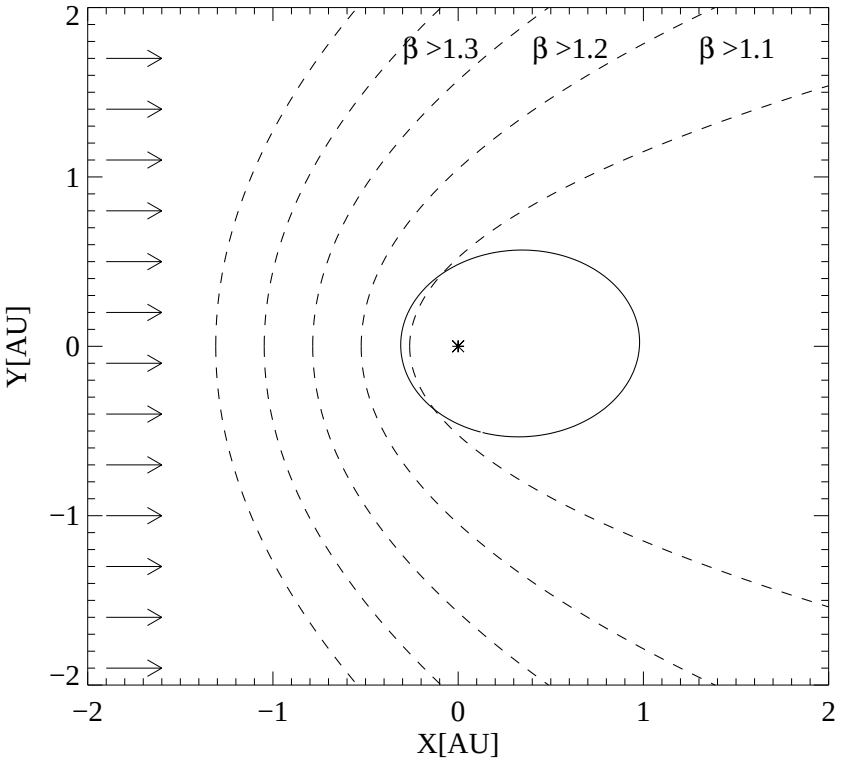

Figure 4.35: Trajectory of the *Helios* spacecraft. The X-axis indicates the injection velocity of the ISD stream. The dashed lines are the boundaries of the exclusion zones corresponding to different β values.

spectra can be found in Grün (1981).

Spectrum type	Ch	Fe	Un	Ch/Fe
ISD	14	5	4	≈3
IDP	74	76	30	≈1

Table 4.2: Statistics of the TOF-spectra for ISD grains and the IDPs.

For both ISD and IDPs, the relative number of *Un* (unidentified) spectra is almost identical, around 16% . It is interesting, however, to compare the relative number of the chondritic (*Ch*) and iron (*Fe*) spectra for the IDP and ISD population. In case of the IDP, a rough balance between the *Ch* and *Fe* mass spectra exists. In contrast, it turns out that the chondritic spectra are more frequent among the ISD grains. The chondritic spectra are more abundant by about a factor 3 compared to the iron spectra. Because of the limited resolution of the TOF spectra, one should be careful with the interpretation of this result, see Sec. 5.4. Nonetheless, the analysis of the *Helios* data gives for the first time ever a direct insight into the elemental composition of ISD.

4.5 Analysis of the ULYSSES data

4.5.1 Introduction

The trajectory of the *Ulysses* spacecraft in the ecliptic plane is almost perpendicular to the direction of the ISD stream Fig. 4.1. This results in a spacecraft velocity relative to the ISD stream for identifying ISD grains with the method described in Sec. 4.1. However, in the dust data obtained by *Ulysses* at high ecliptic latitude, I identified an instrumental effect that can bias the measurements of characteristic values of the ISD stream. In particular, I show in this section evidence for ISD grains that impacted the inner walls of the dust instrument. I re-analyze the entire *Ulysses* interstellar dust data set, taking into account the detector's inner side walls. The side walls have a sensitivity for dust impact detection almost identical to that of the instrument's target area. Thus, I show that the neglect of the sensor side walls overestimates the interstellar dust flux by about 20% and leads to a reduced intrinsic velocity dispersion of the interstellar impactors. Therefore, the width of the stochastic velocity dispersion of ISD grains in the LIC, may be overestimated. The importance of this measurement for understanding the collisional balance of ISD in the LIC (see Sec. 3.2.2) justifies the following analysis.

The flight configuration of the *Ulysses* spacecraft outside the ecliptic plane is favorable for investigate the dynamical properties of the interstellar dust grains, see Fig. 4.37. *Ulysses* is stabilized by its rotation about its main antenna axis, which is directed to the Earth. The dust instrument is mounted on the spacecraft in such a way that its axis is almost perpendicular to the spin axis, see Fig. 4.36. Furthermore, as the orbit plane is almost perpendicular to the downstream direction of the interstellar dust, an ecliptic

latitude scan for positions close to the ecliptic is performed by the instrument boresight due to the spacecraft's rotation. Thus, the pointing of the instrument can be directly described by the rotation angle value of the spacecraft around its spin axis. The mean direction of interstellar particles is located around 90° rotation angle.

The width of the observed distribution is determined by the dependence upon the rotation angle of the instrument's target area available for interstellar impactors. Thus,

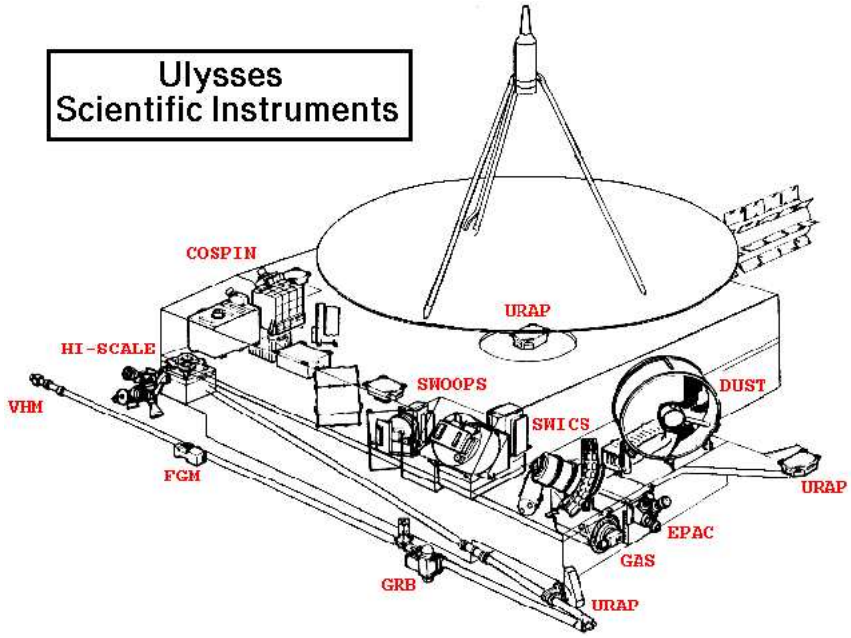

Figure 4.36: Schematic of the *Ulysses* spacecraft and payload, including the dust detector 'DUST'

interstellar impactors can hit the instrument's target even if the impact angle relative to the instrument boresight is non-zero. Assuming a perfectly collimated interstellar dust flux (a Dirac function of the rotation angle), this should result in a width of the rotation angle distribution given by the convolution of the instrument's sensitivity profile and the Dirac peak. Of course, the interstellar dust flux may not be perfectly collimated. In that case, to the dispersion width issued by the spacecraft rotation, we should add the 'natural' dispersion due to the velocity dispersion of individual grains around the velocity vector of the interstellar dust flow. Indeed, the width of the rotation angle distribution was found to be broader than expected in case of a perfectly collimated interstellar dust flux. Under the assumption that the interaction of interstellar dust grains with the heliosphere is not a dominant factor for the velocity dispersion observed between 3 and 5 AU, and assuming a Gaussian spatial distribution profile for the interstellar flow, an upper limit of about 40° to the velocity dispersion width of big grains in the LIC was calculated (Landgraf, 1998). Such findings are of fundamental interest for the understanding of the thermodynamical and dynamical coupling processes between the

interstellar dust grains and the gas in which they are embedded.

However, I show that the broader width in the rotation angle distribution may be caused by impacts striking the inner dust detector's walls. In that case, the velocity dispersion of the interstellar dust grains is overestimated and may lead to wrong conclusions on dynamics of big dust grains in the LIC.

In the next subsection I give some evidences of wall impacts in the Ulysses interstellar dust data sample, before I discuss in Sec. 4.5.3 the implications of this purely instrumental effect on astrophysical conclusions.

4.5.2 Evidence for wall impacts

Recently, intensive experiments have been carried out on a flight spare unit of the *Cassini* dust instrument (Stübig, 2002). In particular, dust particles have been shot on the detector's walls and the resulting impact charge signals monitored. Although the *Cassini* dust instrument and the *Ulysses* one are different, their impact ionisation detector subsystems are almost identical so that the *Cassini* test results can also be applied to the *Ulysses* dust experiment. The tests showed a higher $\frac{QI}{QE}$ ratio for wall impacts than for target impacts, where *QI* and *QE* are respectively the ion charge yield and the electron charge yield. This seems to be caused by a less efficient collection of the electrons generated by the impacts, since the walls are not connected to any charge amplifiers. On the other hand, simulations showed that the electric field in the instrument can still allow the positive ions to reach the ion collector (Grün et al., 2002). As a whole, looking for evidence of wall impacts based on some characteristic features of the impact charge signals may yield the sensitivity of the sensor side walls for dust impacts.

For this work, I use three segments of the *Ulysses* orbit, useful for the identification of interstellar wall impactors as shown on Fig. 4.37. As I want to study an instrumental effect, I have to use a data sample for which the detection conditions were similar for each impactor. Therefore, three conditions have to be fulfilled on each orbit segment. First, the spacecraft's flight geometry relative to the ISD flux has to be similar for each time period. Second, the spacecraft had to be located above or below the ecliptic plane in order to avoid interplanetary dust contamination in the data sample. Third, the theoretical impact velocity of interstellar impactors had to be constant (around 30 kms^{-1} in the chosen flight configuration). Thus, when those conditions are met, the physical conditions of the impact on the detector target are identical for all ISD grains, and a potential instrumental effect may be identified. Three orbit segments between 1993 and 2000 fulfill the required conditions, see Tab. 4.3. Note that the first orbit segment and the third one are identical. The third orbit segment corresponds to the beginning of the second orbit of *Ulysses*.

For each orbit segment, the impact time and rotation angle of the detected impact is

Orbit section [year-doy]	92-300/94-000	96-150/97-250	98-350/00-050
Ecliptic latitude[°]	-11...-41	12...42	-11...-41
Theoretical impact velocity [km/s]	28...32	27...28	28...32

Table 4.3: Orbit sections selected for our analysis. For each orbit segment, I also give the minimum and maximum value of the ecliptic latitude reached by the spacecraft, together with the minimum and maximum theoretical impact velocity values expected for interstellar dust grains.

given in Fig. 4.38. The sensitive area in cm^2 to the ISD stream direction is represented by the contour lines. Note that the calculated sensitive area takes into account the relative velocity of the dust stream to the spacecraft, leading to an effective sensitive area larger than the total geometrical target area of 1000 cm^2. Fig. 4.38 proves that the majority of the impactors detected during the time periods considered are compatible with an interstellar origin. The few impacts detected out of the interstellar sensitivity range may be related to small interplanetary grains able to reach high latitude because of electromagnetic interaction with the ambient magnetic field, carried by the solar wind (Hamilton et al., 1996). Therefore, they will not be considered in our analysis of the interstellar data sample.

I show the distribution of the ISD impacts detected over the three orbit segments as a function of the rotation angle in Fig. 4.39. The distribution for impacts with CLN= 2,3 and CLN= 0,1 (see Sec. 2.2.2) are also shown separately. In the upper panel (all CLN values), the maximum of the distribution is reached for a rotation angle of $\phi_0 \sim 90^\circ$, as expected for ISD impactors.

I assume in a first step that the ISD grains can only hit the instrument's target. In that case, even if the ISD stream is not perfectly collimated, the width of the rotation angle distribution should show no dependence on the impact class. Fig. 4.39 shows that this statistical behaviour is not confirmed. In particular, impacts belonging to the quality class CLN= 0,1 have a broader distribution than the impacts with CLN= 2,3. Taking only the nominal target surface into account and the associated 70 ° half aperture angle, the distribution width for impacts with CLN=2,3 is consistent with a well collimated ISD stream. In contrast, the broader distribution width for impacts with CLN=0,1 can not be explained by such a simplified model.

Fig. 4.40 shows the relative number of impacts in the lower and upper quality classes as function of the rotation angle ϕ.Impacts with CLN= 0,1 dominate the data set if $|\phi - \phi_0| > 45^\circ$. This suggests that the impact quality as defined in Sec. 2.2.2 becomes lower the further the instrument points away from the mean interstellar upstream direction during the particle's impact.When the spacecraft rotation causes the angle between the pointing of the instrument to become greater than the aperture angle, dust particles cannot hit the target anymore but still can hit the instrument's walls, resulting in low-quality class impacts. In contrast, the impact conditions are optimum when the instru-

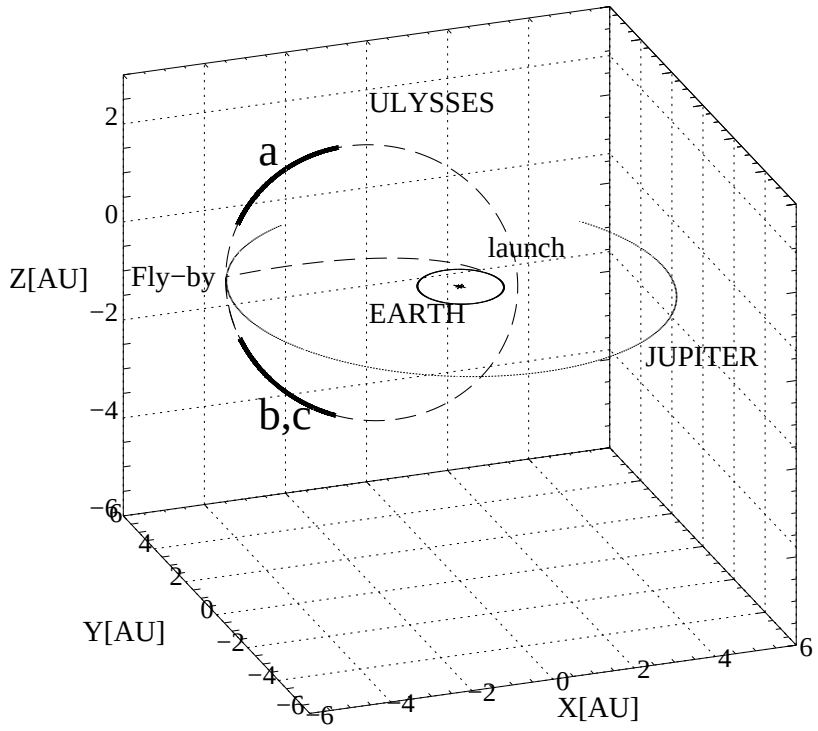

Figure 4.37: Trajectory of the *Ulysses* spacecraft (dashed line) in the heliocentric frame, from launch in 1990 until two orbits have been achieved. The X-axis points toward vernal equinox. The X-Y plane is parallel to the ecliptic plane. The orbits of Earth and Jupiter (thin lines) are also indicated. Note that Jupiter did not achieve one full revolution within the considered time. The inclination reached by the spacecraft after the fly-by at Jupiter is about 80 °. The orientation of the plot has been chosen as seen by an observer co-located with an ISD particle entering the Solar system on a straight trajectory. Note that the plane of the spacecraft's trajectory is almost perpendicular to the downstream ISD direction. Therefore, a rotation angle of the spacecraft equal to 90° corresponds to an instrument's pointing roughly directed toward the observer. The enhanced parts of the trajectory give the orbit's segments a,b, and c where the interstellar data analysed in this work have been collected. The orbit's segment below the ecliptic plane was traversed two times. Segment a: from 1996-150 to 1997-250. Segment b: from 1992-300 to 1994-000. Segment c: from 1998-350 to 2000-050.

ment is pointed roughly toward the ISD flux direction, leading to a dominant number of high-quality class impacts. I conclude that Fig. 4.39 and Fig. 4.40 indicate, at least statistically, the presence of dust impacts onto the detector side walls.

The 'wall impacts hypothesis' is also supported by the following considerations. Let us assume the impacts for which $|\phi - \phi_0| > 45^\circ$ and $\phi < 200^\circ$ to be wall impacts caused by ISD grains. As shown in Fig. 4.41, the sensitivity profile of the instrument calcu-

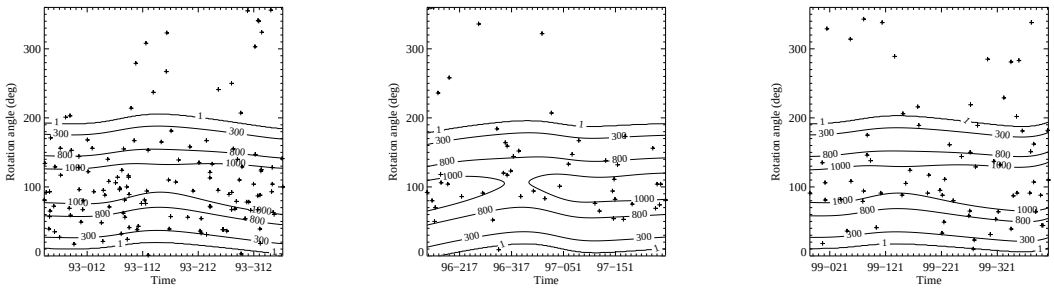

Figure 4.38: Dust impacts of the data sample presented in this work. Each cross represents a dust particle impact. The rotation angle and the impact time are given, together with the geometric sensitivity of the instrument to the interstellar dust stream (cm^2).

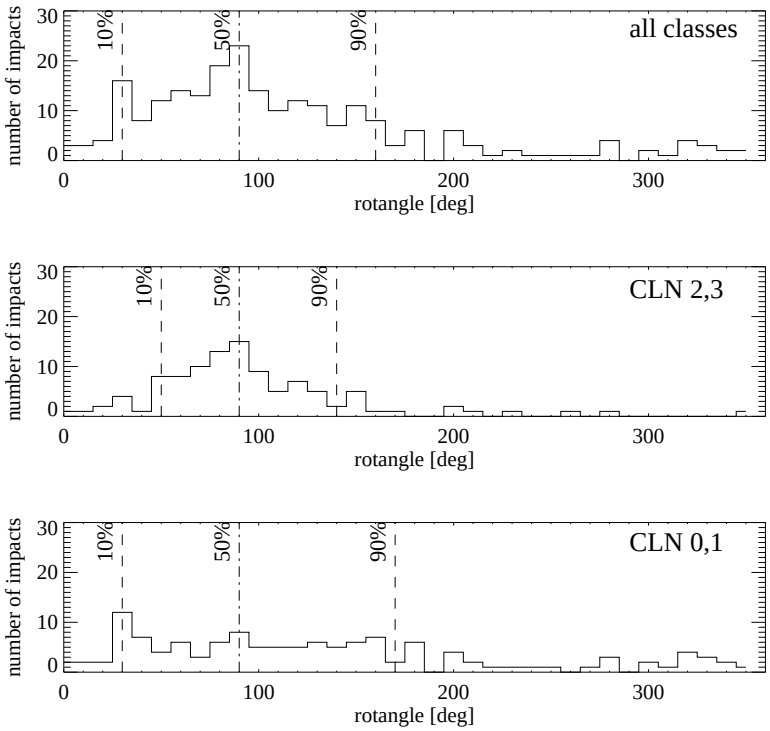

Figure 4.39: Distribution of the rotation angles of the detected dust impacts. The upper plot shows the distribution for all impacts. On the middle one, only impacts with quality classes 2 or 3 were taken into account. In the bottom one is plotted the rotation angle distribution for impacts with quality classes 0 and 1. The range between the dotted lines contains 80% of all interstellar impacts (impactors with rotation angle $\phi < 200°$)

lated for both target (Grün et al., 1992a), and wall surfaces extends the aperture angle

by 20°. Therefore, ISD may be detected up to rotation angles of 200°. Again, the theoretical sensitive surface to a collimated ISD flux was taken into account as a function of time. I performed different calculations, taking into account only the wall surface or the 'traditional' target plus the wall surface. The ratio of the two sensitive surfaces can then be compared with the ratio between the number of wall impact candidates to the total number of impacts recorded over the three orbit parts. Interestingly, it turned out that both ratios are almost equal, around 0.4, which provides additional support for the 'wall impacts hypothesis'. This implies also that the target and the side walls have roughly equal sensitivity for dust detection, at least in the case of ISD grains.

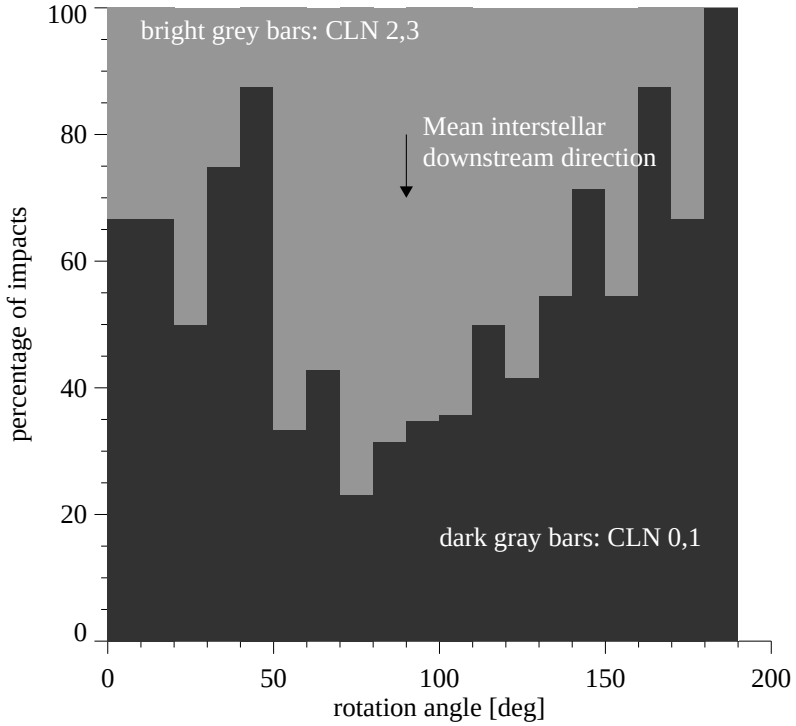

Figure 4.40: Distribution of impacts for which CLN=2,3 compared to impacts with CLN=0,1. The X-axis gives the rotation angle. The arrow gives approximately the rotation angle value $\phi_0 = 90°$ corresponding to the mean interstellar downstream direction. The plot shows that impacts in high quality classes dominate for rotation angles such that $|\phi - \phi_0| < 45°$. Impacts of lower quality are found to be more frequent when the rotation angle corresponds to a pointing further from the mean interstellar downstream direction.

Fig. 4.42 shows the theoretical contribution of the instrument nominal target surface and of the inner wall surface to the distribution of ISD impactors. The curves represent the different sensitive area profiles normalized to the total number of impacts detected over the measurement time. In order to estimate the maximum contribution of the de-

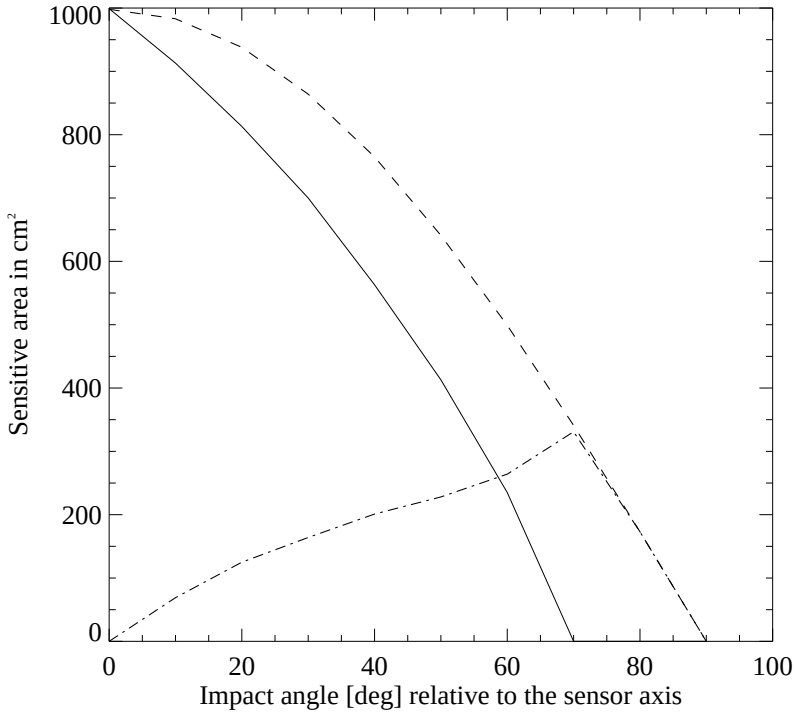

Figure 4.41: Sensitive area of the instrument as function of the angle between the dust impact direction and the pointing (symmetry axis of the detector). The solid line shows the sensitivity of the usual impact target. The dash dotted curve correspond to the wall sensitive surface only, while the dashed one shows the total sensitive surface (target+walls).

tector walls, the ISD flux is assumed to be perfectly collimated. As shown on Fig. 4.42, the contribution of the wall surface seems to provide a good explanation for the impacts located far from ϕ_0. Hence, the walls of the dust detector act as an independent second detector, recording impacts that could normally not be detected by the target, due to its smaller aperture angle. A χ^2 test proves that the sensitivity profile of the instrument including the inner wall leads to a better fit of the ISD distribution than the nominal target area only (see Fig. 4.43).

4.5.3 Discussion

In the previous section, I have shown that the distribution of the events due to ISD impactors is compatible with the result of a convolution of a perfectly collimated ISD flux with a modified sensitivity profile of the dust instrument, taking into account the side walls of the detector. On the opposite, the observed data distribution can also be obtained using the usual target detector only, assuming in that case a non-perfectly col-

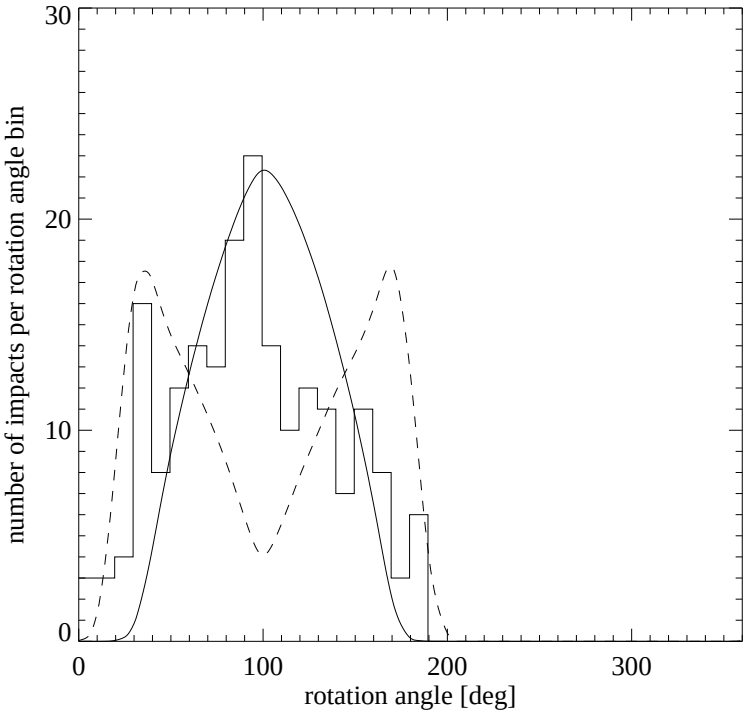

Figure 4.42: The histogram shows the distribution of the interstellar impactors as function of the rotation angle, all quality classes included. The theoretical distribution curves are also plotted, taking into account the sensitive area of the walls only (dashed line) or of the sensitive area of the target only (full line).

limated ISD flux. The latter approach provides a large width in the velocity distribution that can only result from the ISD grains dynamics in the LIC, (see Sec. 4.5.1). However, as I have found evidences for wall impactors in the data set, I claim that neglect of the wall impact effect, responsible for a bigger aperture angle of the detector, has led in earlier analysis to an overestimation of the dispersion by about 30%.

Note that the identification of wall impacts in this work was statistically possible because of the detection geometry with respect to the ISD stream. Our identification also required the CLN parameter (impact class), involving complex criteria onto the impact charge signals. To better connect the identification of wall impactors in our ISD data set with laboratory experiments, I tried to find criteria based on electrical values that can be easily measured. In particular, the rise times and the amplitudes of the ion charge signals can be compared independent of the impact class. I separated the data sample into the impacts for which $|\phi - \phi_0| > 45^\circ$ (and $\phi < 200^\circ$) and the impacts for which $|\phi - \phi_0| < 45^\circ$. A detailed analysis of the rise times and amplitudes of the electron and ion channels was performed but no statistically strong enough differences were found for a reliable one-to-one identification of wall impacts. However, a trend

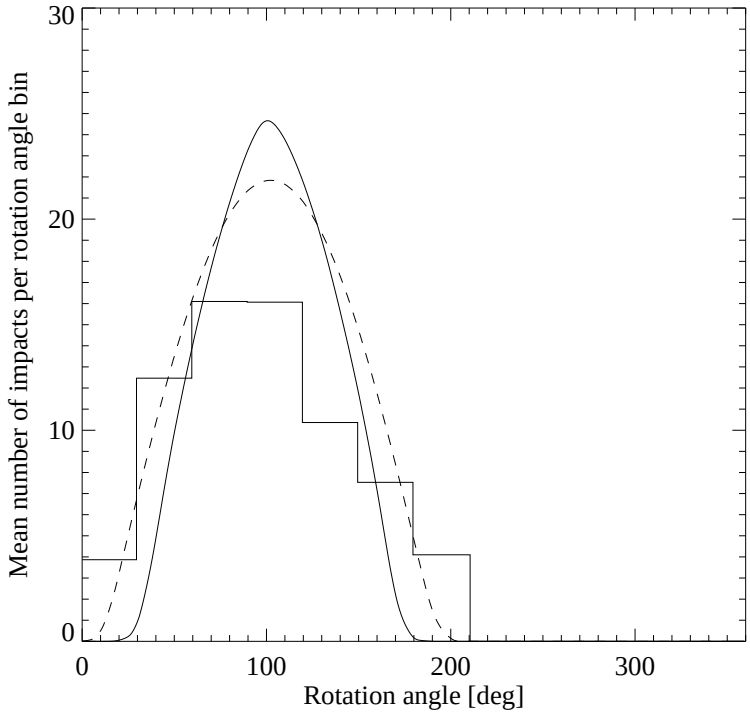

Figure 4.43: Distribution of rotation angles for the ISD contribution. The theoretical distribution given by the target sensitive area (solid curve) or the sensitive area including the walls is plotted (dashed line). A χ^2 fit is performed between the data distribution and each of the two sensitive area models. In the first case, the test gives $\chi^2 = 12.6$, with $P(\chi^2 > 12.6) = 8\%$, while in the second case $\chi^2 = 5.51$, with $P(\chi^2 > 5.51) = 59\%$. As a result, the sensitive area model including the walls better accounts for the data distribution.

in the behaviour of the electron channel seems to reflect a difference between impacts on the target and wall impacts. Indeed, impacts corresponding to rotation angles far away from the peak of the distribution seem to generate less electron charge, as can be seen in Fig. 4.44. Taking the three measurement periods together, about 70% of those impacts generated low electron impact charges (below 10^{-12} C). In contrast, only 40% of the impacts recorded with a pointing closer to the interstellar downstream direction ($|\phi - \phi_0| < 45°$) are located in the lower charge amplitude range. These results are in agreement with the laboratory tests mentioned in Sec. 4.5.2 and with a personal communication of Hakan Swedhem, analysing the *Gorid* data.

The finding that wall impacts contribute significantly to the ISD data set lead us to caution also the flux calculations, since more instrument's surface is available for impacts. In order to quantify this effect on the determined ISD flux values, I calculated for the three orbit segments the corresponding fluxes, using the usual target area or the

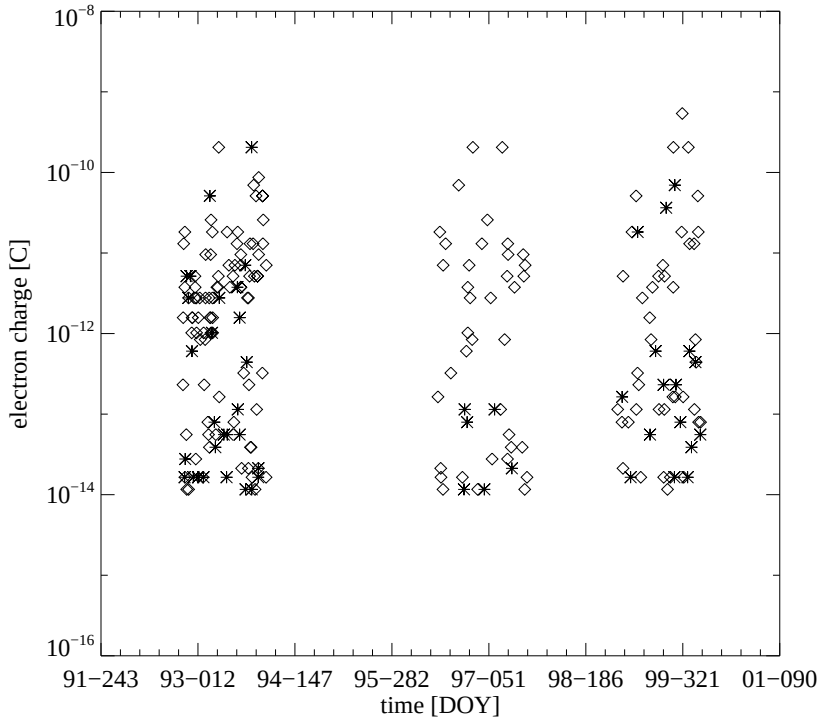

Figure 4.44: This plot gives the electron charge distribution of the impacts in the rotation angle range [0°,200°] for the three orbit sections studied. The diamonds represent impacts with $|\phi - \phi_0| < 45°$ and asterisks the impacts with $|\phi - \phi_0| > 45°$.

target plus the wall area. The results are summarized in the Tab. 4.4. Flux calculations ignoring the side walls overestimate the ISD flux by about 20%.

Note that the instrumental effect discussed in this work is likely to affect the measurements performed by the *Galileo* spacecraft, carrying a twin instrument of the *Ulysses* dust detector. Analysis of the sensor characteristics using the Jovian dust stream population were already performed by Krüger (1999). However, in the *Galileo* case, wall impacts are very difficult to detect for the following reasons. To test statistically the target sensitivity, one needs a population for which the detection conditions (impact energy, geometry) are well known and kept nearly constant over a period of time providing significant statistics. The ISD stream detected by *Ulysses* allows this analysis. In contrast, the *Galileo* data set consists of different dust populations, whose mass and impact velocity differ by orders of magnitude (i.e Jovian dust stream (Grün et al., 1998) or dust rings population (Krivov et al., 2002).) Furthermore, the detection geometry varied much depending on the measured population. Thus, wall impactors are likely to contribute to the *Galileo* data set but can not be identified statistically as performed in this work. However, I confirm that wall impactors will contaminate dominantly the low impact classes (CLN=0,1).

I showed that the wall impact hypothesis is supported by the *Ulysses* ISD data. This instrumental effect points out the limitations of the *Ulysses* instrument in measuring the dynamics of the ISD stream. In particular, the velocity dispersion of the ISD grains detected in the heliosphere can not be measured accurately. As mentioned in the introduction, the ISD data set from the *Ulysses* spacecraft consists mostly of 'big' interstellar grains, i.e. grains larger than those needed to explain the interstellar extinction curve. Those grains, discovered ten years ago, are quite new in our picture of the local interstellar medium. It has been suggested that big interstellar grains may convey most of the dust mass from their circumstellar sources to the ISM (Frisch et al., 1999). Collisions and shock waves may then lead to the creation of the smaller classical grains observed by astronomers. Due to their size, big grains may couple dynamically to the ambient gas on much longer distance than the smaller ones. Therefore, they may keep the dynamics associated to their injection in the LIC, resulting in a higher velocity dispersion than caused by the thermal motion. As the effect of the heliospheric crossing onto the ISD grains dynamics may be corrected, in-situ measurements of the ISD stream intrinsic dynamics are possible. There is therefore a strong need for new detection techniques able to resolve the intrinsic velocity dispersion of the ISD stream. With the new generation of dust instruments, like those proposed in the Cosmic Dune mission (Grün et al., 2000), arises the exciting perspective of a detailed investigation of matter transport in the ISM.

Orbit section	92/300 to 94/000	96/150 to 97/250	98/350 to 00/050
Flux[$m^{-2}s^{-1}$] (nominal target)	$1.1{\cdot}10^{-4}$	$4.1{\cdot}10^{-5}$	$4.8\cdot10^{-5}$
Flux[$m^{-2}s^{-1}$] (plus wall)	$8.6{\cdot}10^{-5}$	$3.2{\cdot}10^{-5}$	$4.1\cdot10^{-5}$

Table 4.4: ISD flux values calculated with the nominal target sensitivity profile or the nominal target plus the wall surface. In the first case, rotation angle between 30° and 160° are admitted. In the second case due to the extended sensitivity profile, rotation angle between 0° and 200° have been taken into account.

5 Discussion and Conclusions

In this chapter, I present a summary of the results that I obtained throughout the analysis of the data in Sec. 4. Then, the implications and consequences of those results are discussed under the light of different fields of the astrophysics.

5.1 Detection of ISD from 0.3 to 3 AU

The primary goal of this work was to estimate the contribution of ISD to dust data sets obtained by various spacecrafts in the inner solar system. As mentioned in the introduction, one could only guess what happens to the ISD grains identified by *Ulysses* beyond 3 AU when they penetrate deeper into the solar system. Therefore, the main result of this thesis is the confirmation of the ISD penetration down to 0.3 AU. Possible detection of ISD at Earth orbit distance was already reported in (Svedhem et al., 1996). This work was based on the *Hiten* satellite data, which was on a highly eccentric orbit about the Earth. The results presented in this thesis therefore confirm this analysis. However, the various locations reached by the different spacecrafts used for this work allowed a real monitoring of the ISD stream around 1 AU.

In this thesis, the detection of ISD grains at Earth orbit distance was first achieved with the recent *Cassini* dust data. The data analysis, using a method to discriminate ISD from IDPs, showed that about the half of the data sample could be explained by ISD impactors with $\beta \approx 1$. The inferred ISD flux was somewhat lower than the flux detected by the *Ulysses* spacecraft (see Sec. 4.2.4). Therefore, filtration processes such as radiation pressure was suspected to alterate the ISD stream when it penetrates closer to the Sun.

A more detailed investigation of the radiation pressure filtering could be performed through the analysis of the *Galileo* data. Indeed, the orbit segments favorable for the detection of ISD covered a wide range of heliocentric distances and heliocentric longitude. As a result, ISD flux determination at various spacecraft locations confirmed the boundary position of the exclusion zones for ISD grains. As the boundary equations were found analytically, assuming a theoretical β-ratio curve (see Fig. 3.1) which reflects the radiation pressure efficiency for a given model of dust grain, the ISD measurements are in agreement with the hypothesis supporting this model. Furthermore, the *Galileo* ISD data pointed out a possible focusing effect, increasing the detection probability of big ISD grains in the Sun vicinity see (Sec. 4.3.6).

However, only the *Helios* data obtained between 0.3 and 1 AU could provide unambiguous evidences of this focusing effect. The spacecraft benefited of a long integration time (a few years) and of a favorable orbit for the detection of big ISD grain. Furthermore, the ISD spatial density was increased through gravitation focusing and the impact rate of big ISD was higher due to their high velocity relative to the spacecraft. These detection conditions resulted in a significant contribution of micron-size ISD grain in the *Helios* data set (see Sec. 4.4.4). The determined flux value in the mass range [10^{-15} kg,10^{-14} kg], corrected by the gravitation focusing factor, leads to the spatial mass density of such large grains at the heliopause, immediately after their injection from the LIC into the heliosphere.

5.2 Interstellar dust: an experimental object

A first interesting conclusion of the in-situ detection of ISD grains is that they can be considered as a laboratory object, helping to test some hypothesis on the instruments behavior under utilisation conditions that can not be reproduced on Earth. In particular, the calibration facility at the Heidelberger dust accelerator does not allow experiments with particles with sizes and velocities comparable with those encountered by the different spacecrafts on the orbit segments used for this work.

Some theoretical considerations in impact plasma physics suggested that the determination of the impact parameters should be rather based on the ion charge signal and avoid the rise time method (see Sec. 2.4). However, this was only a 'work hypothesis' whose consistency had to be verified in the light of the data analysis. Actually, the data sets of *Helios*, *Cassini* and *Galileo* showed evidences for the suspected non-nominal behavior of the instruments in the case of high energetic impactors. Indeed, the analysis of the *Helios* data suggested that the velocity and mass estimation of high energetic impactors based on both the ion and electron channels is biased. Furthermore, as shown in Sec. 4.2.3, the rise time method failed to provide meaningful estimates for the ISD impactors on the *Cassini* instrument target. The better statistics of the *Galileo* data confirmed this picture, showing a systematic underestimation of the impact velocity for ISD impactors and an overestimation of the impactor mass (see Fig. 4.21). As a whole, the analysis of the ISD data sets taken by 3 different detectors, and based solely on the ion charge signal has led to coherent interpretations of the respective data sets. I believe this fact to be an indirect proof of the validity of the preliminary assumptions on the instrument behavior made in Sec. 2.4.

However, this new insight into the instrument behavior does not conflict with the valuable *Ulysses* measurements of the ISD stream velocity and mass distribution. As shown in Fig. 4.37, the *Ulysses* orbit is almost perpendicular to the ISD stream direction. The resulting low impact velocities imply low impact energies, still corresponding to the calibrated range of the instrument. Promising experiment setups are currently

developed to simulate impacts of high energetic particles by laser shots. Those experiments might provide the theoretical background necessary to explain the non-nominal response of the dust instruments to energetic ISD impacts.

5.3 The heliosphere: a cosmic mass spectrometer

The analysis of the *Ulysses* data suggested at first that the heliosphere may act as a huge mass spectrometer filtering the ISD stream (Landgraf, 1998; Landgraf et al., 2000). The results presented in this thesis strongly support this picture.

Ten years separate the ISD measurements by *Cassini* and *Galileo* at 1 AU. This time period corresponds to half a period of the solar activity cycle. One could therefore hope to identify in the *Cassini* and *Galileo* ISD data a time variable ISD flux component, due to the time variable IMF (see Sec. 3.2.2). However, in contrast to the *Ulysses* trajectory, the orbits of the missions *Cassini*, *Galileo* and *Helios* in the inner solar system were not favorable to provide new estimates about the electromagnetic filtering mechanism. Indeed, as shown in (Landgraf et al., 2003), only small grains (radii below 0.2 μ m) experience strong trajectory perturbations due to the electromagnetic coupling and are removed from the ISD stream before they can reach the inner solar system. Therefore, only the *Ulysses* spacecraft located between 3 AU and 5 AU could provide evidences for those particles. The charge-to-mass ratio value of $\frac{q}{m} = 0.59\ \mathrm{C{\cdot}kg^{-1}}$ for 'typical' ISD grain (size range [0.3 μm,0.4μm], $\beta \approx 1.1$, (Landgraf et al., 2003)) implies a gyro-radius greater than 3000 AU. As a whole, no significant difference of the ISD flux values due to electromagnetic coupling should be seen at 1 AU for those particles. In that sense, the flux values of $2.5 \pm 0.5 \cdot 10^{-5}\ \mathrm{m^{-2}\ s^{-1}}$ and $2 \pm 1 \cdot 10^{-5}\ \mathrm{m^{-2}\ s^{-1}}$ inferred at 1 AU for particles with $\beta \approx 1$ from, respectively, the *Cassini* and *Galileo* measurements, are consistent with the expectations.

As the ISD data presented in this thesis were obtained at points within the ISD exclusion zones (see Fig. 5.1), a study of the radiation pressure filtering as function of the heliocentric distance was possible. The ISD flux measured by the *Ulysses*, *Cassini*, *Galileo*, and *Helios* spacecraft are plotted as function of the heliocentric distance in Fig. 5.2. The *Ulysses* flux has been taken from (Landgraf, 1998). In addition, I plotted the mean value of the ISD flux registered achieved by *Galileo* between 0.7 AU and 2.5 AU. As shown in Fig. 5.2, the ISD flux decreases with decreasing solar distance. From the Jovian orbit distance of 5 AU down to the Venus orbit distance of 0.7 AU, the ISD flux is reduced by about a factor of 10. I am confident that this effect is due to the radiation pressure filtering, simulated for individual grain trajectories in Fig. 3.2. The size distribution function for ISD grains inside the heliosphere as inferred from the *Ulysses* ISD data and from the *Galileo* ISD data beyond 3 AU, shows a negative

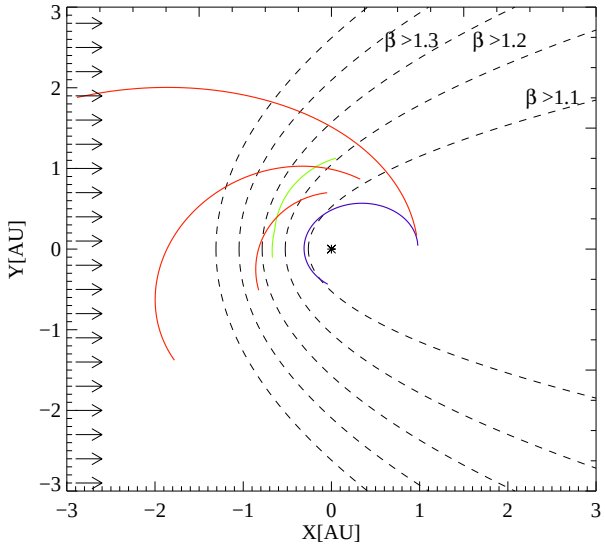

Figure 5.1: This plot shows the different orbit segments of the *Galileo* (red line), *Cassini* (green line), *Helios* (blue line) where ISD grains could be identified. In addition, the dotted lines shows the exclusion zones of ISD for different β-ratio values. The X axis is parallel to the ISD flux.

slope (Landgraf et al., 2000). This implies that the spatial density of big grains (small β values) is lower than those of small grains (high β values). The radiation pressure removes gradually ISD grains from the ISD stream, while penetrating the inner solar system. The smaller grains whose exclusion zones are more remote from the Sun (see Fig. 3.3), are removed first. Thus, the radiation pressure removes preferently the most abundant component from the ISD stream, what reduces the observable component of the ISD flux in the vicinity of the Sun.

The ISD flux measured by *Helios* is, however, by a factor 10 smaller than the extrapolation of the flux between 1 and 5 AU would suggest. In my sense, this can be explained by the *Helios* trajectory, which lied almost completely inside the exclusion zone for grains with $\beta = 1.1$, (see Fig. 5.1). As a consequence, the main component of the ISD stream, known to consist of particles with $\beta \approx 1.1$, (see (Landgraf et al., 2003)), is completely removed by the radiation pressure before it can reach the *Helios* orbit. Bigger particles ($\beta < 1$), however, can still be detected at very small heliocentric distances. Furthermore, their flux is increased by gravitation focusing (see Sec. 4.4.4). Thus, *Helios* benefits from the 'mass spectrometer effect': small grains are removed and big grains concentrated at the spacecraft location, so that the *Helios* ISD data set consists mainly of big interstellar grains.

Estimates of the ISD spatial density around 1 AU are crucial for modeling the dust

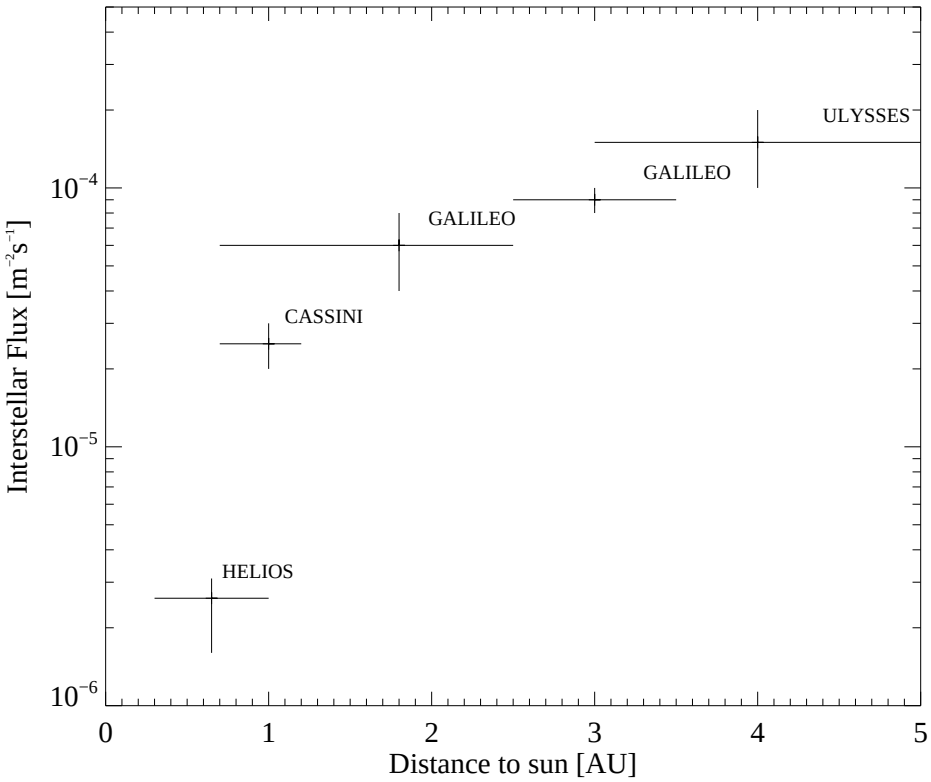

Figure 5.2: Synthetic plot showing the values of the ISD flux calculated with the data presented in this thesis. Note that I plotted the mean of the flux values obtained with the *Galileo* data on the most inner segment 1,2 and 3a.

environment in the Earth vicinity. Theoretical models are either based on in-situ or remote observations and interpretations of dust data. The various dust size ranges are covered by different detection methods, mainly by radar meteor survey, by zodiacal light measurements or by dust instruments on-board spacecrafts. Except for *Cassini*, my thesis is based on the re-interpretation of dust data which were at least partially integrated into dust models, like those by Staubach (Staubach et al., 1997; Staubach et al., 2001) or by Dikarev (Dikarev et al., 2002). Such models have both a practical and a fundamental goal. On the one hand, they are used to evaluate the risk due to dust impacts for spacecraft missions. On the other hand, they provide a synthetic view of the interplanetary micrometeorites environment. The most recent model by Dikarev even describes the dynamic evolution of the dust complex. However, the 'interstellar module' of both models is based on oversimplified assumptions, leading to biased quantitative estimations. Indeed, in (Staubach et al., 2001), a constant ISD flux at 1 AU of $1.5 \cdot 10^{-4}$ $m^{-2}s^{-1}$ is assumed, about an order of magnitude higher than the flux observed by *Cassini* or *Galileo* at the same heliocentric distance. Although this problem

is not really relevant for practical application (the 'typical' ISD is too small to cause serious damage to a spacecraft), an improvement of model predictions about the ISD population at 1 AU should include the effects due to filtering and focusing on the ISD flux values measured by *Ulysses*, *Helios*, *Galileo* and *Cassini*. However, it is important to stress here that my findings about the mass-dependent ISD flux does not require to change the global picture of the IDPs as predicted by the models. Indeed, when the instruments were sensitive to both ISD and IDP populations, the ISD contribution never exceeded 30 % of the whole data sample.

From the ISD flux measurements around 1 AU the dust number density can be derived. This quantity plays a crucial role for the optical identification of ISD in the Solar System. Indeed, like IDPs, ISD grains contribute to the zodiacal light through sun light scattering (visible wavelength) or thermal emission (in the infrared). The geometric cross sectional area Γ is defined by

$$\Gamma = n_d * C_{eff}, \tag{5.1}$$

where n_d is the dust number density and C_{eff} the effective cross section for a given interaction. Γ may be thought as the total sectional area per unit volume. The dust number density n_d can be derived by measuring directly the geometric cross sectional area Γ by various methods implying either photon-dust or energetic particles-dust interactions. In contrast, dust in-situ measurements give a direct estimate of n_d, from which Γ can be inferred. From micro-craters and in-situ measurements a Γ value for the interplanetary dust component of $4.6{\cdot}10^{-21}\mathrm{cm}^{-1}$ was derived (Grün, 2000).

If one use the ISD flux as measured by *Cassini* and *Galileo* around 1 AU and the flux values of bigger grains at 1 AU inferred from the *Helios* measurements, the number density for ISD is approximately of $1.15{\cdot}10^{-9}$ m^{-3} (particles radii of ≈ 0.4 μm). Assuming $C_{eff} = \pi r^2$ averaged over the solar spectrum (oversimplified model!), one gets $\Gamma_{ISD} \approx 5.7{\cdot}10^{-24}$ cm^{-1} to be the total ISD geometric cross section at 1 AU. The geometric cross sectional area of ISD at 1 AU hence amounts to about 0.1% of that derived for the entire zodiacal cloud. This value is lower by one order of magnitude than previously estimated in (Mann, 1995). This difference results from the higher ISD flux assumed in the latter work, taken from the *Ulysses* measurements between 3 and 5 AU. Note that Γ_{ISD}, if measured in Earth orbit, should show saisonal variations, depending on the Earth location relative to the Sun and the ISD downstream direction.

5.4 ISD material properties

In Sec. 3.2.2, I assumed that the shape of both, the ISD grains and IDPs to be spherical, compact and made mostly of silicates. Starting from this hypothesis, I used the corresponding radiation pressure-to-gravitation ratio $\beta(m)$ as shown in Fig. 3.1. However, the effective cross section depends on the dust grain morphology, as well as on its material composition. The crucial role of the β ratio for the data analysis needs therefore

a discussion about the limitations and implications of the employed radiation pressure model.

The radiation pressure model is based on two basic parameters: the grain cross section, depending on the wavelength and the grain's geometrical structure. The calculation of the $\beta(m_d)$ function also needs the grain mass (see Eq. 3.9), function of the grain porosity. (The porosity gives the volume fraction of a grain filled with vacuum). Fractal or compact shapes may therefore lead to different $\beta(m_d)$ function and thus, to different grain dynamics. Furthermore, the grain elemental composition of the grain may also play a crucial role, depending on the albedo and the density of the material.

One could therefore wonder why I used *a-priori* the same β-ratio function for both the IDPs and the ISD population, (see Sec. 3.1). Indeed, ISD grains and IDPs, or even different IDP populations, may differ by their elemental composition and shape. However, as I will show in the following, there are some reasons to believe that the compact spherical silicates model is a reasonable 'work' hypothesis, not only for the most common IDPs, but also for the ISD grains likely to be found in the solar system. The next paragraphs consist in a justification of this simplified model. In addition to the ISD, I consider three basic types of interplanetary dust grains: asteroidal particles, young cometary particles, and old cometary particles. Note that all grains, IDPs as well as ISD grains, are assumed to have an electrostatic equilibrium potential of +5V in interplanetary space (Horányi, 1996).

Asteroidal particles As debris of larger bodies, assuming a zero porosity for the asteroidal particles seems reasonable. Indeed, these particles originate from fragmentation due to mutual collisions between parent bodies. Since this is a very energetic process, fragile particles do not survive, in contrast to their more compact components. Furthermore, collection of meteoroids in the upper atmosphere or in deep see sediments (Brownlee, 1985) showed evidences of more or less compact spherules of silicates with a variable amount of metal oxide inclusions.

Young and old cometary particles From observations of Halley's comet, freshly injected sub-micrometer size grains have been identified. Models for those grains have been proposed by Greenberg (1990). In general, they are highly porous and made of a silicate core with an absorbing organic mantle. Such grains are therefore quite different from the silicates compact spherules model. However, those young cometary grains are more likely to be removed by the radiation pressure from the solar system immediately after their injection. Indeed, their low density increases their β-ratio value and they are injected essentially at the perihelion of the comets, where the heliocentric velocity is at highest. Therefore, they are not likely to remain on bound orbits. In particular, Tab. 5.1 shows that for the typical grain assumed (radius of 0.3 μm), no 'young' cometary particle can be found on bound orbit since $\beta > 1$. Furthermore, according to (Fechtig, 1989),

even if cometary dust grains are injected on bound orbits, they loose their organic mantle during their lifetime, due to solar UV radiation. Hence, only the silicate cores, also called 'Old cometary dust grains', finally survive. The silicate cores are assumed to have a lower porosity and β-ratio similar to those of 'Asteroidal' grains Tab. 5.1.

radius[μm]	Asteroidal	Young cometary	Old cometary
0.03	0.163	0.901	0.135
0.1	0.751	1.790	0.701
0.32	0.772	1.213	0.700
1	0.222	0.543	0.251
3.2	0.061	0.261	0.0882

Table 5.1: Theoretical β-ratio values for four particle models, as given in (Wilck and Mann, 1996).

ISD grains properties ISD grains models given in the literature are useful to predict what kind of elemental composition is expected for the dust grains in the interstellar medium, and thus, inside the heliosphere. The ISD grain models are based on the observation of the extinction curves and of the elemental depletions in the interstellar medium. The last mentioned method provide indirect indication about the ISD elemental composition. Indeed, heavy elements embedded in dust grains are sputtered away by supernovae shocks and injected into the ISM (Jenkins, 1987). A famous model is the so-called 'unified model of interstellar dust' by Li and Greenberg (1997). The authors propose a trimodal dust model: large silicate core-organic refractory mantle, very small carbonaceous particles and Polycyclic Aromatic Hydrocarbons (PAHs). Of course, PAHs are rather big molecule than dust grains and cannot be detected with the in-situ methods as described in this thesis. Very small carbon grains are also very unlikely to penetrate deeply into the solar system: because of their high q/m ratio they are strongly coupled to the IMF. In this model, even grains in the upper size range are smaller than the grains detected by *Ulysses*, *Cassini*, *Galileo* and *Helios*. Therefore, a reasonable assumption was to propose the ISD grains detected in-situ as a possible source (by mutual collisions) for the larger component of the 'unified model' (Grün and Landgraf, 1997). This implies a similar elemental composition for the ISD grains detected in-situ, based on carbon and 'astronomical silicates', whose optical properties are inferred from astronomical observations.

Meaningful estimates of the particles morphology are, however, not easy. Homogeneous silicates spheres can be produced by condensation in the outflow from cool giant stars or nucleation growth in cold dense molecular clouds. In contrast, aggregates with fractal structure may develop from dust-dust collisions, when the colliding particles have approximately the same size (see Fig. 5.3, right plot). Note that an additional mantle made of carbon-ice can condense out of nebula gases (Greenberg, 1988) and be

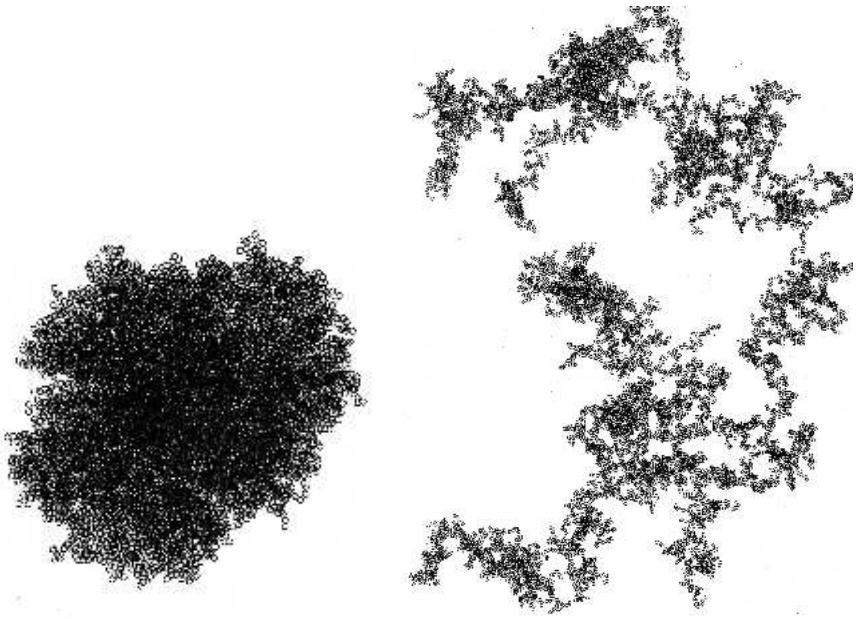

Figure 5.3: ISD grain shape simulation: on the left, a compact particle cluster aggregate of spherical constituent particles. All constituent particles have the same radius. On the right, a fractal-type aggregate, with the same number of constituent particles. Those pictures have been taken from (Mukai et al., 1992)

further processed into an organic layer by UV radiations. This mantle results in a more compact shape for the dust grain. Computer simulated collisions of small spheres with a bigger aggregate result in the shape shown in Sec. 5.3, left plot. However, such shapes may not exist for the size range of the ISD discussed here, since favorable conditions ruling their formation are not provided in the interstellar medium (Kempf, private communication).

As a whole, the homogeneous silicates sphere model should not be a to bad approximation for the estimation of the radiation pressure acting on IDPs. A large uncertainty remains, however, for the ISD grains. In what follows I will show how the ISD data presented in this thesis may help to solve the mystery around material properties of ISD found in the inner solar system.

Implications of the ISD data From the ISD stream monitoring between 0.3 AU and 2.5 AU, one can derive indications about the material properties of the detected ISD grains. One can formulate the question as follows: 'Which kind of morphology and which elemental composition is compatible with a deep penetration of ISD grains into the solar system?'.

A way to answer this question is to justify the validity of the $\beta(m)$ function assumed

in Sec. 3.1, based on the optical properties of spherical astronomical silicates. First, I showed that for a given β and the associated impact velocity, the ion charge yields measured by the *Cassini*, *Galileo* and *Helios* dust instrument are consistent with the mass value given by the $\beta(m)$ function. Second, recall that both, the radiation pressure filtering effect and gravitation focusing are parameterized by the β-ratio. As the presented measurements cover a large heliocentric and ecliptic longitude range, it was possible to show that the position of the β-dependent exclusion-zones boundaries are well reflected in the ISD data. At least, the qualitative and quantitative agreement of the detected number of big ISD grains with the predictions by the gravitation focusing model (see Sec. 4.4.4) provides further evidence for the validity of the $\beta(m)$ function used in this work. As a whole, the $\beta(m)$ function gives a coherent picture of the expected alteration of the ISD stream in the inner solar system. This is an evidence that the 'sphere of silicates' model for the ISD grains, leading to the $\beta(m)$ function as used in this work, is valid for estimating the dynamical evolution of the ISD stream within the heliosphere. Note, however, that the $\beta(m)$ curve depends on so many parameters that nothing more about the individual grain morphology can be deduced from this result. In contrast, some interesting indications about the elemental composition of the ISD grains can be deduced: as the maximum of the $\beta(m)$ curve is strongly dependent on the elemental composition (Wilck and Mann, 1996), the $\beta(m)$ function used for my analysis suggest a dominant contribution of silicates in the detected ISD grains. This conclusion is also supported by the excess of chondritic material found with the *Helios* instrument (see Sec. 4.4.4). Of course, the amount of carbonaceous material can not be estimated directly. However, it should not be dominant, since this would modify strongly the β-ratio function and thus, the dynamics of the grains.

The $\frac{q}{m}$ ratio measured for the ISD grains in the heliosphere between 3 AU and 5 AU is about 0.59 Ckg^{-1} (Landgraf et al., 2003). As the typical grain mass is $\approx 3{\cdot}10^{-16}$ kg, the charge-to-mass ratio implies a charge number N_e of about 1100. Note that this number is in very good agreement with the theoretical considerations given in (Horányi, 1996) for spherical grains. However, as the charging efficiency of fractal shapes is not known, one can not conclude which one of the shapes shown in Fig. 5.3 is the most likely for the ISD grains detected. Indeed, the number of charges N_e that can coexist on a dust grain at a given equilibrium potential is ruled, in part, by the coulomb repulsion and defines the electrical capacity of the particle. Calculations of the capacity of a fractal aggregate could therefore lead to a better understanding of the measured $\frac{q}{m}$ ratio.

5.5 ISD spatial mass density

This section deals with the determination of the spatial mass density of the ISD derived from the ISD flux as observed by *Cassini*, *Galileo* and *Helios*. From the mass density measured in-situ, important conclusions about the dust component at the heliopause can be drawn. Note that in what follows, the particles are assumed to be silicate sphere

with density $\rho = 2500$ kgm^{-3}.

Of fundamental interest are the determination of the dust-to-gas mass ratio and the ISD grain size distribution. As in Sec. 5.4, the grain size distribution is inferred from dust grain models which reproduce the interstellar extinction curve, while the dust-to-gas mass ratio is derived from depletion measurements of elements in the gas phase. However, the size distribution of the biggest ISD grains cannot be derived by astronomical measurements. Furthermore, the measurements of elemental depletion show strong variations depending on the line-of-sigth and on the considered elemental abundance. As they also require absorption lines with a suffisant optical thickness, the derived elemental depletion values are often averaged over large interstellar distances (Frisch et al., 1999).

The in-situ determination of the ISD flux in the inner solar system provide a valuable complement to the methods mentioned above. Both, the dust-to-gas mass ratio and the big ISD grain size distribution can be derived at the heliopause. Indeed, from the ISD flux F for a given grain mass range determined at a given heliocentric location, the flux value F_0 at the heliopause can be inferred by taking into account the alteration processes of the ISD stream in the heliosphere. (For the ISD grains detected in the inner solar system, recall that only the radiation pressure and the gravitation focusing are relevant.) Assuming a constant injection velocity of v_0=26 kms^{-1}, the mass density within a mass interval dm is given by

$$dn_m = \frac{F_0}{v_0} dm \tag{5.2}$$

Assuming furthermore a typical gas density $n_H \approx 0.1...0.3$ cm^{-3}, the dust-to-gas mass ratio can be found straight forwardly.

The *Ulysses* monitoring of the ISD stream over a long period allowed highly reliable data analysis, in contrast to the measurements presented in this thesis. However, it is interesting to check the consistency of the additional results obtained with *Helios*, *Galileo* and *Cassini*, especially for the 'big' ISD grains. Fig. 5.4 shows the differential distribution per logarithmic mass interval. The three straight lines give the MRN distribution introduced in Sec. 3.2.2, for different n_H values. The dark data points show the *Ulysses* measurements as taken from (Landgraf, 1998), while the green, red, and blue one represent the *Cassini*, *Galileo* and *Helios* measurements, respectively. The *Ulysses* data reflect the filtering of the small grains component of the MRN distribution due to the heliospheric interface (Linde and Gombosi, 2000) and to the electromagnetic coupling with the IMF (Grün et al., 1994). Note that the *Helios* flux has been corrected for the gravitation focusing enhancement factor (see Fig. 4.34).

In Fig. 5.4 the dust mass density derived from the *Cassini* data and from the *Galileo* data for $\beta \approx 1$ ($m_d \approx 3 \cdot 10^{-16}$ kg) are in very good agreement with the *Ulysses* results. This is also the case for the smaller grains detected by *Galileo*. The dust mass density,

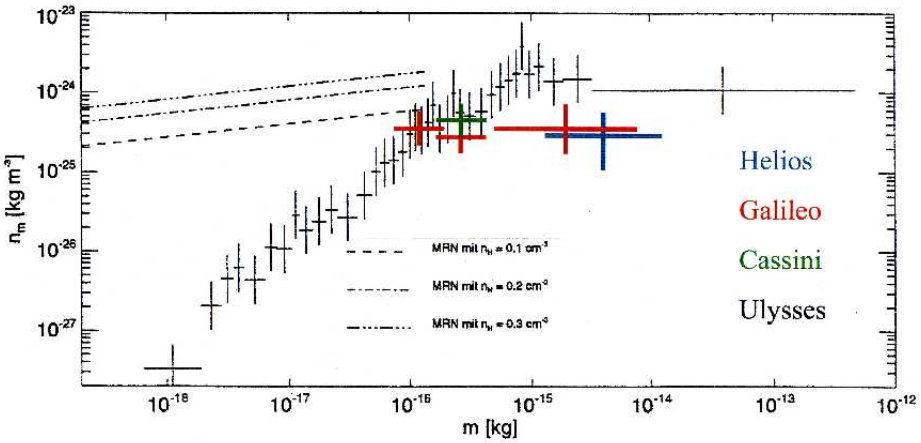

Figure 5.4: dust mass spatial density, as function of the logarithmic grain mass. The results obtained with the *Ulysses*, *Helios*, *Galileo*, *Cassini* ISD data are plotted, together with the MRN distribution for three values of the hydrogen atomic density.(plot modified from (Landgraf, 1998))

however, shows a deviation for the bigger grains detected by *Helios* and *Galileo*. While the *Galileo* measurements of big grains suffer from a poor statistic, the *Helios* results are more reliable due to the enhanced impact rate caused by the gravitation focusing effect (see Sec. 4.4.4). Explanations for a different mass density of big grains are not obvious. As twenty years separate the *Ulysses* and the *Helios* measurements, one could imagine that an inhomogeneity in the LIC, at a typical scale of at least 100 AU (distance traveled in 20 years by the Sun within the LIC) may cause the deviation. This scenario, however, is very unlikely. Indeed, the formation of an inhomogeneity in the LIC dust component is described by the time scale τ_c needed by dust grains to couple dynamically with the surrounding gas. τ_c can be estimated by the equation

$$\tau_c = \frac{m_d}{\pi {r_d}^2 \rho_g v_g}, \tag{5.3}$$

where m_d is the mass of the dust grains, r_d the grain radius, ρ_g the gas mass density and v_g the thermal velocity of the gas. Therefore, τ_c can be envisioned as the time needed by the dust particle to collide with a gas mass equal to its own mass. Calculations show that $\tau_c \approx 10^6$ y in the LIC, so that inhomogeneity is not believed to explain the different flux determined by *Helios* and *Ulysses*. Despite of this deviation (of less than one order of magnitude), however, the *Helios* results confirm the existence of much bigger grains than the upper MRN mass cut, and their large contribution to the dust mass density. For a review on the implications of the discovery of large ISD grains in the LIC, please refer to (Grün and Landgraf, 1997; Frisch et al., 1999; Kimura et al., 1999).

5.6 Accretion of cosmogenic material on Earth

Evidences of cosmogenic material on Earth have been found within the last decades by many geological studies. Anomalous iridium deposits have been identified and interpreted as residues of a huge meteorite impact, assumed to be responsible for the mass extinction at the end of the Cretaceous and the Tertiary periods (Alvarez et al., 1980; Kyte, 1988). Other elements like ^{10}Be found in arctic ice cores or ^{60}Fe deposits in deep sea sediments have also an extraterrestrial origin: while ^{10}Be can be formed through spallation reactions of nitrogen or oxygen atoms in the upper atmosphere, ^{60}Fe is mainly produced in supernovae. Furthermore, there is no doubt that cosmic dust is a source for those cosmogenic elements. IDPs have been identified unambiguously on Earth (Brownlee, 1985) and very big ISD grains (radius above 40 μm) entering the atmosphere could also be monitored through radar meteor survey (Baggaley, 2000). Influences of such accretion processes on the chemical composition of planetary surfaces or atmospheres have been discussed in (Flynn, 1991; McNeil et al., 1996; Yabushita and Allen, 1989). However, few works tried to estimate the systematic contribution of ISD as an interstellar matter source on Earth, although this question may be of fundamental interest in the frame of the prebiotic life theories (Greenberg, 1997). I present in the following a rough estimate of the ISD mass flux value accreted on Earth.

Fig. 5.5 shows the Earth orbit together with the ISD stream (+X direction). Note that for the calculation of the Earth's position over one year, ephemerides data for the year 1999 have been used. The ISD exclusion zones are indicated as well. The plot shows that the ISD flux on Earth will have seasonal variations, depending on the Earth position relative to the Sun and the ISD stream. In June, the Earth is located 'in front' of the sun, so that small grains (β-ratio values up to 1.3) can reach the planet. From October to February, however, only grains whose dynamics is dominated by gravitation (big grains) can be accreted onto the Earth, while the smaller grains ($\beta > 1$) are completely removed by the radiation pressure. In addition, between November and January, the accretion of big grain will be enhanced through the gravitation focusing effect (Sec. 4.4.4).

Using the ISD spatial mass density shown in Fig. 5.4, I calculated the ISD mass accretion rate (averaged over one month) onto the Earth throughout one year (see Fig. 5.6). For each β-ratio value range likely to reach the Earth, the impact velocity has been calculated. Furthermore, the spatial density correction factor, (Eq. 4.17) has been taken into account. The results are shown between July 1999 to July 2000. Note that the electromagnetic coupling of the smaller grains (high β values) with the IMF was neglected. However, this should not affect much the curve shape since ISD grains that couple with the IMF are removed by electromagnetic interactions before they can reach the Earth orbit. The enhanced accretion rate between November and January is caused by gravitation focusing of big ISD grains. During this period of time, the Earth is located around the 'focal point', behind the Sun (see Fig. 5.5).

The Sun is currently heading toward the LIC boundary (Frisch et al., 1999). As-

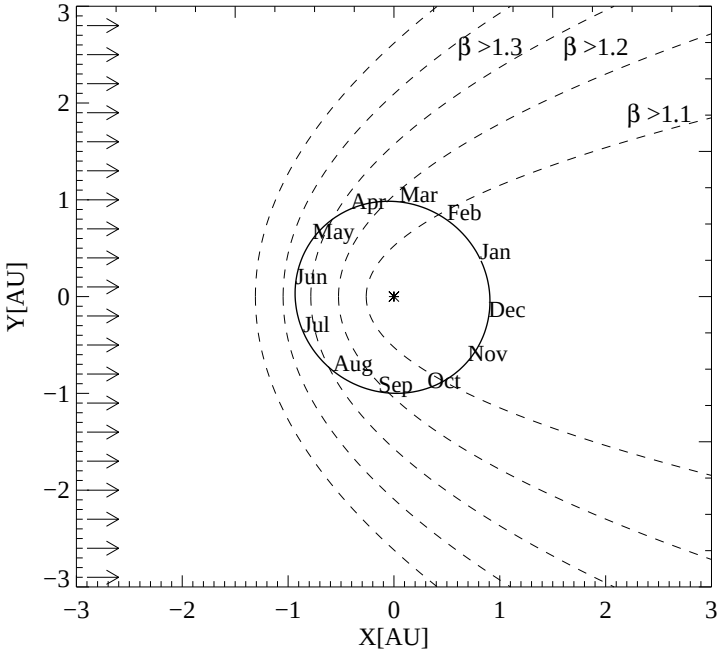

Figure 5.5: ISD stream and Earth trajectory. Real Earth ephemeride data for the year 1999 have been used. The position of the Earth over the whole year is given by the months names.

suming the LIC to have a diameter between 2 and 5 parsecs, the solar system has been embedded up to 100 millions of years in this sub-component of the interstellar medium. The mass flux density function plotted in Fig. 5.6 can be used to estimate quantitatively the long time scale accretion of ISD under following hypothesis:

1. The large scale dust component in the LIC is homogeneous
2. The radiation pressure of the Sun was constant over the last 100 millions years

The first hypothesis is not obvious, since the spatial dust distribution within the LIC might be perturbed locally, e.g. by supernovae shock waves. However, as no astronomical observations can provide a detailed description of this distribution (especially in case of the big grains), I assumed the spatial grain density at the heliopause derived from the in-situ measurements to be representative for the last 100 millions years. In contrast, the second hypothesis is more reasonable since the Sun spent the last 4 billions years of her life on the main sequence of the HR-diagram. Therefore, the radiation pressure, responsible for ISD filtering must have been quite constant over this time.

The ISD mass flux F_m averaged over one year is given by

$$F_m = \frac{\int f_m(t)dt}{\int dt}, \tag{5.4}$$

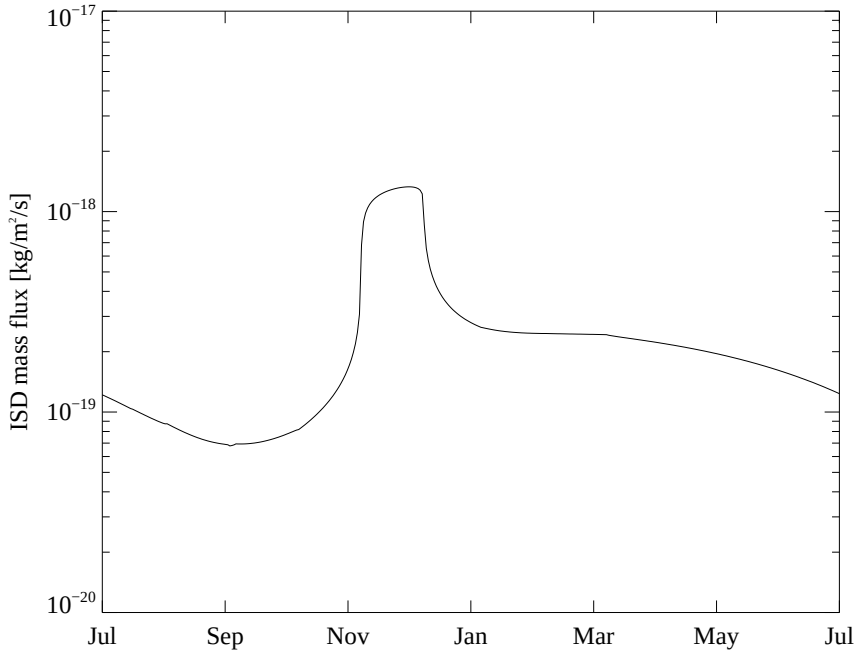

Figure 5.6: ISD mass accretion rate (averaged over one month) onto the Earth throughout one year.

this gives $F_m = 2.7{\cdot}10^{-19}$ kgs^{-1}m^{-2}, or in 'geological' units, F_m =85gcm^{-2}Ma^{-1}. Note, that this value is a lower limit since the influx of very big ISD grains can not be measured accurately with the in-situ detection technique. (The small target area of the dust instrument results in a poor statistic for big grains, whose spatial number density is low). Although the F_m value seems to be rather small, geological analysis of sediments or polar ices sample should be sensitive enough to detect such quantities: for comparison, the iridium estimates are of the order of 1 ngcm^{-2}Ma^{-1} (Kyte, 1988)! The main problem remains, that is the discrimination between interstellar and interplanetary matter. However, carefully isotopic analysis, as described in (Marvin, 1987), should make it possible.

5.7 Going further

The main goal of this thesis was an analysis of recent or older in-situ dust data taken in the inner solar system. The armada of milestone missions carrying dust instruments provided a large amount of excellent data on which I could base the present work. More than a complement to remote observation methods the in-situ detection is essential to the study of the interaction between the Solar System and the surrounding

dust-gas phase in which it is embedded. Furthermore, a detailed monitoring of the ISD fluctuations in the vicinity of the terrestrial planets is highly desirable for planetology sciences. This monitoring can be achieved with a sufficient accuracy only by in-situ detection methods.

The major difficulty of the data analysis was the discrimination of the ISD grains from various interplanetary populations. In general, the identification had to be constrained to specific orbit parts and needed further assumptions suggested by the results of the *Ulysses* mission. However, I showed that the body of evidences for ISD in the inner Solar System leads to a coherent interpretation of the ISD stream alteration within the heliosphere. This suggests that both, our understanding of the heliospheric filtering processes and the modeling of some ISD grains material properties is close to the reality. Thus, the research on interstellar dust is ready for the ultimate step: infer the dynamics of the ISD grains in the LIC and find out their precise chemical and isotopic composition. This is the goal of the new dust instrument, a 'dust telescope', currently in development.

The primary task of this instrument will be the reliable identification of ISD grains. To avoid large uncertainties on the measurement of the orbital elements, this instrument will have a trajectory sensor, capable to resolve the impact velocity vector within 1° accuracy (Grün et al., 2003). Such a precision will avoid the ISD measurements to be biased by instrumental effects as those discussed in Sec. 4.5. In addition to the trajectory subsystem, a time-of-flight mass spectrometer will have a mass resolution of $\frac{M}{\Delta M} \approx 100$. This should be sufficient to verify some guesses about the dust grain composition as discussed in Sec. 5.4.

One of the crucial parameter for the success of this mission is the choice of the spacecraft orbit. As shown in this thesis, a low cost orbit in the Earth vicinity (not further than the L2 Lagrange point distance) and within the ecliptic plane is suitable for monitoring the ISD stream. With the precision of the next instrument generation, and the knowledge on the ISD stream dynamics from the heliopause down to the Earth, the observer will be able to reconstruct the individual dust grains trajectories up to their injection in the heliosphere. Thus, the dust astronomer will contemplate the Local Interstellar Cloud at home...

A Some calculations around the ISD stream in the inner Solar system

In this appendix, I present details of some calculations needed for the data analysis. In particular, the interpretations of the data sets used in this thesis was based in part on theoretical expectations for the ISD dynamics.

A.1 Polar equation of the β-exclusion zones boundary

Assume an ISD particle, whose size is defined by its β ratio value. I assume that the particle is injected inside the heliosphere parallel to the $+X$ direction with a given injection velocity v_∞ greater than the escape velocity of the solar gravitation field. If G is the gravitation constant and M the Sun mass, $\tilde{\mu} = GM(1-\beta)$ is the effective gravitation parameter, reduced by the solar radiation pressure. I assume in this section $\beta > 1$ and $Y_\infty = b$ is called the impact parameter of the trajectory. The eccentricity e and the deviation angle δ of the hyperbolic trajectory are given by, respectively

$$e^2 - 1 = \frac{b^2 v_\infty^4}{\tilde{\mu}^2} \tag{A.1}$$

$$\sin\frac{\delta}{2} = \frac{1}{e} \tag{A.2}$$

If (r, f) are the polar coordinates associated to a Cartesian position (X,Y), the polar equation of the hyperbola is given by:

$$r = \frac{p}{1 + e\cos(f - \frac{\delta}{2} + \frac{\pi}{2})}, \tag{A.3}$$

where $p = \frac{b^2 v_\infty^2}{\tilde{\mu}}$.

Let us now assume a position given by (r_s, f_s). This position can be reached by an ISD grain if the condition

$$r_s = \frac{p}{1 + e\cos(f_s - \frac{\delta}{2} + \frac{\pi}{2})} \tag{A.4}$$

is fulfilled. This is equivalent to solve for the b value the equation

$$\frac{b^2 v_\infty^2}{\tilde{\mu}} = r_s(1+\sin^2 f_s \frac{b v_\infty}{\tilde{\mu}} - \cos f_s) \tag{A.5}$$

Therefore b is solution of the binomial equation

$$X^2 - X r_s sin f_s - r_s \frac{\tilde{\mu}}{v_\infty^2}(1-\cos f_s) = 0 \tag{A.6}$$

The discriminant is $\Delta = r_s[r_s \sin^2 f_s + 4\frac{\tilde{\mu}}{v_\infty^2}(1-\cos f_s)]$. A solution to Eq. A.6 exists only if $r_s > -4\frac{\tilde{\mu}}{v_\infty^2}\frac{1-\cos f_s}{\sin^2 f_s}$, where the right part of the inequation can be further formed in $-4\frac{\tilde{\mu}}{v_\infty^2}\frac{1}{1+\cos f_s}$

As a consequence, the limit case $\Delta = 0$ gives the polar equation of the exclusion zone, parameterized by β

$$r_s = -4\frac{\mu(1-\beta)}{v_\infty^2}\frac{1}{1+\cos f_s}, \tag{A.7}$$

which is the polar equation of a parabola. Note that no assumption has been made concerning the plane that contains the trajectory of the dust grain. The same calculation can be performed in each plane spanned by the vectors ($\mathbf{r}_\infty$, $\mathbf{v}_\infty$), where $\mathbf{r}_\infty$ is the dust grain position at the heliopause. Fig. A.1 shows a simulation of the trajectories for grains starting at different positions. Note the paraboloidal shape issued by the radiation pressure. The Sun is located at the origin.

A.2 Interception trajectory

The method described here provides an efficient way to solve the following problem: given the position of a spacecraft (X_s,Y_s), can I find ISD grains able to reach the spacecraft? If yes, what are the orbital parameters of their trajectories? What is their velocity vector at the spacecraft position? How much charge will generate the impact?

The first question can be immediately answered considering Eq. A.6. The sign of the discriminant depends only on the product $\tilde{\mu}(1.-\cos f_s)$. As $\tilde{\mu} = (1-\beta)\mu$, if $\beta > 1$, the problem does not have a solution for all spacecraft locations. As shown in the previous section a solution exists in this case if, and only if, the spacecraft is located outside the exclusion zone associated to the β-ratio value. For $\beta = 1$, the solution is trivial and unique: $Y = Y_s$ is the trajectory that hits the spacecraft. For $\beta < 1$, there are always two solutions, provided by two values b of the impact parameter with opposite sign.

$$b_{1,2} = \frac{r_s \sin f_s}{2}[1 \pm (1 + \frac{4\tilde{\mu}}{v_\infty^2 r_s(1+cos f_s)})^{\frac{1}{2}}], \tag{A.8}$$

In any case, I have chosen the interception trajectory defined by the impact parameter having the same sign than Y_s (shorter trajectory). The orbital parameters are calculated

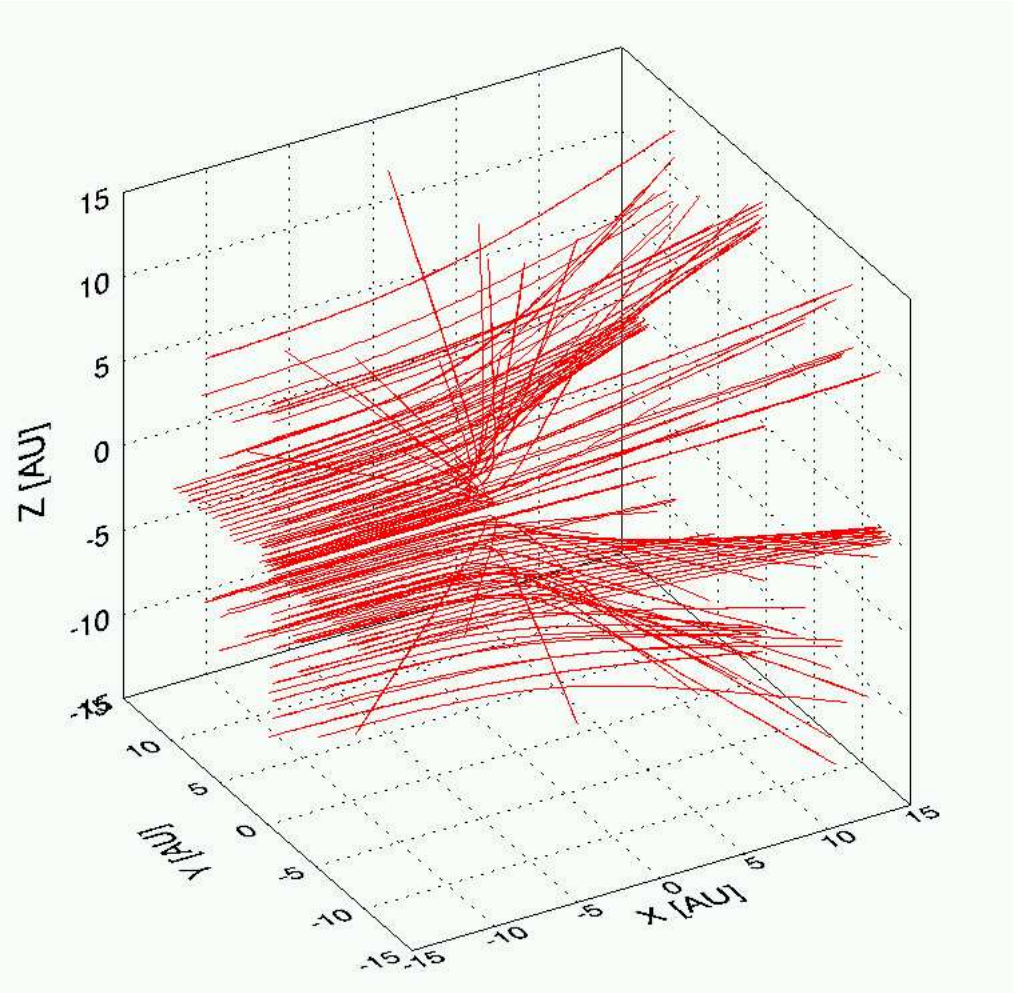

Figure A.1: This plot shows a 3D view of a ISD stream component undergoing strong radiation pressure forces. For the simulation, the injection velocity is 26 kms^{-1} and the β-ratio equal to 1.8.

using Eq. A.1 and Eq. A.2, and the velocity vector of the dust grain at any location of the trajectory is deduced.

An example of application for the *Helios* spacecraft is shown in Fig. A.2. The hyperbolic trajectory of an ISD grains for which $\beta = 0.5$, hitting the spacecraft, is plotted (dotted line). The velocity vectors of the dust grains and the spacecraft in the heliocentric frame are symbolized by the arrows. Then, it is straightforward to calculate the velocity of the dust grain in the spacecraft reference frame. Finally, from the function $\beta(m)$ (see Fig. 3.1) and from the instrument calibration law, the impact charge can be deduced.

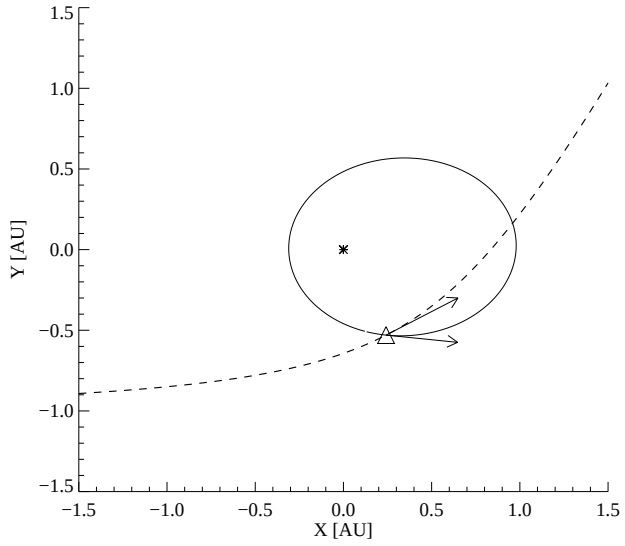

Figure A.2: Interception trajectory of an ISD grain with $\beta = 0.5$, hitting the *Helios* spacecraft. The arrows show the velocity vectors in the heliocentric frame of both the spacecraft and the ISD grain.

B CASSINI Data description

The CDA instrument allows the transmission of the digitalized impact charge signals. Each channel is sampled continuously at low frequency (0.375 MHz). An event detection (dust impact or noise) cycle is initiated according to a detection scheme implemented in the instrument's software. The event detection is based on cross conditions that have to be fulfilled by electrical potentials overcoming a certain threshold. For a detailed description, please refer (Srama, 2000b). When an event detection cycle is initiated, the channels monitoring the impact charges are sampled at a higher frequency (6 Mhz for the ion channel QI and 3 Mhz for the electron channel QE). 496 samples of the signals are recorded. This provides 80 μs and 160 μs, respectively, of charge signal. In addition, 16 signal values recorded just before the event detection are reread and stored. An example of the resulting impact charge signals is given in Fig. B.1. The charge signals corresponding to the IID subsystem are QT and QI. Note that the plotted event corresponds to a real impact, detected as the spacecraft was in the inner solar system and for which a mass spectrum is also provided (MP channel). As mentioned in Sec. 4.2 the QP channel was saturated in the inner solar system and is therefore not plotted.

In contrast to the *Helios*, *Ulysses* and *Galileo* dust instruments, the CDA offers the big advantage to transmit the full impact charge signals. This allows a better evaluation of each event, since the shape of the signals obtained in space can be compared directly with signals produced in the laboratory during the instrument calibration. Furthermore, signals artefacts can be identified and corrected, so that the determination of the signal rise time and signal amplitude is more accurate. The next paragraph deals with the criteria that the charge signals of an event have to fulfill to account for a genuine dust impact. Then, I briefly describe how signals generated by high energetic impactors have to be corrected.

B.1 Noise identification

During the measurement period presented in this thesis, the CDA detected and transmitted events (both, impact or noise events) with digitalized charge signals. Although I used exclusively the ion charge signal for the estimation of the impact energy, the presence of both an ion signal (QI) and an electron signal (QT or QC) is necessary to discriminate a genuine impactor from a dust event. The basic principle of this discrimination is not new and has already been discussed for the previous impact ionisation dust instruments (Baguhl et al., 1993). Consequently, all events showing only one impact

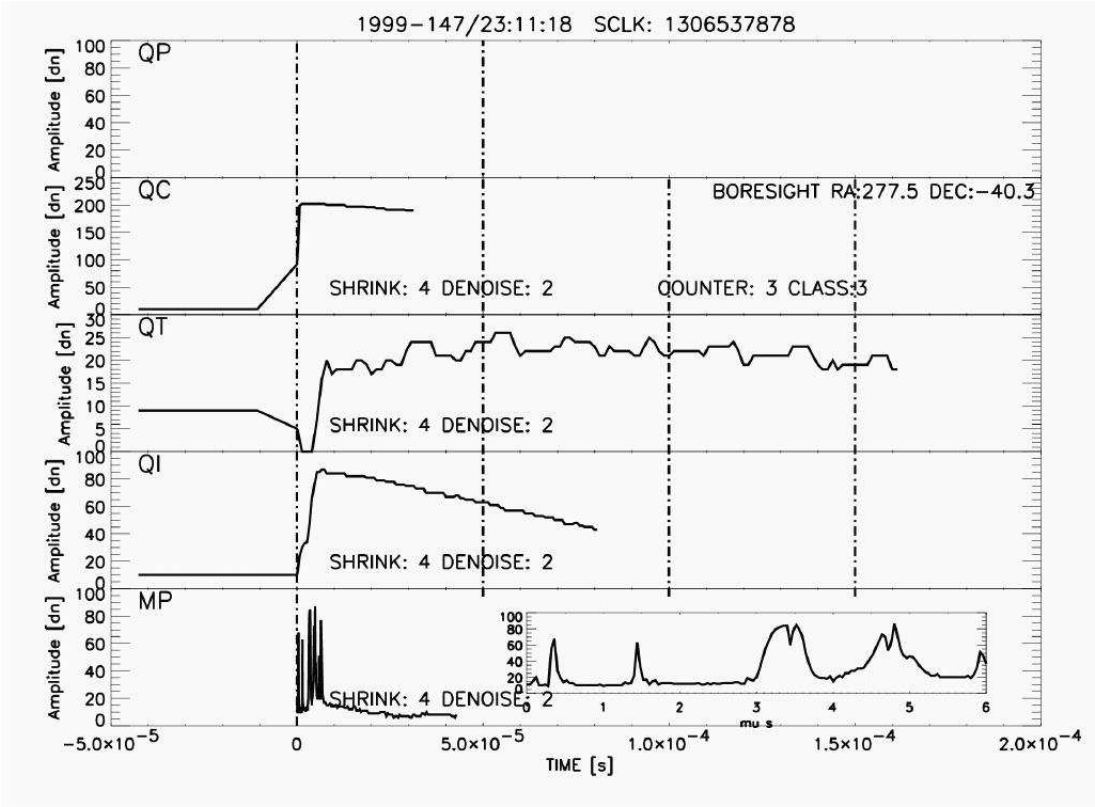

Figure B.1: charge signals corresponding to an event detected by the dust instrument and transmitted by *Cassini* to the Earth.

charge signal have been discarded. Also, signals whose shape was to different from the nominal one observed during calibration tests were rejected.

A detailed study of one noise category was performed, in order to understand its origin. So-called 'QI-flares' were found to be present in the data set. Those events are characterized by the fact that only the ion channel triggered and initiated an event detection cycle. This behavior is definitely not compatible with the physics of a dust impact. I tried to identify the noise source, testing various hypothesis. Fig. B.2 shows the rate of the 'QI-flares' events between 1999 and end 2001.

Although UV radiations were identified as a major noise source on the ion channel during the *Galileo* mission (Grün et al., 1995a), this hypothesis is unlikely in the *Cassini* case for two reasons. First, the ion amplifier is better shielded by the instrument walls, (see Sec. 2.2). Second, in contrast to the *Ulysses* and *Galileo* spacecraft, *Cassini* is three axis stabilized and the instrument boresight was always kept away from the Sun direction.

The hypothesis of solar flares as noise source was also envisioned. This explanation is supported by the bursts in the 'QI-flares' rate curve (see Sec. B.2), that could

be issued by high energetic particles heating the ion amplifier. Indeed, in contrast to the UV radiations that expands radially from the Sun, the particles of the solar wind plasma are coupled with the IMF, whose field lines are described by the Parker spiral (see Sec. 3.1). Therefore, depending on the angle between the instrument pointing and the local IMF vector field, high energetic particles are likely to hit the ion amplifier. I tried to find a correlation between the 'QI-flares' and major solar flares as detected by the Space Weather NOAA Forecasts. I calculated a rough estimated propagation time of the high energetic particles from the Sun to the spacecraft. Unfortunately, no significant correlation was found during the *Cassini* cruise in the inner solar system. Furthermore, as recent data show that the 'QI-flares' frequency did not decrease with an increasing heliospheric distance (expected because of a dilution effect of the solar wind), this hypothesis was abandoned.

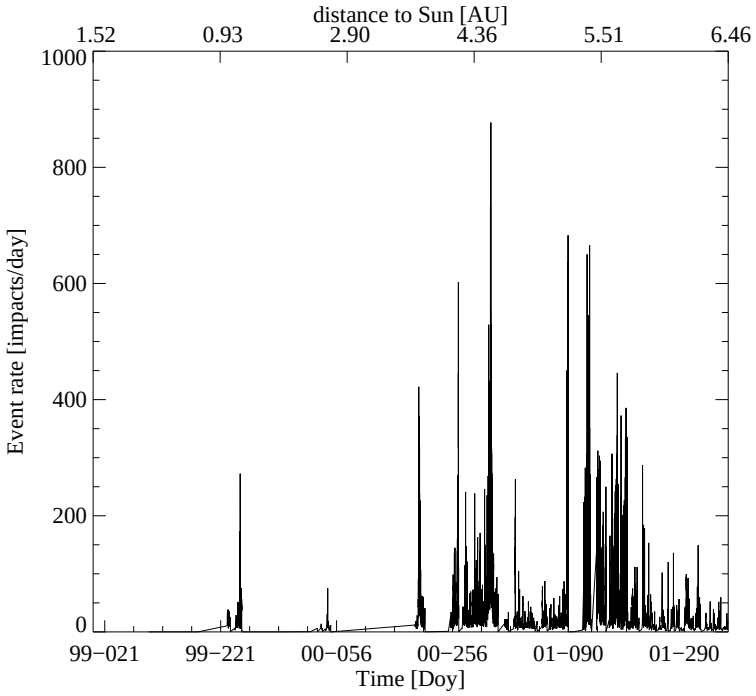

Figure B.2: Rate of the 'QI-flares' events transmitted by the CDA during the cruise of *Cassini* from 1999-001 to 2001-365.

At least, various possible influences of the hardware environment onto the CDA was studied. The two principal hypothesis on which I focused were:

- The articulation procedure of the turn table that may trigger the ion channel
- The spacecraft attitude control thrusters that may inject some gas residues into the CDA

Also for those hypothesis, no significant evidences were found. So far, no satisfying explanation have been found.

Despite of this chess in understanding the 'QI-flares' noise source, those signals could be easily rejected from the studied data set. The following identification criterion was used for the data analysis: $QI > 5 \cdot 10^{-15}$ C and $QI > QT$ and $QI > QC$, where QI, QT, QC represent the amplitude of the signals.

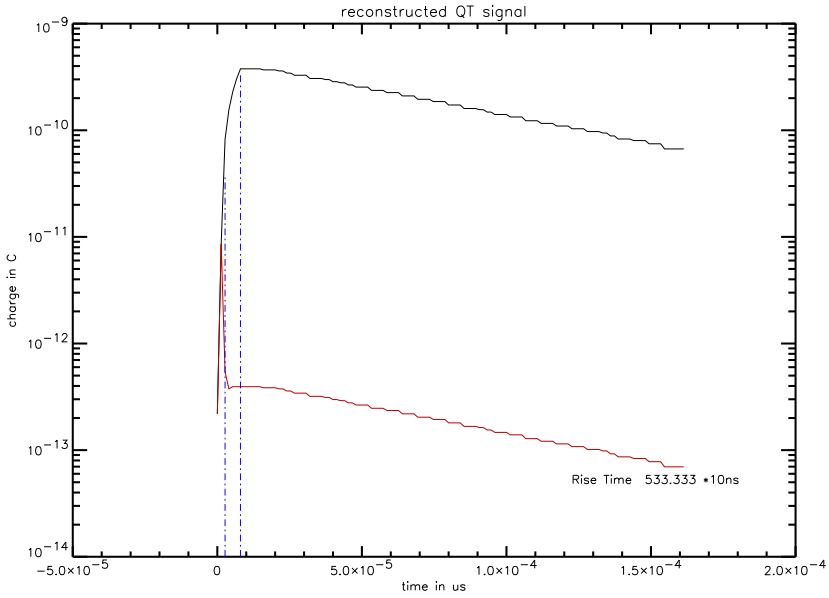

Figure B.3: This plot shows an example of the reconstruction of a switched QT signal. The red line gives the original signal, while the dark line represent the signal after reconstruction. The vertical dashed blue lines indicate the rise-time, defi ned as the time interval where the charge signal lies between 10% and 90% of the maximum amplitude.

B.2 Signal reconstruction

This paragraph deals with an important problem I had to face during the analysis of high energetic dust impactors. In order to increase the dynamic range of the charge measurements, the instrument electronics is able to switch between a high charge amplification mode (for low impact charges) to a low charge amplification mode (in case of high impact charges.) The impact charge threshold value is about $2 \cdot 10^{-11}$C. Therefore, signals generated by high energetic impactors have to be reconstructed before calculating their rise time and their amplitude. To achieve this operation, the signal digitalized values during the switch process must be rejected. However, as the switch procedure does not have been tested in details during the instrument design phase, the signals were

sometimes difficult to reconstruct. Fig. B.3 shows the successful reconstruction of an electron impact charge signal. The original switched signal is shown in red, while the reconstructed signal is in black. The blue lines show the time difference between the 10% and the 90% of the signal amplitude (definition of the rise time).

C Calculating with quaternions

C.1 introduction

The analysis of scientific data obtained by an experiment carried on a spacecraft (camera, radar, magnetometers,...) requires generally a precise description of the spacecraft orientation in space. In particular, for in-situ dust and micrometeoroid research as performed with impact ionization detectors, a precise knowledge of the instrument's pointing is crucial. However, navigation constraints often force spacecrafts to achieve controlled rotations about their three main axis. As a consequence, the pointing of the mounted instruments with respect to an inertial frame is time dependent. Therefore, it is often needed to perform coordinate transformations between the reference frame and the frame attached to the spacecraft.

Each attitude modification of a spacecraft can be decomposed into a succession of translation and rotations. The most intuitive way to handle with rotations is to use the Euler angles description: any transformation of the spacecraft attitude can be obtained applying to the reference frame a combination of three rotations (sometimes called yaw, pitch, roll) about the main spacecraft axis. However, the description using the Euler angles have some disadvantages. First, the combination of basic rotations needed to achieve a transformation is not unique. Second, the Euler angles may lead to configurations where one degree of freedom is lost (so-called gimbal lock), leading to numerical (or mechanical) issues. Third, the equation of motion or the interpolation of the intermediate steps between two spacecraft attitude can not be solved in the practice using Euler angles. The quaternions give a mathematical answer to this problem.

C.2 The Quaternions: a generalisation of the complex numbers

In 1843, Hamilton found a 4-dimensional analog to the complex numbers and called them *quaternions*. I do not pretend providing here an exhaustive description of this mathematical theory. My aim is just to introduce some basic definitions needed for the comprehension of those mathematical objects. Then, I will discuss in details the efficiency of the quaternions description for handling with complex rotation in 3D. Practical examples will be given, as applications for the *Cassini*, *Galileo* and *Ulysses* spacecraft dynamics. A complement of theory may be found in Ebbinghaus (1992).

Quaternions are 4-tuples of real numbers, forming an algebra H, for which we can introduce a basis 1, i, j, k, satisfying:

$$i^2 = j^2 = k^2 = -1, ij = k, ji = -k, jk = i, kj = -i, ki = j, ik = -j, \tag{C.1}$$

Thus, each quaternion can be written as

$$Q = q_0 + xi + yj + zk, \tag{C.2}$$

where q_0 is the real part of the quaternion Q, and the vector $q = (x,y,z)$ its imaginary part, element of a 3-dimensional algebra with basis elements $\{i, j, k\}$. Let us rewrite the basis vectors $\{i, j, k\}$ as $\{e_i, e_j, e_k\}$. The multiplication of two basis vectors can be written concisely with the equation:

$$e_i e_j = -\delta_{ij} + \varepsilon_{ijk} e_k, \tag{C.3}$$

where,

$$\varepsilon_{ijk} = \begin{cases} 1: & (ijk) \text{ even permutation of } (123) \\ -1: & (ijk) \text{ odd permutation of } (123) \\ 0: & \text{else} \end{cases} \tag{C.4}$$

Let us consider $\vec{p} = \{p1, p2, p3\}$ and $\vec{q} = \{q1, q2, q3\}$ as imaginary part of the quaternions P and Q. It follows $P = p_0 + \vec{p}$ and $Q = q_0 + \vec{q}$. Using the multiplication rule (C.3), the product of two quaternions P, Q may be written as

$$PQ = (p_0 q_0 - \vec{p} \cdot \vec{q}, p_0 \vec{q} + q_0 \vec{p} + \vec{p} \wedge \vec{q}) \tag{C.5}$$

The conjugate of a quaternion is defined by analogy to the complex numbers by

$$\bar{Q} = q_0 - \vec{q} \tag{C.6}$$

and the norm by

$$|Q| = \sqrt{\bar{Q} Q} \tag{C.7}$$

For a quaternion $Q \neq 0$ the inverse quaternion is given by

$$Q^{-1} = \frac{\bar{Q}}{|Q|^2} \tag{C.8}$$

C.3 Using quaternion to represent rotations in 3D

A powerful application of the quaternions theory resides in the mathematical representation of rotations in R^3. Indeed, let us prove the existence of a bijection between S, subgroup of the quaternions with $|Q| = 1$, into the group R_θ of the rotations in R^3,

defined by the axis $\vec{n}$ and the angle $0 \leq \theta \leq 2\pi$. The vector $\vec{n}$ define the subspace W ($dimW = 1$) and its orthogonal subspace $W_\perp$. Given $\vec{v}$, a vector of R^3, we may uniquely decompose it as $\vec{v} = \vec{w} + \vec{z}$, where $\vec{w} \in W$ and $\vec{z} \in W_\perp$. Since $\vec{n}$ is an orthonormal basis vector for $W_\perp$, it follows that $\vec{z} = (\vec{n} \cdot \vec{v})\vec{n}$. Thus, $\vec{w} = \vec{v} - (\vec{n} \cdot \vec{v})\vec{n}$. Let us now apply the rotation R_θ to the vector $\vec{v}$. Since rotations are linear applications, we have,

$$\vec{v_\theta} = \vec{w_\theta} + (\vec{n} \cdot \vec{v})\vec{n} \tag{C.9}$$

An orthonormal basis of W is ($\frac{\vec{w}}{|\vec{w}|}$, $\frac{\vec{n} \wedge \vec{w}}{|\vec{n} \wedge \vec{w}|}$) . Therefore $\vec{w_\theta}$ can be decomposed as $\vec{w_\theta} = cos\theta \frac{\vec{w}}{|\vec{w}|} + sin\theta \frac{\vec{n} \wedge \vec{w}}{|\vec{n} \wedge \vec{w}|}$ Furthermore, the vector component on the W subspace will not be affected by the rotation (since W is the rotation axis), so that we get, using (C.9), the general formula:

$$\vec{v_\theta} = \cos\theta \vec{v} + (1 - \cos\theta)(\vec{n} \cdot \vec{v})\vec{n} + \sin\theta(\vec{n} \wedge \vec{v}) \tag{C.10}$$

Let us now consider S, the subgroup of H, made of the quaternions satisfying |Q|=1. If Q is an element of S, Q can be written as $Q = (\cos\frac{\theta}{2}, \vec{n}\sin\frac{\theta}{2})$, where $\vec{n}$ is a unit vector and $0 < \theta < 2\pi$. (Indeed, if $Q = (\alpha e, \beta\vec{n})$, with $\beta > 0$, $\alpha^2 + \beta^2 = 1$ implies the existence of a unique θ in $0 < \theta < 2\pi$ such as $\alpha = \cos\frac{\theta}{2}$ and $\beta = \sin\frac{\theta}{2}$)

We also define the endomorphism ξ of R^3 as the application: $\vec{v} \rightarrow Q\vec{v}\bar{Q}$. Using (C.5) for the quaternions multiplication rules, we find $\vec{v}\bar{Q} = (0, \vec{v})(\cos\frac{\theta}{2}, -\vec{n}\sin\frac{\theta}{2}) = (\vec{n} \cdot \vec{v}\sin\frac{\theta}{2}, \cos\frac{\theta}{2}\vec{v} - \vec{v} \wedge \vec{n}\cos\frac{\theta}{2})$. Further calculations give: $Q\vec{v}\bar{Q} = (0, \frac{1+\cos\theta}{2}\vec{v} + \frac{1-\cos\theta}{2}\vec{n} \cdot \vec{v}\vec{n} + \sin\theta\vec{n} \wedge \vec{v} + \frac{1-\cos\theta}{2}(\vec{n} \cdot \vec{v})\vec{n} - \vec{v})$. Hence, the resulting quaternion $\xi(\vec{v})$ is a vector, since its real part is equal to zero. Final calculations prove that:

$$\xi(\vec{v}) = \cos\theta\vec{v} + (1 - \cos\theta)(\vec{n} \cdot \vec{v})\vec{n} + \sin\theta(\vec{n} \wedge \vec{v}), \tag{C.11}$$

identical to the expression (C.10). Therefore, $\xi(\vec{v}) = \vec{v_\theta}$. As a consequence, a bijection between S and the rotations in R^3 exists. In other terms, each geometrical rotation may be represented by a quaternion Q of S and the associated linear application ξ. Note that the vector $\vec{n}$ and the sign of the angle θ specifies the orientation (clockwise or counter-clockwise) of the rotation in R^3.

The advantages of the quaternion representation are evident. First, it makes the calculation of multiple rotations easier than a conventional representation by Euler angles. Indeed, the three rotations required around three different axis may be replaced by a unique rotation and its associated quaternion $Q = Q_3Q_2Q_1$, where Q_3, Q_2, Q_1 are the quaternions associated to the successive rotations (Note the order for the multiplication, the quaternion multiplication is not commutative!). Second, we don't have to identify successive rotation axis to decompose the rotation, what always requires an outstanding capacity to 'see' in 3D. Indeed, the correct quaternion describing a rotation may be calculated just knowing the final and the initial vector position. At least, the quaternion associated to a given rotation is unique. Therefore, given two different spacecraft attitudes, there is a unique quaternion describing the rotation from the initial attitude

to the final one. Thus, there is no risk to decompose the spacecraft motion into a non optimized way or to lose one degree of freedom (no gimbal lock risk).

C.4 Application to the data analysis

During a nominal flight configuration phase, space probes need to are dynamically stabilized. Spacecrafts can be either three axis stabilized or spin-stabilized. *Cassini* is a three axis stabilized spacecraft: the spacecraft attitude is defined by the pointing of two of its main inertial axis. The sequences of the spacecraft attitude modifications are calculated by the flight software. In contrast, the *Galileo* and *Ulysses* spacecrafts are stabilized in rotation around their main antenna axis and achieve a few rotations per minute. For each spacecraft type, in addition to the dust impact data, the dust sensors provide the current attitude quaternion of the spacecraft. Hence, we are able to reconstruct the dust instrument pointing corresponding to the impact time.

An important problem throughout the data analysis performed in this thesis was the calculation of the sensitive area to a dust population. An impactor can hit the instrument target if the angle between the dust grain velocity vector relative to the spacecraft and the pointing of the dust detector is smaller than the aperture angle of the instrument. In order to calculate this angle, one need to transform the dust velocity vector from an inertial frame (ECLJ2000 for example, where the orbital elements of the grains are defined) into the instruments frame. This is done with the help of the associated quaternion. The reverse transformation is performed using the conjugate of this quaternion.

Assume a spacecraft coordinate frame to be defined. For example, in case of the *Cassini* spacecraft, the main antenna axis is the -Z axis, the magnetometer boom +Y. Thus, at a given time, two axis constraints fully determine the orientation of the spacecraft. Usually, the antenna is directed toward the Earth. An other direction, may be required for X or Y, for measurements or safety purposes. Fig. C.1 illustrates how to calculate the quaternion associated to the coordinate transformation from the heliocentric inertial frame system (ECLJ2000) to the spacecraft frame.

We define $\{\vec{\gamma}, \vec{Y_E}, \vec{N_E}\}$ to be the basis vectors of ECLJ2000. $\vec{\gamma}$ is the vernal equinox axis, $\vec{N_E}$the ecliptic north direction. Let us call $\{\vec{X_0}, \vec{Y_0}, \vec{Z_0}\}$ the spacecraft frame at a given time t_0.
The first step consists in calculating the quaternion $Q_0 = (\cos(\frac{\theta}{2}), \vec{n}\sin(\frac{\theta}{2}))$, associated to the right handed rotation that transforms $\vec{N_E}$into Z_0. The axis $\vec{n}$ is given by $\vec{n} = \frac{\vec{N_E} \wedge \vec{Z_0}}{|\vec{N_E} \wedge \vec{Z_0}|}$, and $\theta = \arccos(\vec{N_E} \cdot \vec{Z_0})$. If ξ_0 is the associated transformation, we have $\xi_0(\vec{N_E}) = Q_0 \vec{N_E} \bar{Q_0} = \vec{Z_0}$, but still, $\xi_0(\vec{\gamma}) \neq \vec{X_0}$ and $\xi_0(\vec{Y_E}) \neq \vec{Y_0}$. Therefore, we need a second quaternion by application of which, one of the secondary axis $\vec{X_0}$ or $\vec{Y_0}$ is obtained, without changing the primary axis $\vec{Z_0}$. Let us call the intermediate secondary axis $\xi_0(\vec{\gamma}) = \vec{X_{int}}$.

We consider the planes π_0 and π_{int} generated by, respectively, ($\vec{Z_0}$,$\vec{X_0}$) and ($\vec{Z_0}$,$\vec{X_{int}}$). The angle θ_π between the two planes π_0 and π_{int} is given by the angle between their normal unit vector, respectively, $\frac{\vec{Z_0}\wedge\vec{X_0}}{|\vec{Z_0}\wedge\vec{X_0}|}$ and $\frac{\vec{Z_0}\wedge\vec{X_{int}}}{|\vec{Z_0}\wedge\vec{X_{int}}|}$. Thus, $\theta_\pi = \arccos(\frac{\vec{Z_0}\wedge\vec{X_0}}{|\vec{Z_0}\wedge\vec{X_0}|}.\frac{\vec{Z_0}\wedge\vec{X_{int}}}{|\vec{Z_0}\wedge\vec{X_{int}}|})$. The quaternion $Q_1 = (\cos(\frac{\theta_\pi}{2}), \vec{Z_0}\sin(\frac{\theta_\pi}{2}))$ finally allows to reach the nominal configuration. As a whole, the quaternion of the transformation is given by $Q = Q_1 Q_0$.

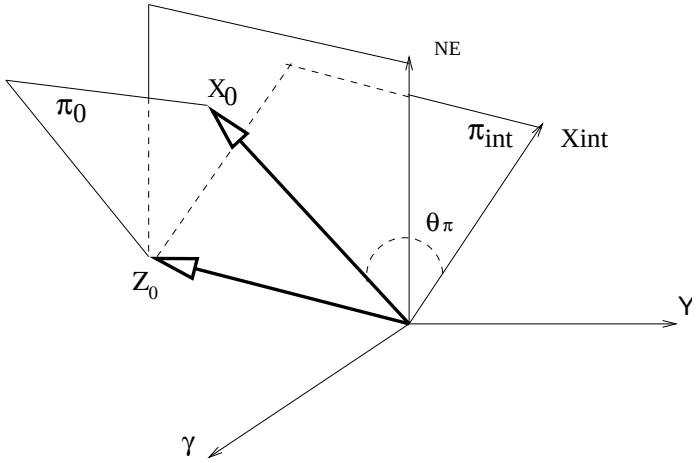

Figure C.1: This figure illustrates the determination of the quaternion associated to the transformation from the heliocentric frame $\{\vec{\gamma}, \vec{Y_E}, \vec{N_E}\}$ to the spacecraft frame $\{\vec{X_0}, \vec{Y_0}, \vec{Z_0}\}$ (see text).

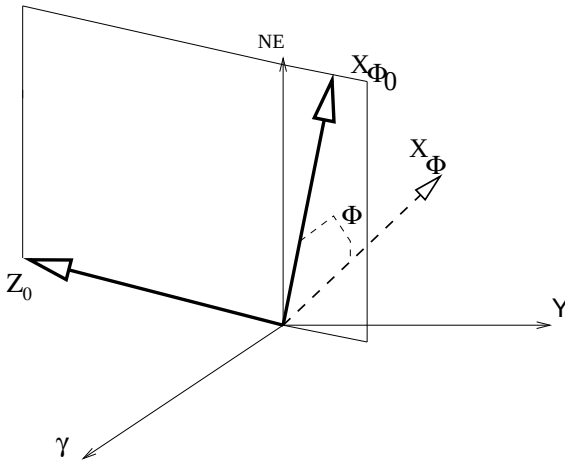

Figure C.2: For spinning spacecrafts like *Ulysses* and *Galileo*, the rotation is parameterized by the rotation angle ϕ. This figure illustrates the additional quaternion needed to describe this rotation, and the definition of the ϕ_0 = 0 direction (see text).

Similar calculations are performed for the *Galileo* and *Ulysses* spacecrafts. However,

those spacecrafts are spinning. Thus we have to define a zero value for the rotation angle which parameterizes the rotation. $\vec{Z_0}$ being the spin axis, an initial configuration of the spacecraft's frame $\{\vec{X_0}, \vec{Y_0}, \vec{Z_0}\}$ from which the successive configurations $\{\vec{X_\phi}, \vec{Y_\phi}, \vec{Z_0}\}$ are calculated (ϕ is the rotation angle, defined by the spin axis $\vec{Z_0}$ and the origin $\vec{X_{\phi_0}}$). The convention for *Ulysses* and *Galileo* is to take $\vec{X_{\phi_0}}$ so that the angle between the planes $\pi_{\vec{N_E}}$ and π_{ϕ_0} is equal to zero, $\pi_{\vec{N_E}}$ being the plane spanned by ($\vec{N_E}$, $\vec{Z_0}$) (see Fig. C.1). As a consequence, $\vec{N_E}$, $\vec{Z_0}$ and $\vec{X_{\phi_0}}$ are lying within the same plane. Finally, each configuration corresponding to $\phi \neq 0$ is simply obtained from the 'zero' configuration by achieving a rotation around $\vec{Z_0}$ by an angle ϕ, associated to the quaternion $Q_\phi = (\cos(\frac{\phi}{2}), \vec{Z_0}\sin(\frac{\phi}{2}))$.

Of course, in all cases, a last transformation is needed to transform coordinates from the spacecraft's frame into the dust instrument's frame. This can be achieved considering a 'hardware' quaternion, describing the mounting of the dust instruments to the spacecraft bus. In the *Galileo* and *Ulysses* cases, this quaternion is not time dependent since the dust instrument can not be oriented. On *Cassini*, however, the dust instrument is mounted on a turn table, so that the articulation angle of the turn table during the measurements has to be taken into account.

Bibliography

Alvarez, L. W., Alvarez, W., Asaro, F., and H. V. Michel 1980. Extraterrestrial Cause for the Cretaceous Tertiary Extinction. *Science* **208**, 1095–+.

Andreani, P., Franceschini, A., and G. Granato 1999. Dust emission from quasars and quasar host galaxies. *Mon.Not.R.Astron.Soc.* **306**, 161–180.

Auer, S. 2001. In situ Measurements of Cosmic Dust. In *Interplanetary Dust* pp. 385–444. Springer.

Baggaley, W. J. 2000. Advanced Meteor Orbit Radar observations of interstellar meteoroids. *J. Geophys. Res.* **105**, 10353–10362.

Baguhl, M., Grün, E., Hamilton, D. P., Linkert, G., Riemann, R., and P. Staubach 1995. The flux of interstellar dust observed by Ulysses and Galileo. *Space Sci. Rev.* **72**, 471–476.

Baguhl, M., Grün, E., and M. Landgraf 1996. In Situ Measurements of Interstellar Dust with the ULYSSES and Galileo Spaceprobes. *Space Science Reviews, v. 78, Issue 1/2, p. 165-172.* **78**, 165–172.

Baguhl, M., Grün, E., Linkert, G., Linkert, D., and N. Siddique 1993. Identification of 'small' dust impacts in the ULYSSES dust detector data. *Planetary and Space Sci.* **41**, 1085–1098.

Bleszynski, S. 1987. Filtering of the local interstellar medium at the heliopause. *Astron. Astrophys.* **180**, 201–206.

Brownlee, D. E. 1985. Cosmic dust - Collection and research. *Annual Review of Earth and Planetary Sciences* **13**, 147–173.

Ciolek, G. E. 1995. Ambipolar diffusion, interstellar dust, and the formation of protostellar cores. In *ASP Conf. Ser. 80: The Physics of the Interstellar Medium and Intergalactic Medium* pp. 174–+.

Czechowski, A. and I. Mann 2003. Penetration of interstellar dust grains into the heliosphere. *Journal of Geophysical Research (Space Physics)* pp. L13+.

Dietzel, H., Eichhorn, G., Fechtig, H., Grun, E., Hoffmann, H.-J., and J. Kissel 1973. The HEOS 2 and HELIOS micrometeoroid experiments. *Journal of Physics E Scientific Instruments* **6**, 209–17.

Dikarev, V., Jehn, R., and E. Grün 2002. Towards a new model of the interplanetary meteoroid environment. *Adv. Space Res.* **29**, 1171–1175.

Divine, N. 1993. Five populations of interplanetary meteoroids. *J. Geophys. Res.* **98**, 17029–17048.

Draine, B. T. 1990. Evolution of interstellar dust. In *The evolution of the interstel-*

lar medium, Proceedings of the Conference, Berkeley, CA, June 21-23, 1989. San Francisco, CA, Astronomical Soci ety of the Pacific, 1990 pp. 193–205.

Draine, B. T. and H. M. Lee 1984. Optical properties of interstellar graphite and silicate grains. *Astrophys. J.* **285**, 89–108.

Ebbinghaus, H. D., Hermes, H., Hirzebruch, F., Koecher, M., Mainzer, K., Neukirch, J., Prestel, A., and R. Remmert 1992. Hamiltonsche quaternionen. In *Zahlen* (S. Verlag Ed.) pp. 155–182.

Evans, A. 1994. *The dusty universe*. Chichester ; New York : J. Wiley ; Chichester : In association with Praxis Pub., Ltd., 1994.

Fahr, H. J. 1968. On the Influence of Neutral Interstellar Matter on the Upper Atmosphere. *Astrophys. Space Sci.* **2**, 474–+.

Fahr, H. J. 1991. Local interstellar oxygen in the heliosphere - Its analytic representation and observational consequences. *Astron. Astrophys.* **241**, 251–259.

Fechtig, H. 1989. Dust in the solar system. *Z. Naturforsch* **44a**, 877–882.

Flynn, G. 1991. In *Accretion of meteoric material onto Mars-Implications for the surface, atmosphere, and moons* pp. 121–124. Pergamon, New York.

Friichtenicht, J. F. and J. C. Slattery 1963. Ionization associated with hypervelocity impacts. *Nasa Technical Note* D-2091.

Frisch, P. C., Dorschner, J. M., Geiss, J., Greenberg, J. M., Grün, E., Landgraf, M., Hoppe, P., Jones, A. P., Krätschmer, W., Linde, T. J., Morfill, G. E., Reach, W., Slavin, J. D., Svestka, J., Witt, A. N., and G. P. Zank 1999. Dust in the Local Interstellar Wind. *Astrophys. J.* **525**, 492–516.

Giese, R.-H. 1973. Mikrowellen-Analogieversuche und Lichtstreuung an kosmischem Staub. *Mitteilungen der Astronomischen Gesellschaft Hamburg* **32**, 162–+.

Göller, J. R. and E. Grün 1989. Calibration of the Galileo/Ulysses dust detectors with different projectile materials and at varying impact angles. *Planet. Space Sci.* **37**, 1197–1206.

Greenberg, J. M. 1988. The interstellar dust model of comets - post halley. In *Dust in the Universe* pp. 121–143.

Greenberg, J. M. 1997. Prebiotic chiral molecules created in interstellar dust and preserved in comets, comet dust, and meteorites: an exogenous source of life's origins. In *Proc. SPIE Vol. 3111, p. 226-237, Instruments, Methods, and Missions for the Investigation of Extraterrestrial Microorganisms, Richard B. Hoover; Ed.* pp. 226–237.

Greenberg, J. M., Gillette, J. S., Muñoz Caro, G. M., Mahajan, T. B., Zare, R. N., Li, A., Schutte, W. A., de Groot, M., and C. Mendoza-Gómez 2000. Ultraviolet Photoprocessing of Interstellar Dust Mantles as a Source of Polycyclic Aromatic Hydrocarbons and Other Conjugated Molecules. *Astrophys. Journal* **531**, L71–L73.

Greenberg, J. M. and J. I. Hage 1990. From interstellar dust to comets - A unification of observational constraints. *Astrophys. J.* **361**, 260–274.

Grün, E. 1981. In *Physikalische und chemische Eigenschaften des interplanetaren Staubesmessungen des Mikrometeoritenexperimentes auf Helios*. Bundesministerium für Forschung und Technologie, Forschungsbericht W 81-034.

Grün, E. 2000. Dust in the Solar System. In *The Outer Heliosphere: Beyond the*

Planets pp. 289–304, Copernicus Gesellschaft e.V.

Grün, E., Baguhl, M., Divine, N., Fechtig, H., Hamilton, D. P., Hanner, M. S., Kissel, J., Lindblad, B.-A., Linkert, D., Linkert, G., Mann, I., McDonnell, J. A. M., Morfill, G. E., Polanskey, C., Riemann, R., Schwehm, G., Siddique, N., Staubach, P., and H. A. Zook 1995a. Three years of Galileo dust data. *Planetary and Space Sci.* **43**, 953–969.

Grün, E., Baguhl, M., Divine, N., Fechtig, H., Hamilton, D. P., Hanner, M. S., Kissel, J., Lindblad, B.-A., Linkert, D., Linkert, G., Mann, I., McDonnell, J. A. M., Morfill, G. E., Polanskey, C., Riemann, R., Schwehm, G., Siddique, N., Staubach, P., and H. A. Zook 1995b. Two years of Ulysses dust data. *Planetary and Space Sci.* **43**, 971–999.

Grün, E., Baguhl, M., Fechtig, H., Hanner, M. S., Kissel, J., Lindblad, B.-A., Linkert, D., Linkert, G., Mann, I., and J. A. M. McDonnell 1992. Galileo and ULYSSES dust measurements - From Venus to Jupiter. *Geophys.Res.Lett.* **19**, 1311–1314.

Grün, E., Baguhl, M., Hamilton, D. P., Kissel, J., Linkert, D., Linkert, G., and R. Riemann 1995c. Reduction of Galileo and Ulysses dust data. *Planetary and Space Sci.* **43**, 941–951.

Grün, E., Fechtig, H., Giese, R. H., Kissel, J., Linkert, D., Maas, D., McDonnel, J., Morfill, G., Schwehm, G., and H. Zook 1992a. The Ulysses dust experiment. *A&A Supl. Ser.* **92**, 411–423.

Grün, E., Fechtig, H., Hanner, M., Kissel, J., Lindblad, B.-A., Linkert, D., Maas, D., Morfill, G., and H. Zook 1992b. The Galileo dust detector. *Space Sci. Rev.* **60**, 317–340.

Grün, E., Gustafson, B., Mann, I., Baguhl, M., Morfill, G. E., Staubach, P., Taylor, A., and H. A. Zook 1994. Interstellar dust in the heliosphere. *Astron. Astrophys.* **286**, 915–924.

Grün, E., Kempf, S., Srama, R., Moragas-Klostermeyer, G., and N. Altobelli 2002. Analysis of impact ionization from 300 km/s fast projectiles. In *Geophysical Research Abstracts*, Vol. 4, EGS.

Grün, E., Krüeger, H., Srama, R., Kem pf, S., Auer, S., Colangeli, L., Horanyi, M., Withnell , P., Landgraf, M., Landgraf, P., and H. Svedhem 2000. Techniques for Galactic Dust measurements in the Heliosphere. *J. Geophys. Res.* **105**, 10403–10410.

Grün, E., Krüger, H., Graps, A.L.and Hamilton, D., Heck, A., Linkert, G., Dermott, S., Fechtig, H., Gustafson, B., Hanner, M., Hor'anyi, M., Kissel, J., Lindblad, B., Linkert, D., Mann, I., McDonnel, J., Morfill, G., Polanskey, C., Schwehm, G., and R. Srama 1998. Galileo observes electromagnetically coupled dust in the Jovian magnetosphere. *J. Geophys. Res.* **103**, 20 011–20 022.

Grün, E. and M. Landgraf 1997. Collisional Consequences of Big Interstellar Grains. In *Bulletin of the American Astronomical Society* p. 1045, Vol. 29.

Grün, E. and M. Landgraf 2000. Collisional consequences of big interstellar grains. *J. Geophys. Res.* **105**, 10291–10298.

Grün, E., Pailer, N., Fechtig, H., and J. Kissel 1980. Orbital and physical characteristics of micrometeoroids in the inner solar system as observed by HELIOS 1. *Planet.*

Space Sci. **28**, 333–349.

Grün, E., Srama, R., Rachev, M., Srowig, A., Harris, D., Conlon, T., and S. Auer 2003. An Advanced Dust Telescope. *AGU Fall Meeting Abstracts* pp. B401+.

Grün, E., Staubach, P., Baguhl, M., Hamilton, D. P., Zook, H. A., Dermott, S., Gustafson, B. A., Fechtig, H., Kissel, J., Linkert, D., Linkert, G., Srama, R., Hanner, M. S., Polanskey, C., Horanyi, M., Lindblad, B. A., Mann, I., McDonnell, J. A. M., Morfill, G. E., and G. Schwehm 1997. South-North and Radial Traverses through the Interplanetary Dust Cloud. *Icarus* **129**, 270–288.

Grün, E., Zook, H., Baguhl, M., Balogh, A., Bame, S., Fechtig, H., Forsyth, R., Hanner, M., Horanyi, M., Kissel, J., Lindblad, B.-A., Linkert, D., Linkert, G., Mann, I., McDonnel, J., Morfill, G., Phillips, J., Polanskey, C., Schwehm, G., Siddique, N., Staubach, P., Svestka, J., and A. Taylor 1993. Discovery of Jovian dust streams and interstellar grains by the Ulysses spacecraft. *Nature* **362**, 428–430.

Grün, E. and H. A. Zook 1980. Dynamics of micrometeoroids. In *IAU Symp. 90: Solid Particles in the Solar System* pp. 293–298.

Grün, E., Zook, H. A., Fechtig, H., and R. H. Giese 1985. Collisional balance of the meteoritic complex. *Icarus* **62**, 244–272.

Gustafson, B. 1994. Physics of Zodiacal Dust. *Ann. Rev. Earth Planet. Sci.* **22**, 553–595.

Gustafson, B. S. and N. Misconi 1979. Streaming of Interstellar Grains in the Solar System. *Nature* **282**, 276–278.

Hall, J. S. 1949. Observations of the Polarized Light from Stars. *Science* **109**, 166–167.

Hamilton, D., Grün, E., and M. Baguhl 1996. Synthesis of Observations. In *Electromagnetic escape of dust from the Solar System* pp. 31–34. B.A.S.Gustafson and M.S. Hanner.

Hiltner, W. A. 1949. On the Presence of Polarization in the Continuous Radiation of Stars. II.. *Astrophys. J.* **109**, 471–+.

Hoffmann, H.-J., Fechtig, H., Grün, E., and J. Kissel 1975. First results of the micrometeoroid experiment S 215 on the HEOS 2 satellite. *Planetary and Space Science* **23**, 215–224.

Holzer, T. E. 1989. Interaction between the solar wind and the interstellar medium. *Astron. Astrophys.* **27**, 199–234.

Horányi, M. 1996. Charged dust dynamics in the solar system. *Annu. Rev. Astrophys.* **34**, 383–418.

Hornung, K. and S. Drapatz 1980. Residual ionization after impact of large dust particles. In *ESA SP-155*.

Jenkins, E. B. 1987. Element abundances in the interstellar atomic material. In *ASSL Vol. 134: Interstellar Processes* pp. 533–559.

Jones, A. P., Tielens, A. G. G. M., and D. J. Hollenbach 1996. Grain Shattering in Shocks: The Interstellar Grain Size Distribution. *Astrophys. J.* **469**, 740–+.

Kimura, H., Mann, I., and A. Wehry 1999. Interstellar Dust in the Solar System. *Astr. Space Sci.* **264**, 213–218.

Kissel, J. and F. Krueger 1987. Ion Formation by Impact of Fast Dust Particles and Comparison with related Techniques. *Appl. Phys.* **A 42**, 69–85.

Krivov, A. V., Wardinski, I., Spahn, F., Krüger, H., and E. Grün 2002. Dust on the Outskirts of the Jovian System. *Icarus* **157**, 436–455.

Krüger, H., Grun, E., Heck, A., and S. Lammers 1999. Analysis of the sensor characteristics of the Galileo dust detector with collimated Jovian dust stream particles. *Planet. Space Sci.* **47**, 1015–1028.

Kyte, F. T. 1988. Accretion Rate of Extraterrestrial Matter: Iridium Deposited over the Last 70 Million Years. *LPI Contributions* **673**, 101–+.

Landgraf, M. 1998. *Modellierung der Dynamik und Interpretation der In-Situ Messung interstellaren Staubs in der Lokalen Umgebung des Sonnensystems. Ph.D. thesis*, Universität Heidelberg.

Landgraf, M., Augustsson, K., Grün, E., and B. A. S. Gustafson 1999. Deflection of the Local Interstellar Dust Flow by Solar Radiation Pressure. *Science* **286**, 2319–2322.

Landgraf, M., Baggaley, W. J., Grün, E., Krüger, H., and G. Linkert 2000. Aspects of the mass distribution of interstellar dust grains in the solar system from in situ measurements. *J. Geophys. Res.* **105**, 10343–10352.

Landgraf, M., Krüger, H., Altobelli, N., and E. Grün 2003. Penetration of the heliosphere by the interstellar dust stream during solar maximum. *J. Geophys. Res.* **108**, 5–1.

Levy, E. H. and J. R. Jokipii 1976. Penetration of interstellar dust into the Solar System. *Nature* **264**, 423–424.

Li, A. and J. M. Greenberg 1997. A unified model of interstellar dust.. *Astron. Astrophys.* **323**, 566–584.

Linde, T. J. and T. I. Gombosi 2000. Interstellar dust filtration at the heliospheric interface. *J. Geophys. Res.* **105**, 10411–10418.

Mann, I. 1995. The Out of Ecliptic Distribution of Interplanetary Dust and Its Relation to Other Bodies in the Solar System. *Earth Moon and Planets* **68**, 419–426.

Marvin, U. B. 1987. The planetary and interstellar components of meteorites - a review. In *IAU Symp. 120: Astrochemistry* pp. 469–483.

Mathis, J. S., Rumpl, W., and K. H. Nordsieck 1977. The Size Distribution of Interstellar Grains. *Astrophys. J.* **217**, 425–433.

McNeil, W., Lai, S., and E. Murad 1996. A model for meteoric magnesium in the ionosphere. *J. Geophys. Res.* **101**, 5251.

Morfill, G. and E. Grün 1979. The Motion of Dust Particles in Interplanetary Space-Interstellar Grains. *Planetary and Space Science* **105**, 1283–1292.

Mulser, P. 1971. Electrostatic fields and ion separation in expanding laser produced plasmas. *Plasma Physics* **13**, 1007–1012.

Parker, E. N. 1958. Dynamics of the Interplanetary Gas and Magnetic Fields. *Astrophys. J.* **128**, 664–+.

Raizer, Y. 1960. Residual ionization of a gaz expanding in vacuum. *Sov.Phys.* **JETP 10**, 411.

Sears, F. H. 1940. The dust of space. *Astronomical Society of the Pacific. J.* **52**, 80.

Srama, R. 2000a. *CDA Calibration Report*. Technical report, MPI-K.

Srama, R. 2000b. *Vom Cosmic-Dust-Analyzer zur Modellbeschreibung wissenschaftlicher Raumsonden. Ph.D. thesis*, Technische Universität München.

Staubach, P., Grün, E., and R. Jehn 1997. The meteoroid environment near earth. *Adv. Space Res.* **19**, 301–308.

Staubach, P., Grün, E., and M. J. Matney 2001. Synthesis of Observations. In *Interplanetary Dust* pp. 347–384. Springer.

Stübig, M. 2002. *New insights in impact ionization and in time-of-flight mass spectroscopy with micrometeoroid detectors by improved impact simulations in the laboratory*. *Ph.D. thesis*, MPI-K.

Svedhem, H., Munzenmayer, R., and H. Iglseder 1996. Detection of possible interstellar particles by the hiten spacecraft. In *ASP Conf. Ser. 104: IAU Colloq. 150: Physics, Chemistry, and Dynamics of Interplanetary Dust* pp. 27–+.

Wilck, M. and I. Mann 1996. Radiation pressure forces on "typical" interplanetary dust grains. *Planetary and Space Science* **44**, 493–499.

Witte, M., Rosenbauer, H., Banaszkiewicz, M., and H. Fahr 1993. The ULYSSES neutral gas experiment - Determination of the velocity and temperature of the interstellar neutral helium. *Advances in Space Research* **13**, 121–130.

Yabushita, S. and A. Allen 1989. On the effect of accreted interstellar matter on the terrestrial environment. *Mon.Not.R.astr.Soc* **238**, 1465–1478.

Yeghikyan, A. and H. Fahr 2003. Effects induced by the passage of the Sun through dense molecular clouds. *Astron. Astrophys.* pp. 127–135.

Danksagung

Ich möchte allen danken, die zum Gelingen dieser Arbeit beigetragen haben. In erster Linie gilt ein besonderer Dank an Herrn Prof. Dr. Eberhard Grün für seine Geduld und seine immer wertvolle Anregungen bei der Jagd nach interstellaren Staubteilchen. Ich konnte mich auch immer auf die volle Unterstützung der Staubgruppe Mitglieder verlassen. Insbesondere, die Hilfbereitschaft und die exzellente Betreuung von Sascha Kempf, Harald Krüger und Ralf Srama hat die Alltagsarbeit in ein echtes Vergnügen verwandelt! Darum bedanke ich mich bei Markus Landgraf, durch den ich diese Gruppe kennengelernt habe. Valeri Dikarev sei hier auch gedankt für seine konstruktive Kritik und die Zeit, die er immer fand, um mir zuzuhören. Danke auch an Stefan Helfert für seine Computer-Tipps und an Georg Moragas-Klostermeyer. Zu der guten Stimmung und dem Arbeitspass haben auch meine anderen Kollegen viel beigetragen. Es seien hier meine Mitdoktoranden erwähnt, Jessica Argarwal, Anna Mocker, Mikhail Rachev und Andre Srowig. Den anderen aktuellen Staubleuten gilt auch mein Dank: Gerhard Schäfer, Angelika Baron, Gudrun Linkert, Wolfgang Müller, Richard Moissl, Frank Müller, Frank Potsberg und Sacher Khoudari. Dem Max-Planck-Institut für Kernphysik möchte ich für die finanzielle Unterstützung danken.

Enfin, merci à toi, Virginie, pour ton soutien et l’ énergie que tu m’ as communiquée durant ces années!

Declaration

This thesis was processed with LaTeX.
I assure that I wrote this thesis independently and that I did not use other than the given resources.

Erklärung

Diese Arbeit wurde mit LaTeX geschrieben. Ich versichere, dass ich diese Arbeit selbständig verfasst und keine anderen als die angegebenen Hilfsmittel benutzt habe.

Heidelberg, den 16. März 2004